A THEORETICAL ANALYSIS OF

GaInNAs/GaAs QUANTUM WELLS FOR
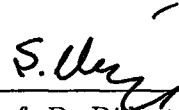
LONG WAVELENGTH EMISSION

Ph. D Thesis

in

Engineering Physics

University of Gaziantep
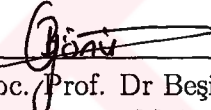
By

Murat ODUNCUOĞLU

July 2004

Approval of the Graduate School of Natural and Applied Sciences.

_____
Prof. Dr Bülent GÖNÜL
Director

I certify that this thesis satisfies all the requirements as a thesis for the degree of Doctor of Philosophy.
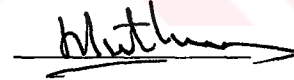
_____
Assoc. Prof. Dr Zihni ÖZTÜRK
Head of Department

This is to certify that we have read this thesis and that in our opinion it is fully adequate, in scope and quality, as a thesis for the degree of Doctor of Philosophy.
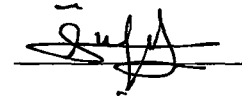
_____
Assoc. Prof. Dr Beşire GÖNÜL
Major Supervisor

Examining Committee Members:
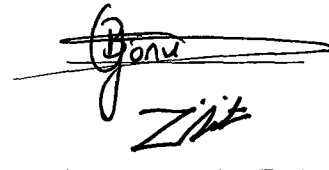
Prof. Dr İbrahim Halil MUTLU

Prof. Dr Ömer Faruk BAKKALOĞLU

Prof. Dr Sadettin ÖZYAZICI

Assoc. Prof. Dr Beşire GÖNÜL

Assoc. Prof. Dr Zihni ÖZTÜRK

Abstract

A THEORETICAL ANALYSIS OF GaInNAs/GaAs QUANTUM WELLS FOR LONG WAVELENGTH EMISSION

ODUNCUOĞLU, Murat

Ph. D in Engineering Physics

Supervisor: Assoc. Prof. Dr Beşire GÖNÜL

July 2004, 136 pages

III-N-V alloys of $Ga_{1-x}In_xN_yAs_{1-y}$ display unusual physical properties compared to that of the conventional III-V semiconductors. While conventional semiconductors have a tendency of increasing bandgap energy with decreasing lattice constant, III-N-V exhibit quite different behaviour, an increase of N concentration causes a monotonic decrease of the bandgap, instead of an increase, towards that of cubic GaN.

The work carried out in this thesis reveals that doping and pressure can cause the III-N-V systems having additional unusual properties compared to that of the III-V systems.

The theoretical calculations have shown that the effective mass of the electron increases with nitrogen concentration. This behaviour is opposite to the conventional semiconductors. We have seen that the addition of nitrogen into InGaAs leads the GaInNAs system having a band alignment of that of the ideal case (deep conduction wells and shallow valence wells). Therefore, the use of GaInNAs as an active layer causes better carrier confinement and hence reduces the carrier leakage at high temperatures.

We have presented model calculations to analyze the pressure dependence of band structure, effective mass, optical confinement factor, peak gain and the differential gain. These calculations have shown that although transparency carrier density increases with pressure, the threshold carrier density, can decrease due to the increased optical confinement factor. The loss mechanism in a semiconductor laser are strongly wavelength dependent and pressure can vary the bandgap. Therefore, we have used the pressure dependence of the above laser parameters to investigate the loss mechanism for a typical three competing laser

devices emitting in the neighborhood of 1.3 μm. The variation of pressure dependence of laser parameters indicates that aluminium and nitride based laser systems are superior to that of the phosphide based laser system and offers the Al- and N-based laser systems as ideal candidates for low threshold and high speed applications, respectively. We have found that the estimated variation of phonon-assisted Auger rates with pressure in N-based system has a slower decrease than that of the other two laser systems. The threshold carrier density n_{th} in N-based system increases with pressure whereas it decreases in Al- and P-based laser systems. This opposite variation change the overall behaviour of the threshold current in these three competing laser systems. Our theoretical calculations indicate a significant increase of the radiative to non-radiative recombination current in N-based laser system. This result highlights the intrinsic superiority of the N-based laser system.

We have presented calculations which shows that doping has a reverse effect on gain characteristic of GaInNAs/GaAs laser system than that of the N-free corresponding laser system. So we have concluded, for the first time, that this is another unusual physical property of nitrogen containing alloys due to the nitrogen-induced modified conduction band. We have also shown that the gain characteristics of GaInNAs/GaAs laser system can be significantly improved by means of doping following the route of the high indium and low nitrogen concentration. We have seen that the optimal route of 1.3 μm wavelength GaInNAs would be the choice of the higher indium instead of the higher nitrogen due to the better matching of the effective masses, favorable band alignment, smaller transparency carrier density, higher peak and differential gain and lower spontaneous emission factor.

An accurate material gain calculation is a necessary ingredient for a full characterization of III-V and III-N-V laser systems. Material gain calculations, generally ignores the Coulomb interaction between electrons and holes. We have determined that the neglect of the Coulombic attraction between electrons and holes is an overestimation, since the linear gain is enhanced at least three orders of the magnitude when these interactions are taken into account.

The optimization of III-N-V quantum well active layer for improved device performance requires a clear understanding of exciton behavior in quantum wells. An enhancement of the ground state heavy hole exciton have been calculated in $Ga_{1-x}In_xN_yAs_{1-y}$ / GaAs compared to that of the $In_xGa_{1-x}As$/GaAs. Moreover, we have seen that the binding energy of the exciton increases with increasing nitrogen concentration. The close examination of the In/N ratio dependence of the band offsets and reduced exciton mass revealed the fact that low In / high N route must be chosen to get higher exciton binding energies in 1.3 μm laser systems. We have also compared the P-based laser seems as an ideal laser system due to the enhanced exciton binding energies. N-based lasers have intermediate binding energy values and Al- based lasers seem the worst one.

Key words: GaInNAs/GaAs, nitrides, band anti-crossing model, pressure, bandgap renormalization, band offsets, exciton binding energy, gain, doping.

Öz

GaInNAs/GaAs UZUN DALGABOYLU KUANTUM KUYU LAZERLERİN TEORİK OLARAK İNCELENMESİ

ODUNCUOĞLU, Murat

Doktora Tezi, Fizik Mühendisliği Bölümü

Tez Yöneticisi: Doç. Dr Beşire GÖNÜL

Temmuz 2004, 136 sayfa

Yaygın olarak kullanılan III-V yarıiletkenler ile III-N-V alaşımı olan GaIn-NAs karşılaştırıldığında farklı fiziksel özellikler sergilediği görülmüştür. III-V yarıiletkenlerinin band aralığı örgü sabitinin azalması ile artarken, III-N-V sistemlerde azalmaktadır. Bu alaşımda azot konsantrasyonun artması kübik yapıdaki GaInN'ın tersine band aralığını azaltmaktadır.

Bu tezde yapılan çalışmalar katkı atomlarının ve basıncın III-N-V sistemlerinde, III-V sistemlerine nazaran sıradışı özelliklere sahip olduğunu gösterir.

Yapılan teorik hesaplamalarda etkin kütlenin azot konsantrasyonunun artması ile arttığı görülmüştür. Bu özellik yaygın olarak kullanılan yarıiletkenlerin tam tersidir. InGaAs yarıiletkenine azot ekleyerek GaInNAs elde edildiğinde, lazerler için ideal yapı olan derin iletkenlik bandı ve sığ değerlilik bandı elde edilebilmektedir. Bundan dolayı GaInNAs aktif tabaka olarak kullanıldığında yük taşıyıcılar daha iyi hapsedilebilmekte ve bunun sonucu olarak da yüksek sıcaklıklarda yük taşıyıcı sızmaları azalmaktadır.

Basınca bağlı olarak değişen band yapısı, etkin kütle, optik hapsolma faktörü ve kazanç grafikleri model hesaplamalarla analiz edildi.

GaInNAs üretmek için azot eklenen InGaAs materyal üzerindeki değişiklikler anlatıldı. İletkenlik bandı ve azot ekleme sonucu olusan enerji seviyesi arasındaki etkileşimlerin band yapısı ve artan etkin kütle üzerindeki etkileri analitik olarak incelendi.

Hesaplamalarda saydamlık taşıyıcı yoğunluğunun arttığı ve optik hapsolma faktörünün artmasından dolayı eşik taşıyıcı oranlarında azalma görüldü. Yarıiletken lazerlerde kayıp mekanizması dalgaboyuna bağlıdır ve basınç band aralığını değiştirir. Basıncın etkisi ile değişen lazer parametreleri hesaplanarak 1.3 μm'de ışıma yapan birbirine benzer üç lazer sistemi için kayıp mekanizmaları incelendi. Al

ve N lazer sistemlerinin basınçla değişen materyal parametreleri P lazer sisteminden daha iyi sonuçlar verdiği görüldü. Böylece Al lazerlerin düşük eşik için ve N lazer sistemleri ise yüksek hız uygulamaları için iyi birer aday olduğu belirlendi. Hesaplamalarımız N'li sistemlerin fonon-yardımcılı Auger oranlarının diğer iki sisteme göre yavaş düşüş yaptığını göstermiştir. Eşik taşıyıcı yoğunluğu, N lazer sistemlerinde basınçla artarken Al ve P lazer sistemlerinde azalmaktadır. Sistemlerin bu şekilde farklı değişiklik göstermesi eşik akım değerlerinin bütün özelliklerini değiştirmektedir. Teorik hesaplamalarımızda N lazerlerinde yayılımlı ve yayılımsız değerlilik bandından iletkenlik bandına geçiş akımlarında artış olduğunu göstermiş ve bu N lazerlerinin olumlu yanlarını açıklamamıza yardım etmiştir.

Yaptığımız hesaplamalarda GaInNAs yapılarında katkılamanın kazanç karakteristikleri üzerinde azotsuz sistemlerden farklı özellikler gösterdiği görüldü. İlk olarak biz, azot katkılı alaşımların bu farklı özelliğinin iletkenlik bandındaki değişimden kaynaklandığını gösterdik. Ayrıca, $Ga_{1-x}In_xN_yAs_{1-y}$ lazer sisteminin kazanç karakteristiklerinin yüksek In / düşük N yoğunluğu kullanılarak katkılama yöntemi ile iyileştiğini gözledik. 1.3 μm dalgaboylu $Ga_{1-x}In_xN_yAs_{1-y}$ sistemlerinde yüksek In konsantrasyonu tercih edildiğinde etkin kütlede, band yapısında, geçirgenlik taşıyıcı yoğunluğunda, kazançta ve düşük eş zamanlı dağılım faktöründe istenilen değerlere ulaştığı görüldü.

Kazanç hesaplamaları III-V ve III-N-V sistemlerinin tam olarak karakterize edilebilmesi için önemli bir faktördür. Materyal kazanç hesaplamaları yapılırken genellikle elektron ve boşlukların Coulomb etkileşmesi gözönüne alınmaz. Bu etkileşimi kazanç hesaplamalarımıza eklediğimizde kazançta yaklaşık üç kat artış olduğunu tespit ettik.

III-N-V lazer sistemlerinin optimizasyonunda eksitonların davranışlarınında anlaşılması gerekmektedir. $Ga_{1-x}In_xN_yAs_{1-y}$/GaAs ve $In_xGa_{1-x}As$/GaAs için eksiton hesaplamaları yapıldı ve bu iki sistem karsılaştırıldı. Azot yoğunluğunun artması, eksitonun bağlanma enerjisini arttırmaktadır. Değerlilik ve iletim bandı derinliği ve indirgenmiş eksiton kütlesinin, In/N oranına bağımlılığını ortaya çıkaran hesaplamalar, 1.3 μm lazerlerindeki eksiton bağlanma enerjisinin düşük In / yüksek N oranına sahip olduğunda en yüksek değere ulaştığını göstermiştir. Ayrıca P, Al ve N lazer sistemleri için eksiton bağlanma enerjilerinin, kuyu genişliğine bağlı olarak değişimi hesaplandı. P lazer sisteminin eksiton bağlanma enejisi en yüksek, Al lazer sisteminin en düşük ve N- lazer sisteminin ise bu iki sisteme ait değerlerin arasında olduğu gözlendi.

Anahtar kelimeler: GaInNAs/GaAs, azot, band anticrossing modeli, basınç, bant aralığı daralması, bant genişliği, eksiton bağlanma enerjisi, katkılama

I dedicate this work to my family

Acknowledgements

I wish to express my sincere gratitude and thank to my supervisor, Assoc. Prof. Dr Beşire GÖNÜL, for guiding, advising and encouraging me throughout, ensuring that the project was successful and enjoyable.

I wish to thank everyone in the Engineering Physics Department for many useful discussions and for the sharing of their friendship. In particular, I would like to thank to Assist. Prof. Dr Andrew BEDDALL for LATEX, and to my dear friend Dr Okan ÖZER for his emotional support throughout the thesis.

My special thanks go to my mother and father, who were a prop to me during this work by their faithful prays.

To my wife and son, I owe my sincere thanks for her unshakable faith in me and her willingness to endure with me.

Table of Contents

List of Tables

Table

List of Figures

Figure

List of Symbols

e : Electron charge

$\hbar$: Plank's Constant

k_B : Boltzmann's constant

T : Temperature

a_e : Lattice constant of epitaxial layer

a_s : Lattice constant of substrate

ε : Strain

E_g : Energy gap (in units of eV)

Δ_o : Spin-orbit splitting (eV)

C_{11} : Elastic stiffness (GPa)

C_{12} : Elastic stiffness (GPa)

b : Deformation potential (eV)

d : Deformation potential (eV)

m_c : Electron effective mass

m_{hh} : Valence band (heavy hole) effective mass

m_{lh} : Valence band (light hole) effective mass

m_s : Spin-split-off band

m_r : Reduced mass

γ_1 : Luttinger Parameters

γ_2 : Luttinger Parameters

E_M : Conduction states of the matrix semiconductor

E_N : Localized nitrogen state energy (eV)

V_{MN} : Matrix element of interacting localized and extended states

$E_{\pm}$: Conduction band energy states

$Q_{c,v}$: Band offset ratio for conduction- and valence-band

$\Delta E_{c,v}$: Band discontinuities for conduction- and valence-band

E_c : Conduction band energy (eV)

E_v : Valence band energy (eV)

Γ : Optical confinement factor

Φ : Electric field amplitudes

μ : Dipole moment along a given polarisation of light

ϵ_0 : Permittivity in vacuum

n_r : Refractive index of the material

n : Carrier density

L_z : Well width

$f_{c,v}$: Fermi occupation factors for electrons at the conduction and valence subband edges

G_{max} : Band edge peak gain

β : Differential gain

n_{tr} : Transparency carrier density

n_{th} : Threshold carrier density

g_{th} : Threshold material gain

$\alpha_{a,c}$: Active and cladding layer losses

L : Length of the laser

R_m : Reflectivity of the end mirrors

V : Pumped volume of the active region

A : Monomolecular recombination coefficient

B : Bimolecular radiative recombination coefficient

C : Auger coefficient

$\langle M_{av}^2 \rangle$: Squared momentum matrix element

k : Wavevector

E_a : Activation energy

J_{th} : Threshold current density

$|M_{ee}|$: Electron-electron interaction matrix element

$f_{CH,SH}$: Oscillator strengths

E_p : Energy equivalent of the momentum matrix element

S : Spontaneous noise

n_{sp} : Amplifier noise enhancement factor or spontaneous emission factor

$N_{A,D}$: Acceptor and donor carrier concentrations

V_{sq} : Screened Coulomb potential

ω_{pl} : Plasma frequency

ω_q : Effective plasmon mode frequency

ϵ_b : Background dielectric constant

a_0 : Bohr radius

ϵ_R : Exciton Rydberg energy

κ : Inverse screening length

ΔE_{CH} : Coulomb-hole self energy

ΔE_{SX} : Screened-exchange shift

$\alpha(\omega)$: Linear gain

τ_{in} : Intraband relaxation time

ω : Angular frequency of light

E_{cv} : Transition energy

Chapter 1

Introduction

The growth of the internet and data transmission are pushing the bandwidth requirements for fibre networks. For optical fiber telecommunication lasers emitting in the wavelength range from 1.25 to 1.65 μm are the subject of intense investigations. Devices with emission wavelengths between 1.3 and 1.6 μm are of primary importance in optical local (LAN) and metro (MAN) area networks, and long haul communications due to the dispersion zero at 1.3 μm and minimum loss at 1.55 μm in optical silica fiber.

Up to now lasers at these wavelengths are almost exclusively fabricated from GaInAsP or AlGaInAs heterostructures on InP. While InGaAsP/InP-based lasers have been the sources for long-haul, 1.55 μm optical-fibre backbone networks for the past three decades, their cost is simply far too high to meet the demands of tens of million lasers that might be utilized in each MAN and LAN in a modern datacom network architecture. For many years it was believed that there was no suitable alloy lattice matched to GaAs, so InGaAsP on InP was the only material system that met the perceived criteria. All the long-wavelength communication lasers (100 %) presently in use are fabricated from this system. There has been intense effort to realize low cost, long wavelength systems over the past decade, however, the physical properties of the previously utilized semiconductor systems made this nearly impossible. An alternative solution to InP epitaxy would be to use materials grown on GaAs. However, alloys which are

nearly lattice-matched to GaAs, historically have optical emission at wavelengths less than 1.1 μm. The well-known materials limitations of the InGaAsP system pushed Kondow et al [1] to examine GaInNAs as an alternative active-region material that could be grown on GaAs. Lasers made from new material systems, such as dilute nitrides and antimonides, or quantum dot active regions, are promising approaches to achieving temperature-insensitive 1.3 μm lasers on GaAs substrates.

A second major challenge for semiconductor lasers is a higher temperature insensitivity of the laser threshold and output, which could allow for uncooled operation of the devices. The fundamental heterojunction bandgap offsets between InP and InGaAsP, limiting electron confinement in the quantum wells achieving adequate power output with these lasers has always been a challenge. This results in a much lower T_0 compared to the InGaAs/GaAs materials. Kondow et al [1] were also the first to point out that the higher conduction band offset in GaInNAs compared to InGaAsP would lead to higher T_0 for this material. In addition, significant non-radiative Auger recombination occurs in InGaAsP at high injection densities, creating greater problems for high-power lasers. Both of these combine to increase threshold and heating at higher power levels. While InP-based materials have dominated this technology in the past, their ability to produce adequate power and manufacturing shortcomings compared to GaAs-based systems provide an opening for GaInNAs/GaAs-based, long-wavelength, high-power lasers. In order to greatly expand broadband amplifier used in MANs, the key elements that must be achieved are sufficient power and low cost.

Kondow et al [1] proposed and grew the material system, a number of research groups have since demonstrated diode laser operation using GaInNAs quantum well lasers. This material has attracted attention by virtue of its unusual physical properties than that of the conventional $III - V$ compounds. GaInNAs is a candidate for long wavelength emission with contrary to the general rules of $III - V$ alloy semiconductors where a smaller lattice constant increases

the bandgap, the large electronegativity of N and its small covalent radius cause a very strong negative bowing parameter and the addition of N to GaAs or In-GaAs dramatically decreases the bandgap [1]. By combining N and In, GaInNAs produces a very rapid decrease in bandgap to reach the long-wavelength emission region with simultaneous control over bandgap and lattice match to GaAs. Such an active quantum-well material allows the fabrication of 1.3 μm lasers.

1.1   Thesis Outline

The research work reported in this thesis is concerned with the design and characterisation of 1.3 μm GaAs-based structures.

Chapter 2 presents a brief qualitative introduction to nitride based laser systems, covering the basic concepts required in the remainder of the thesis. The electronic properties of the alloy GaInNAs is markedly different from most other III-V alloys. The decrease in energy per atomic percent of nitrogen is more than ten times greater than the typical increase in other semiconductor alloys [2]. In addition, electron effective mass increases as the energy gap decreases [3], contrary to other alloy systems. This result appears to invalidate any simple interpolation scheme and favor the authors to use band-anti-crossing model of the interaction between localised N states and the extended states of the semiconductor matrix which is briefly reviewed in this chapter. As an overview, model calculations are presented in this chapter as well.

Hydrostatic pressure is an extremely useful tool to vary continuously the band structure of the semiconductor and hence to investigate the important loss mechanism of Auger recombination in the semiconductor lasers. The band structure parameters of bandgap and effective mass are strongly dependent on pressure. In Chapter 3, the changes in band structure and optical confinement factor with pressure for different nitrogen concentrations are determined and their effect on transparency- and threshold-carrier density analysed.

Chapter 4 introduces a theoretical comparison of pressure dependence of

threshold current of 1.3 μm lasers. The results regarding the nitride-, phosphide-, and aluminium-based 1.3 μm lasers are explained. By means of determining the pressure dependence of the required material parameters for these three systems a comparison of the threshold carrier, radiative and non-radiative current density is provided. Model calculations have been presented to choose the ideal laser material system with low threshold characteristics from the three typical competing laser devices emitting in the neighborhood of 1.3 μm.

In Chapter 5, we study the theoretical potential advantage of doped 1.3 μm emission $Ga_{1-x}In_xN_yAs_{1-y}$/GaAs quantum wells. We investigate how the doping concentration modifies the fermi functions, band structure, gain characteristics and spontaneous emission factor by modelling five different $Ga_{1-x}In_xN_yAs_{1-y}$ / GaAs quantum well laser structures in terms of simplified models for different x/y ratios. A systematic study of the band-offset ratio for different In/N ratios has been undertaken. Model solid theory has been used to calculate the band offset ratios including the effect of strain and modifications in conduction band. We determine the optimal laser configuration of compressively strained $Ga_{1-x}In_xN_yAs_{1-y}$ quantum well lasers emitting at 1.3 μm. An equivalent nitrogen-free system is also provided for comparison. This study provides useful information for the optimization of doped $Ga_{1-x}In_xN_yAs_{1-y}$/GaAs on the basis of 1.3 μm emission wavelength.

The focus of Chapter 6 is to first provide the theoretical background of bandgap renormalization and then present the comparison of material gain calculations with and without bandgap renormalization. Bandgap renormalization is a many body effect and it is due to the free carriers. The attractive Coulomb electron-hole attraction enhances the optical gain, therefore for a careful analysis of gain characteristics it should be taken into account.

The binding energy of the ground state exciton in III-V and III-N-V single quantum well is investigated in Chapter 7. The exciton binding energy is calculated by using simple two-band model, including strain and the difference in

dielectric constants between well and barrier materials. In first part of Chapter 7, the fully analytical method to calculate the exciton binding energy is briefly introduced. In the second part of the chapter, we firstly investigate the nitrogen dependence of exciton binding energy in $Ga_{1-x}In_xN_yAs_{1-y}$/GaAs laser material system. Secondly, we determine the optimal route of In/N by means of comparing the binding energies for 1.3 μm $Ga_{1-x}In_xN_yAs_{1-y}$/GaAs laser systems. Finally, a comparative study of exciton binding energies as a function of well width is undertaken for the three competing laser material systems of P-, AL- and N-based lasers.

Chapter 8 gather together the major conclusions from the work described in this thesis. Future work is also provided in this chapter.

Chapter 2

The Theoretical Models

2.1 Introduction

This chapter provides the models and the corresponding calculations relevant to the study of GaInNAs/GaAs quantum well laser systems used in this thesis. There have been numerous attempts to explain the properties of the $III - N - V$ materials. The $III - N - V$ alloy GaInNAs shows quite remarkable band structure properties that raise exciting possibilities for optoelectronic applications. Although GaN has a much larger bandgap than GaAs, when a low concentration of N is incorporated into InGaAs there is a very strong decrease in the optical bandgap. This is very interesting both theoretically and practically: theoretically, because the behavior cannot be explained by standard models of III-V alloys and so new approaches are clearly needed; practically, because the lower bandgap makes accessible in the GaAs system the 1.3 μm and 1.55 μm wavelengths of interest for optical fibre communications. If we can achieve a good theoretical understanding of the band structure and optical properties of GaInNAs, the possibility exists that we may be able to propose novel and superior optoelectronic device structures, (eg with $m_c^* = m_v^*$). A special effort has been focused on understanding the large bandgap reductions [4, 5]. The effects of the nitrogen incorporation into InGaAs is described in section 2.2. The quaternary material parameters for analog of the nitrogen-containing systems

discussed in section 2.3. The band structure of GaInNAs system is explained by using band anti-crossing model (BAC) [6], which is discussed in section 2.4. The band alignment in GaInNAs quantum structure is outlined in section 2.5.

2.2 Effects of nitrogen in GaInNAs

GaInNAs exhibits interesting new properties and differs considerably from the conventional III-V alloys, such as AlGaAs, GaInAs and GaInAsP, which are commonly employed in III-V device structures. GaInNAs is composed of hexagonal GaInN and cubic InGaAs. Significant changes occur in the band structure compared to GaAs with incorporation of only a small percentage of nitrogen. These include a large red shift of the bandgap [7, 8], an increase in the electron effective mass [6, 9, 10], a highly nonlinear pressure dependence of the bandgap [11, 12], a N-induced formation of new bands [8, 12, 13, 14], and a strong linewidth broadening of all transitions [8, 13, 14, 15]. The key to understand these unusual properties of the GaInNAs alloys is the large difference in size and electronegativity of arsenic and nitrogen atoms. The covalent radius and electronegativity of nitrogen are 0.068 $\mathring{A}$ and 3.04, respectively, compared to those of 0.121 $\mathring{A}$ and 2.18 for arsenic. A large difference in the atomic size causes deformation of the crystal lattice and the larger electronegativity of nitrogen favors electron localization around the nitrogen atom. In 1984 nitrogen was found to act as an isoelectronic impurity in GaAs, and the localized energy state formed by a single nitrogen atom was observed at 150-180 meV above the bottom of the conduction band [16]. In 1990 Liu et al. [17] reported excitonic luminescence originating from nitrogen pair and cluster states located below the conduction band minimum of GaAs. The N concentration in their study was about $10^{17} cm^{-3}$, i.e., 0.001%. More recently it has been found that the nitrogen incorporation leads to the strong red shift of the bandgap when the N concentration is increased to above 0.01% [18]. However, the luminescence spectrum of GaAsN is still dominated by sharp excitonic transitions.

GaInNAs exhibits a remarkable band-gap bowing, enabling optical emission at 1.3 and 1.5 μm on a GaAs substrate. In calculation of fundamental bandgap, the huge bandgap bowing parameters have been discovered. In alloying GaAs with nitrogen leads to a giant bandgap bowing with increasing molar fraction. Bandgap reductions of as large as 180 meV have been obtained in $GaAs_{1-x}N_x$ with only 1% of nitrogen [7] - [19]. Similar effects have been observed in InAsN [20], GaPN [21, 22], InPN [23], GaAsSbN [24], and InSbN [25] alloys.

Fig. 2.1 shows the lattice constants and bandgaps of some III-V semiconductors. The lattice constant of GaAsN behaves linearly and decreases with concentration, since the lattice constant of cubic GaN is 4.5 $\mathring{A}$. If linear approximation would apply, an increase of the bandgap energy from 1.42 eV of GaAs toward 3.2 eV of cubic GaN could be expected. Instead, the bandgap shows huge bowing with increasing N concentration. The N-induced decrease of the lattice constant can compensated and the bandgap further reduced by adding indium to GaAsN. Therefore, it is possible to grow $Ga_{1-y}In_xN_yAs_{1-x}$ quaternary alloy that has a bandgap suitable for long-wavelength optical communications.
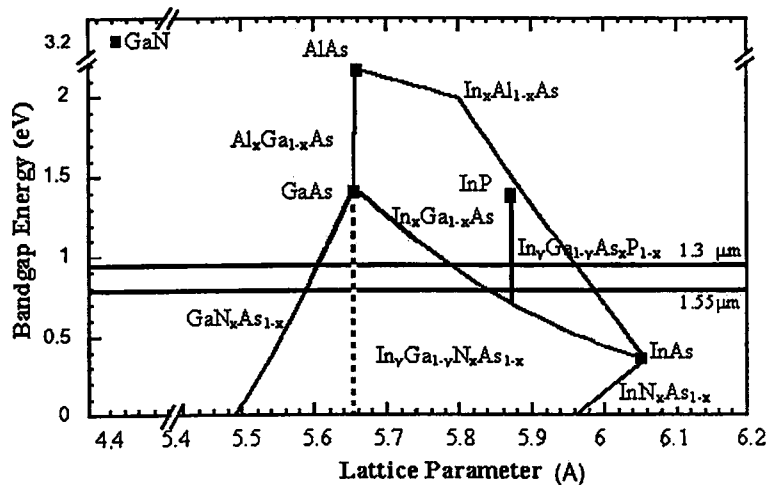
Figure 2.1: Bandgaps and lattice constants of some binary III-V semiconductors (squares). The fiber-optical communication wavelengths of 1.3 and 1.55 μm are also shown. GaInNAs can reach these wavelengths lattice matched to GaAs.

2.3   Theoretical models

In this section we present the models and the related material parameter calculations that we have used throughout this thesis.

2.3.1   Material parameters

The material parameters such as lattice constants, Luttinger parameters and strain-related parameters of the conventional ternary and quaternary systems can be calculated by linear interpolation method [29]. The material parameters depend on the well and barrier compositions, their widths and growth orientation. The parameters for the quaternary alloy $Ga_{1-x}In_xN_yAs_{1-y}$ are interpolated from the binary compound values, such as B_{GaN}, B_{GaAs}, B_{InN}, and B_{InAs} using the following expression of

$$Q_{GaInNAs}(x,y) = x\,y\,B_{InN} + x\,(1-y)\,B_{InAs}$$
$$+ (1-x)\,y\,B_{GaN} + (1-x)\,(1-y)\,B_{GaAs} \quad (2.1)$$

where x is the fractional composition of indium, In, and y is the fractional composition of nitrogen, N, in GaInNAs. The nitrogen-related binary material values used in this thesis are given in Table 2.1.

Material	GaAs	InAs	GaN	InN
Lattice Constant a_o (Å)	5.6533	6.0584	4.50	4.98
Energy gap E_g (eV)	1.42	0.417	3.299	1.94
Spin-orbit Splitting Δ_o (eV)	0.34.	0.39	0.017	0.006
Elastic Stiffness C_{11} (GPa)	1221	932.9	293	187
Elastic Stiffness C_{12} (GPa)	566	45.6	159	125
Deformation Potential b (eV)	-2.0	-1.8	-2.2	-1.2
Deformation Potential d (eV)	-4.8	-3.6	-3.4	-9.3
Electron Effective Mass m_c (m_o)	0.067	0.026	0.15	0.12
Effective mass m_{hh} (m_o)	0.35	0.333	0.855	0.833
Luttinger Parameters γ_1	6.98	20.0	2.67	3.72
Luttinger Parameters γ_2	2.06	8.5	0.75	1.26

Table 2.1: Binary material parameters [29, 30].

The addition of indium in to GaNAs to produce GaInNAs causes a reduction in the bandgap and an increase in lattice parameters. But the increase in nitrogen fraction causes a reduction in the bandgap and decreases the lattice parameter. The change in bandgap and lattice parameter gives the flexibility of tailoring both bandgap and lattice parameter. Hence, GaInNAs gives the potential to grow lattice matched or strained materials on GaAs substrate. Moreover, the effect of strain on the band structure varies with growth orientation. The lattice constant for any given composition of binary, ternary, or quaternary well material compared with that of the substrate material determines whether the structure under investigation is an unstrained or strained laser device. The change in lattice parameter and strain for GaInNAs system are calculated by using interpolation method and shown in Fig. 2.2 and 2.3, respectively.
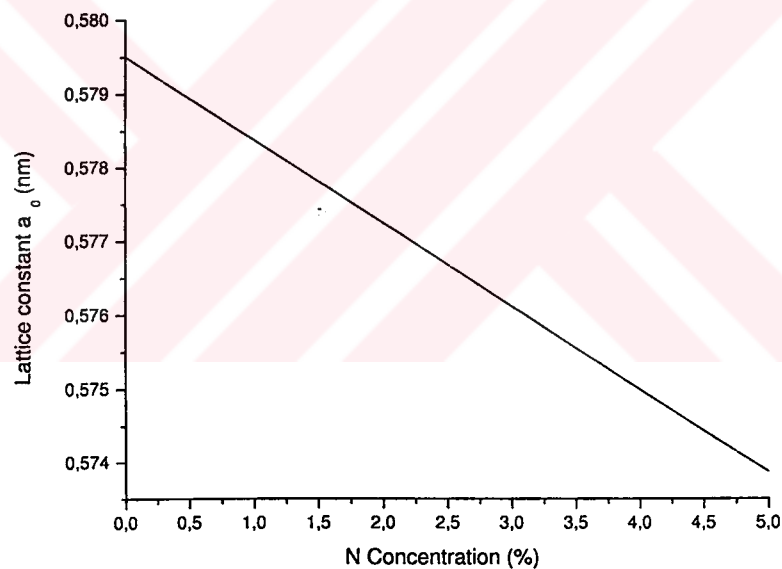
Figure 2.2: The variation of lattice constant with nitrogen concentration in GaIn-NAs.
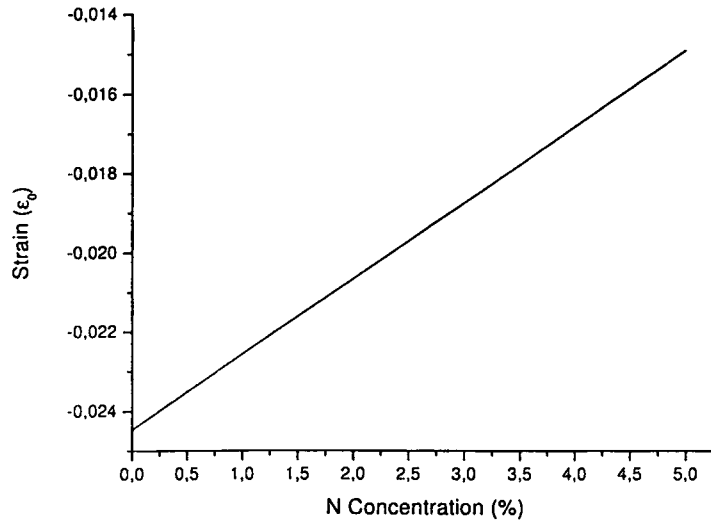
Figure 2.3: The calculated variation of strain versus nitrogen concentration in GaInNAs.

2.4   The band anti-crossing model

The bandgap energy has been successfully described for bulk semiconductor in terms of anti-crossing between the conduction band minimum of InGaAs and resonant band of localized nitrogen defect states above the band edge [31, 32]. The two-level band anti-crossing model (BAC) describes the electronic structure of $Ga_{1-x}In_xN_yAs_{1-y}$. In literature, some groups has been used this model and the results were found to be in good agreement [6, 12, 26, 27].

According to band anticrossing model, the incorporation of N into InGaAs (or GaAs) alloys leads to a strong interaction between the conduction band and a narrow resonant band formed by the N states. The overall effect is the splitting of the conduction band, with a consequent reduction of the fundamental bandgap due to the lowering of the conduction band edge. The mathematical formalism of the model is derived as follows [12]. The interaction between the extended conduction states of the matrix semiconductor (InGaAs) and the localized N states is treated as a perturbation which leads to the following eigenvalue problem

of

$$\begin{vmatrix} E - E_M & -V_{MN} \\ -V_{MN} & E - E_N \end{vmatrix} = 0 \qquad (2.2)$$

where E_M is the conduction states of the matrix semiconductor, E_N is the localized nitrogen state energy (relative to the top of the valence band) and V_{MN} is the matrix element describing the interaction between these two states. Incorporation of the interaction represented by the matrix element V_{MN} leads to a mixing and anti-crossing of these states. The solution to this eigenvalue problem gives us the dispersion relation for $Ga_{1-x}In_xN_yAs_{1-y}$

$$E_{\pm}(k) = \frac{[(E_M(k) + E_N) \pm \sqrt{(E_M(k) - E_N)^2 + 4C_{MN}^2}]}{2} \qquad (2.3)$$

The BAC model provides simple analytic expressions for the conduction band dispersion as a function of N concentration y and allows to calculate, for example, the strength of the optical transitions [33] in bulk materials and the transition energies between electronic states in quantum wells or the gain in laser structures [34].

A schematic diagram of the band structure for $Ga_{1-x}In_xN_yAs_{1-y}$ according to Eqn. (2.3), and the $E_{\pm}(k)$ and E_N levels, is shown in Fig. 2.4. All energies are measured relative to top of the valence band in this figure. The E_+ transition is blue shifted and the E_- transition is red shifted from the N resonant level with increasing N concentration. According to this model, the E_- subband has mainly delocalized conduction band-like character, whereas the E_+ subband is due to the localized E_N-like states. An increase in the V_{MN} value with increasing N concentration leads to a stronger repulsion between the E_- and E_+ states.

One of the most striking features of the results is a distinct flattening of the $E_{\pm}$ curves for energies approaching E_N. This indicates a large increase in of the effective mass in both subbands compared to GaAs. A strong non-parabolicity of the conduction band can also be predicted from Fig. 2.5. The electron effective mass is another important material parameters and depend very strongly on the electron energy relative to localized E_N level.
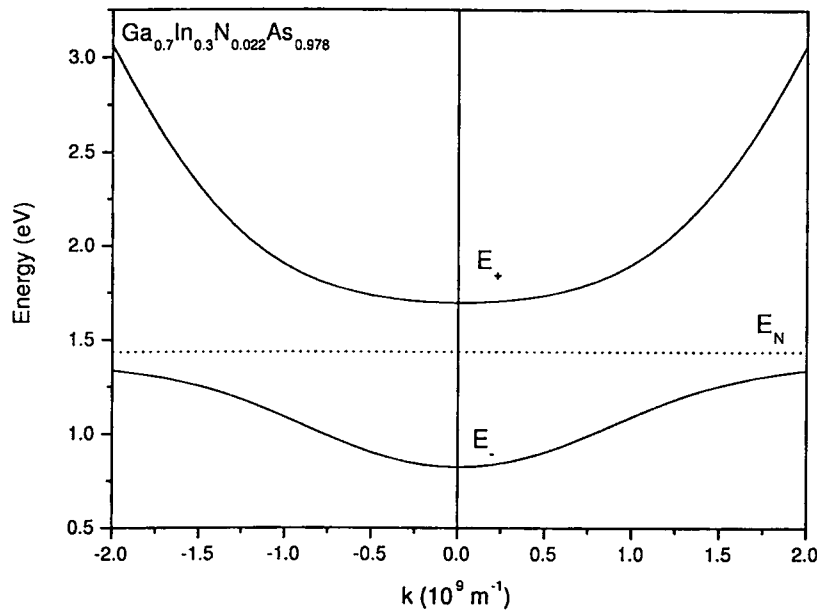
Figure 2.4: The calculated conduction band structure of $Ga_{0.7}In_{0.3}N_{0.022}As_{0.978}$ near the Γ-point ($k = 0$) according to the BAC model. A parabolic approximation for the conduction band of InGaAs was used. The splitting of the conduction band into E_- and E_+ bands is clearly shown. The energy scale is relative to the top of the valence band.

2.4.1   Verification of the Band Anti-crossing Model

In the literature it seems, so far, that the BAC model is well established as far as the macroscopic behavior is concerned. Shan et al [12, 27] measured optical transitions under pressure, where optical transitions are observed, which are associated with the two branches of the split lowest conduction band in GaInNAs for various compositions.

Skierbiszewski et al [35] examined the carrier dynamics in a GaNAs alloy where they measured the mobility of carriers in the alloy and compared it to the theoretical mobility, calculated, from the BAC model; the qualitative and quantitative agreement of theory and experiment was good. These authors also examined the increase of the conduction band effective mass theoretically (in the context of the BAC model) and experimentally; again the agreement was very good [6].

Uesugi et al [36] have indirectly confirmed the central idea of the model (i.e. the interaction of the extended and localized levels) through the temperature dependence of bandgap energies of GaNAs films for various N concentrations. The result showed that, in determining the temperature dependence of the bandgap energy, two kinds of N-related energy states with different temperature dependence of bandgap energy must be considered: one with a higher temperature dependence similar to the GaAs bands (extended like state) and an N-related localized state with lower temperature dependence.

Finally, Lindsay and O'Reilly [37] have adopted a theoretical approach. By using a tight-binding sp^3s^* Hamiltonian, they have calculated the compositional dependence of the conduction band edge and then compared it with the E_- energy calculated according to the BAC model. These results were found to be in good agreement, as well.

2.4.2   Parameters within the band anticrosssing model

In order for the dispersion relation predicted by the model to reproduce the band structure of the real semiconductor as accurately as possible, the interaction matrix element V_{MN} and the nitrogen level E_M must be determined along with their dependence on composition. In addition, an accurate form for the electron effective mass is required for the calculation of various laser parameters. The E_M is the energy of the InGaAs matrix conduction band and is given as [5],

$$E_M(k) = \begin{cases} E_0 - 1.55y + \frac{\hbar^2 k^2}{2m}, & \text{eV inside the well;} \\ E_0, & \text{outside the well.} \end{cases} \tag{2.4}$$

where y denotes the nitrogen concentration and $\frac{\hbar^2 k^2}{2m}$ is quadratic conduction band dispersion term, E_0 is the conduction band edge of the well/barrier material in the absence of nitrogen. The energy of the nitrogen level is taken as

$$E_N = \begin{cases} 1.52 - \gamma y, & \text{eV inside the well;} \\ 1.52 + E_{b,N}, & \text{outside the well.} \end{cases} \tag{2.5}$$

where $\gamma = 2.52$ for GaNAs and $\gamma = 3.9$ for GaInNAs. The height of the nitrogen barrier, $E_{b,N}$ and E_N are assumed independent of k and all the energies are taken relative to the top of the valance band. The strength of the $\Gamma - E_N$ interaction is described by the interband matrix element V_{MN}. The square of the matrix element V_{MN}^2 is proportional to concentration of nitrogen atom as

$$V_{MN} = \begin{cases} C_{MN}\sqrt{y}, & \text{inside the well;} \\ 0, & \text{elsewhere.} \end{cases} \tag{2.6}$$

The V_{MN} is a key parameter describing the interaction between the localized and extended states. The values of V_{MN} is not constant and may be composition dependent [12, 35]. In this thesis we have used the value of V_{MN} as $2.7\sqrt{y}$ eV [32].

Using these parameters we calculate these subband energies of E_- and E_+ versus nitrogen concentration as shown in Fig. 2.5. With increasing nitrogen concentration E_- energy shifts towards lower energies. On the contrary, the E_+ energy shifts towards higher energies with increasing nitrogen. The E_+ level has been found to increase linearly with a slope nearly equal to the decrease in E_-.

2.4.3   Electron Effective Mass

A knowledge of the carrier mass is necessary for analysis of important semiconductor properties. As is well known, the carrier mobility is strongly dependent upon the effective mass. In addition, the knowledge of the effect of the effective mass on gain parameters is of special importance for a full exploration and optimization of $III - N - V$ material system in device applications. Therefore, the change in electron effective mass due to the nitrogen modified conduction band is investigated in this section.

Unlike other conventional alloy semiconductors, the electron effective mass increases when the energy bandgap is reduced by adding nitrogen. This has a profound influence on the strength of electron-photon and electron-electron
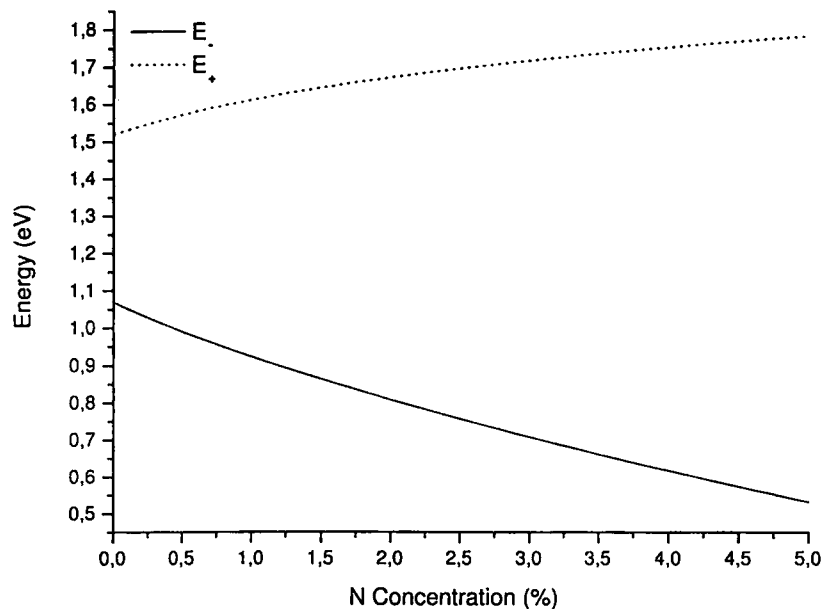
Figure 2.5: Calculated subband energies E_- and E_+ as a function nitrogen concentration for $Ga_{0.7}In_{0.3}N_yAs_{1-y}$, according to BAC model.

interactions, and consequently on every aspect of the performance (threshold current, etc.) of semiconductor lasers. As can be seen from Fig. 2.4, the energy E_- is flattening near its minimum leading to a large enhancement of the electron effective mass. The change in electron effective mass due to the nitrogen modified conduction band can be found by Skierbiszewski et al [35] as

$$m^* = m_M \left[1 + \left(\frac{V_{MN}}{(E_N - E_-)} \right)^2 \right] \tag{2.7}$$

where m_M is the electron effective mass in the parabolic conduction of the semiconductor matrix.

The electron effective mass of electron increases with nitrogen composition, as shown in Fig. 2.6. This behavior is rather unusual and in fact is opposite to the conventional semiconductors, where the value of effective mass decreases with decrease of bandgap energy.
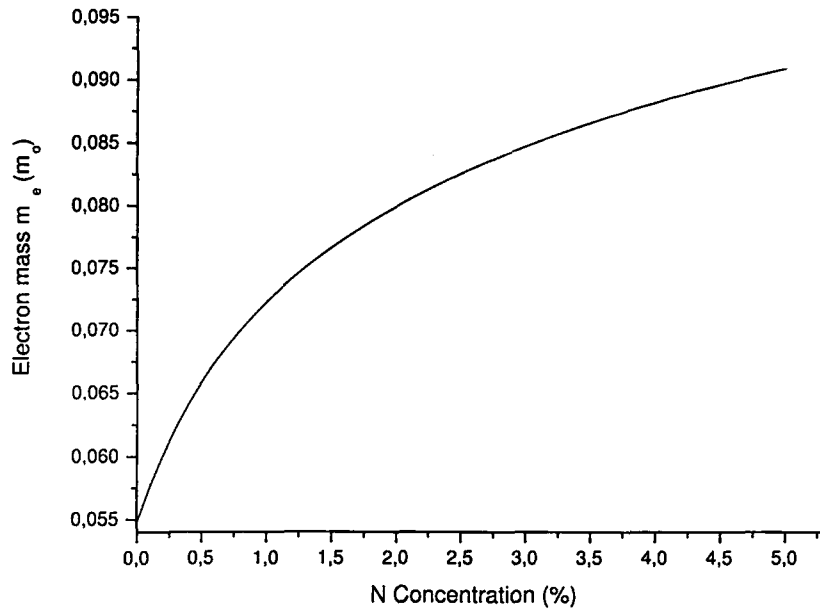
Figure 2.6: The calculated values of electron effective mass with increasing nitrogen concentration.

2.5   Band Offset Ratios

The band offset is an important parameter for the design of heterostructure based electronic and optoelectronic devices. The relative band alignment of band edges between the quantum well and the barrier is the total band discontinuity, distributed over the conduction and valence bands, as ΔE_c and ΔE_v respectively. The band discontinuity depends on the semiconductors and the amount of mismatch strain at the interface. It has been commonly accepted that nitrogen incorporation mainly affects the conduction band states of the GaInNAs alloys leading to an increase in the conduction band offset, Q_c, and only a small discontinuity in the valence band edge [3].

In this section, two models regarding the band alignment, "Model Solid Theory" and "Harrison's Model", which are used to calculate band offsets of III-V and III-N-V semiconductor laser material systems are reviewed.

2.5.1 Model solid theory

The band offset ratio, $Q_{c,v}$, is determined by discontinuity fractions of $\frac{\Delta E_{c,v}}{\Delta E_g}$. The energy of the potential barrier, ΔE_g is determined from the difference between the bulk bandgap energy of the barrier layers and the strained bandgap energy of the active layer. The bulk bandgap energy of GaInNAs is calculated by means of band anti-crossing model which defined previous section. The necessary material parameters of the well and barrier materials are calculated by using interpolation method.

The effects of strain in the plane of the epitaxial growth is calculated as

$$\varepsilon = \frac{a_s - a_e}{a_e} \tag{2.8}$$

where a_e is the lattice constant of quaternary epitaxial layer and a_s is the lattice constant of substrate. The conduction band position can be calculated by simply adding the strained bandgap energy to the valence band position. The unstrained valence band-edge of the active region material is set as the reference energy of zero. The valence band position is given by

$$E_v(x,y) = \begin{cases} E_{v,av}(x,y) + \frac{\Delta_0(x,y)}{3} + \delta E_{hh}(x,y), & \text{for hh (compressive strain);} \\ E_{v,av}(x,y) + \frac{\Delta_0(x,y)}{3} + \delta E_{lh}(x,y), & \text{for lh (tensile strain).} \end{cases} \tag{2.9}$$

where $E_{v,av}(x,y)$ is the average valence subband energy and Δ_0 is the spin-orbit split-off band energy. These values are obtained by linear interpolation method (binary values are listed in Table 2.1 and Table 2.2). The conduction band is shifted by the energy $\delta E_c(x,y)$ and given as

$$\delta E_c(x,y) = 2a_c\left(1 - \frac{C_{12}}{C_{11}}\right)\varepsilon \tag{2.10}$$

the valence bands are shifted by energy, $\delta E_{hh}(x,y)$ and $\delta E_{lh}(x,y)$ are expressed as

$$\delta E_{hh}(x,y) = -P_\epsilon - Q_\epsilon \tag{2.11}$$

$$\delta E_{lh}(x,y) = -P_\epsilon + Q_\epsilon \tag{2.12}$$

Materials	Symbol(Unit)	GaAs	InAs
Model Solid Theory			
Average valence band position	$E_{v,av}$	-6.92	-6.67
Harrison's Model			
Conduction band position	$E_c^H(eV)$	1.53	0.801
Valence band position	E_v^H	0.111	0.441

Table 2.2: Parameters for the calculation of the band alignments using Model Solid Theory [38] and Harrison's model [39].

where

$$P_\epsilon = -2a_v\left(1 - \frac{C_{12}}{C_{11}}\right)\varepsilon \qquad (2.13)$$

$$Q_\epsilon = -b\left(1 + 2\frac{C_{12}}{C_{11}}\right)\varepsilon \qquad (2.14)$$

where a_c and a_v are the conduction- and valence-band hydrostatic deformation potentials, and b is the valence band shear deformation potential. The strained bandgaps can then be expressed as

$$E_{c-hh}(x,y) = E_g(x,y) + \delta E_c(x,y) + \delta E_{hh}(x,y) \qquad (2.15)$$

$$E_{c-lh}(x,y) = E_g(x,y) + \delta E_c(x,y) + \delta E_{lh}(x,y) \qquad (2.16)$$

The conduction band position is

$$E_c(x,y) = \begin{cases} E_v(x,y) + E_{c-hh}, & \text{for hh (compressive strain);} \\ E_v(x,y) + E_{c-lh}, & \text{for lh (tensile strain).} \end{cases} \qquad (2.17)$$

The conduction band offset is given by

$$\frac{\Delta E_c}{\Delta E_g} = 1 - \frac{E_v^w - E_v^b}{E_g^b - E_g^w} \qquad (2.18)$$

where E_v^w and E_v^b are the valence band positions in the well and barrier materials, respectively, and E_g^w and E_g^b are the strain adjusted bandgaps for the well and barrier materials.

2.5.2   Harrison's model

The position of both valence and conduction bands are determined by

$$
E_v(x,y) = \begin{cases} E_v^H(x,y) + \delta E_{hh}(x,y), & \text{for hh (compressive strain)}; \\ E_v^H(x,y) + \delta E_{lh}(x,y), & \text{for lh (tensile strain)}. \end{cases} \tag{2.19}
$$

and

$$
E_c(x,y) = E_c^H + \delta E_c(x,y) \tag{2.20}
$$

where $E_v^H(x,y)$ and $E_c^H(x,y)$ are obtained by a linear interpolation of the binary parameters found in Table 2.2, and $\delta E_{hh}(x,y)$, $\delta E_{lh}(x,y)$ and $\delta E_c(x,y)$ are the strain energy shift given in Eqn (2.20) - (2.15). The superscript "H" refers to Harrison's model. The conduction band-edge discontinuity then be calculated as

$$
\frac{\Delta E_c}{\Delta E_v} = \frac{E_c^{H,b} - E_c^{H,w}}{(E_v^{H,w} - E_v^{H,b})(E_c^{H,b} - E_c^{H,w})} \tag{2.21}
$$

where the superscript w and b indicate the well and barrier materials, respectively.

2.5.3   Calculation of the band offsets for GaInNAs/GaAs Systems

Strong progress in the development of GaInNAs/GaAs devices, hardly and detailed spectroscopic studies of the band alignment of GaInNAS/GaAs quantum well structures can be found in the literature to date. Therefore the experimentally derived data [40] was used in literature for gain calculations. Recently, Lin et al [41] and Gönül et al [3] used the model solid theory for GaInNAs/GaAs as in the case of strained InGaAs materials. The authors [3, 41] have shown that model solid theory can be used to calculate the band alignments of GaIn-NAs/GaAs ignoring the presence of nitrogen in the average valence band edge energy values and taking into account the presence of nitrogen for the rest of the laser parameters. The band-alignment of matrix element InGaAs/GaAs system is determined by using Harrison's model. In Fig. 2.7, the conduction and

valence band offsets for N-free systems are shown. As can be seen from these variations both valence- and conduction-band offsets increase with increasing indium concentration.
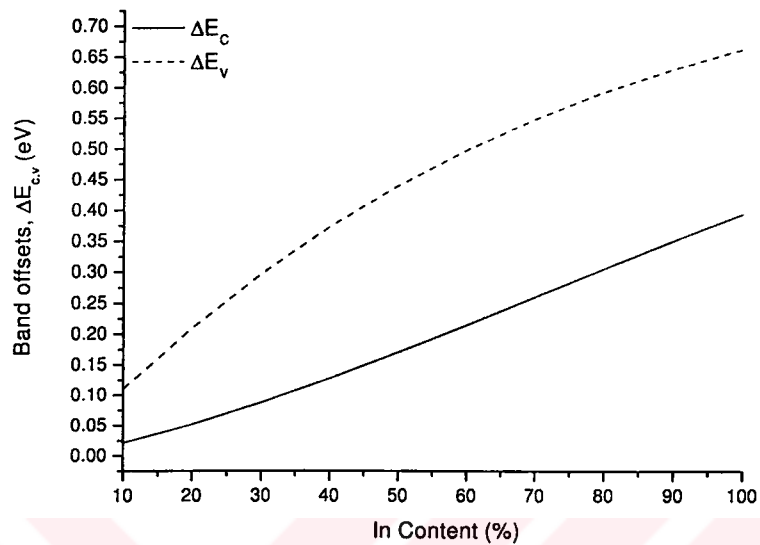
Figure 2.7: The calculated variation of the conduction and valence band offsets for InGaAs/GaAs laser system according to Harrison's model.

We use model solid theory has been used to calculate the band offsets of the GaInNAs/GaAs for small nitrogen concentration. A significant increase in conduction band offset ratio and a decrease in valence band offset ratio have been calculated with the introduction of nitrogen to InGaAs, as shown in Fig. 2.8

These results illustrate the fact that the addition of nitrogen into InGaAs leads the N-system having a band alignment of that of the ideal case (deep conduction wells and shallow valence wells) certainly. In addition, our calculations indicate that the band alignment of the N system can be calculated effectively by means of model solid theory since the calculated results are in agreement with that of the experimental results [40].
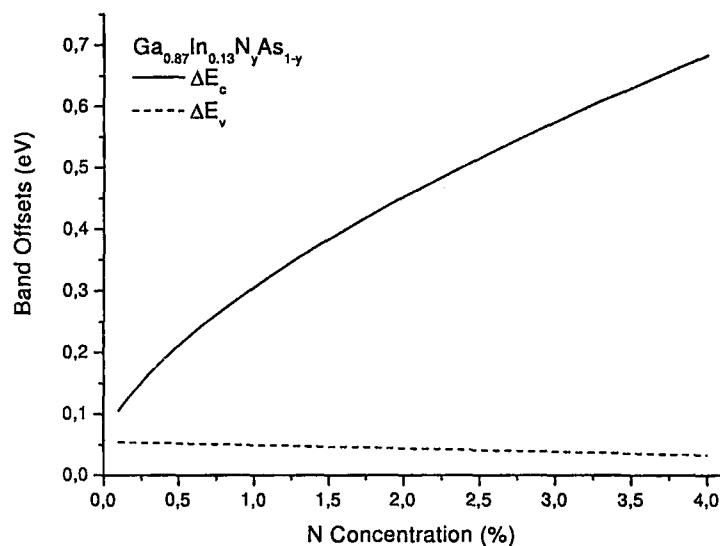
Figure 2.8: The calculated variation of the conduction and valence band offsets with nitrogen concentration GaInNAs/GaAs laser system according to model solid theory.

2.6 Conclusions

In this chapter, we review the theoretical models and provide the model calculations used through out this thesis. First of all, the effects of the adding nitrogen on InGaAs is described. The material parameters which depends on well and barrier compositions is calculated by interpolation method. The band structure and increased electron effective mass due to the interaction of the conduction band with nitrogen-related resonant states is determined by using the band anti-crossing method. These calculations implies that GaInNAs lasers can approach the ideal condition of equal electron and hole effective masses. This is important in full gain calculation modelling of laser devices.

In addition, the theoretical models and calculations for the band offset ratios for $III - V$ and $III - N - V$ material systems are presented briefly. We have shown that model solid theory can be used effectively to calculate the band alignments of N-based lasers where only experimental data available to date. The use of GaInNAs as an active material provides an efficient way to build very deep

quantum wells in the conduction band, leading to better carrier confinement and hence reduced carrier leakage at high temperatures.

Chapter 3

Pressure dependence of GaInNAs quantum well lasers

3.1 Introduction

The main motivation for the rapidly expanding fundamental and applied research in mixed anion nitride alloys is a wide range of possible optoelectronic applications for efficient light emitting devices operating within the near infrared region. Therefore, the improving of the optical quality of the alloy depends on the identification of the dominant radiative and non-radiative mechanism of light emission.

Hydrostatic pressure provides a convenient method to vary continuously the band structure of semiconductor lasers and hence to study systematically the internal electronic and optoelectronic process occurring. These include for example, such loss mechanisms as intervalence band absorption and Auger recombination which are responsible for increasing the temperature dependence of bulk $1.3 - 1.5$ μm wavelength devices used in optical fiber communication [42].

Shan et al have shown that the incorporation of N into InGaAs alloys leads to a strong interaction between the conduction band and a narrow resonant band formed by the N states due to the highly localized nature of the perturbation introduced by N atoms, resulting in a splitting of the conduction band and a

reduction of the fundamental bandgap. This is supported by the unambiguous observations of the optical transitions associated with the two branches of the split lowest conduction band in $Ga_{1-x}In_xN_yAs_{1-y}$ alloy samples with different In and N concentrations and a characteristic anti-crossing behavior of the two branches under hydrostatic pressure. The observed reduction of the bandgap energy of $Ga_{1-x}In_xN_yAs_{1-y}$ alloys with small N concentration can be fully explained by this interaction.

Fig. 3.1 shows the pressure dependence of the fundamental bandgaps of $Ga_{1-x}In_xN_yAs_{1-y}$ samples [12]. The bandgap energies were determined by photomodulated transmission (PT) measurement. In the case of $Ga_{0.92}In_{0.08}As$ ($y = 0$), the bandgap increases linearly with applied hydrostatic pressure at a rate of ≈ 100 meV/GPa. This type behavior is commonly observed for conventional group III-V semiconductors. Adding N completely changes the pressure dependence. All the $Ga_{1-x}In_xN_yAs_{1-y}$ samples exhibit a much weaker dependence of the bandgap energy at low pressure and a tendency of the energy gap to saturate at high pressures. The saturation is clearly visible in the samples with lower N concentrations. The pronounced change in the pressure dependence of the energy gap could be understood in terms of a pressure-induced transformation of the nature of the lowest conduction band states, namely, from extent to highly localized.

Knowledge of the band structure parameters is necessary for the analysis of important semiconductor properties. The band structure parameters are dependent on external perturbations such as temperature and pressure. In particular, the bandgap energy and effective masses are well known to be strongly dependent on pressure.

The aim of this chapter is to investigate the pressure dependence of the band structure parameters such as optical confinement factor Γ, effective mass, differential gain, carrier densities, threshold gain and the relative importance of these effects for strained GaInNAs/GaAs laser structure in detail.
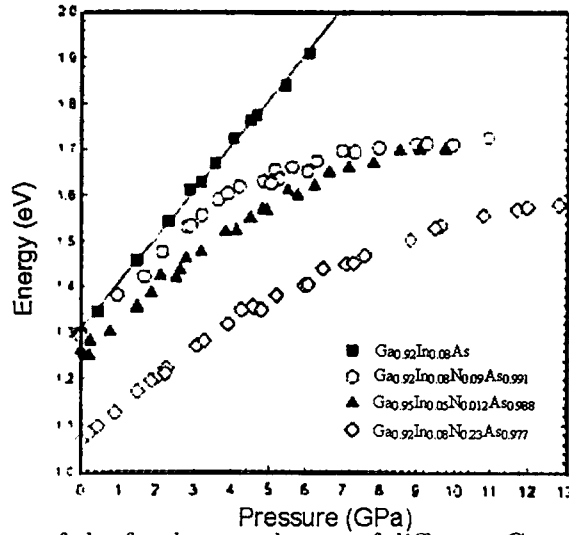
Figure 3.1: Change of the fundamental gaps of different $Ga_{1-x}In_xN_yAs_{1-y}$ samples as a function of hydrostatic pressure [12].

3.2 Pressure dependence of laser parameters

This section analysis the changes in band structure, effective mass optical confinement factor Γ, and gain related parameters with hydrostatic pressure from laser point of view.

3.2.1 Band structure

In this section, we examine the pressure dependence of the band structure of GaInNAs. The pressure coefficient of the emission energy from GaInNAs well layer can be expressed as

$$\frac{dE_{emis}}{dP} = \frac{dE_g}{dP} + \frac{dE_c}{dP} + \frac{dE_h}{dP} \tag{3.1}$$

where $\frac{dE_g}{dP}$ are the pressure coefficient of the GaInNAs bandgap, $\frac{dE_c}{dP}$ and $\frac{dE_h}{dP}$; the pressure dependence of the confinement energy for electrons and holes, respectively. In the GaInNAs/GaAs system, the incorporation of nitrogen has only minor effects on the valence band. Therefore, $\frac{dE_h}{dP}$ can be neglected. The main factor affecting $\frac{dE_c}{dP}$ are the pressure induced change of the barrier height and electron effective mass. The barrier height will increase with pressure since the

pressure coefficient of GaAs is larger than that of GaInNAs. Then the confined energy E_c will be increased. On the other hand, the increase of electron effective mass with pressure [43] will decrease the confinement energy E_c. Since the two factors have different signs and both effects are small compared to the first term in Eqn. (3.1), experimentally measured pressure coefficient for the GaInNAs-related peak should mainly reflect the pressure behavior of the GaInNAs bandgap.

The pressure dependence of GaInNAs can be explained considering the simple model of two interacting energy levels which is explained in previous chapter. The incorporation of the interaction represented by the matrix element V_{MN} leads to a mixing and anti-crossing of the extended states of the InGaAs matrix and localized N states. The two solutions of the problem was given as

$$E_{\pm} = \frac{(E_m + E_n) \pm \sqrt{(E_m - E_n)^2 + 4V_{MN}^2}}{2}. \tag{3.2}$$

The pressure dependence of the conduction band edge E_M is given by [12]

$$E_M(P) = E_0(k) + 0.1\,P \qquad\qquad eV, \tag{3.3}$$

where E_M is measured with respect to the valence band edge, P is hydrostatic pressure in units of GPa. The hydrostatic pressure dependence of the energies E_- and E_+ is shown in Fig. 3.2 along with the predicted pressure dependence of the GaInNAs conduction band edge calculated with Eqn. (3.2) and the known pressure dependence of the E_M. The energy of the nitrogen level E_N is insensitive to applied pressure [19]. The downward shift of the lower branch E_- can account well for reduction of fundamental bandgap observed in GaInNAs alloys. This demonstrates that the interaction between extended band states and localized nitrogen states is responsible for the downward shift of the conduction band edge. The pressure dependence of the E_+ transitions undergo a change opposite to E_-, i.e. the E_+ energy position weakly depends on the applied pressure at low pressures and demonstrates much stronger linear increase at high pressures.

The unusual pressure dependence of the E_- and E_+ states is attributed to the pressure induced band anti-crossing, changing the character of the states from extended to localized.
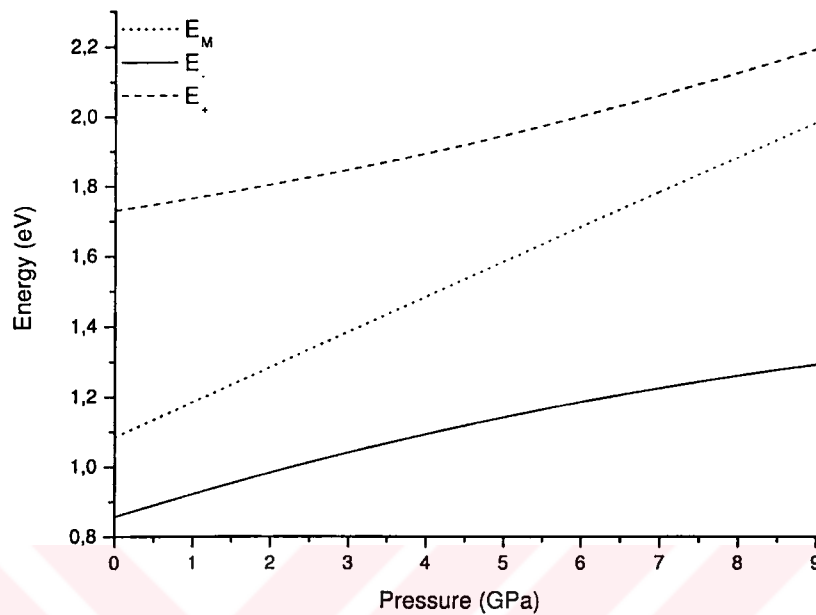
Figure 3.2: Change of fundamental gap as a function of hydrostatic pressure in units of GPa.

3.2.2   Effective electron mass

The knowledge of the carrier effective masses with pressure provides valuable information on the fundamental nature of the band states in the alloy and is also vitally important for a full exploration and optimization of III-N-V alloys in device applications.

In dispersion relation (see Fig. 2.4), the lower subband, E_-, causes the bandgap energy reduction and the flattening of the lower subband near its minimum leading to a large enhancement of the electron effective mass [5]. When hydrostatic pressure is applied the energy gap increases with increasing pressure. The changes in the band structure and changes in the ordering of the conduction band minima results an increase in effective mass m^*. Fig. 3.3 represents

the increase in the electron effective mass of GaInNAs/GaAs quantum well with increasing pressure. As can be seen from Fig. 3.3, a clear qualitative trend of the strong pressure induced enhancement in the electron effective mass induced by the presence of nitrogen in the alloy has been calculated. The effective mass increases linearly with increasing pressure.
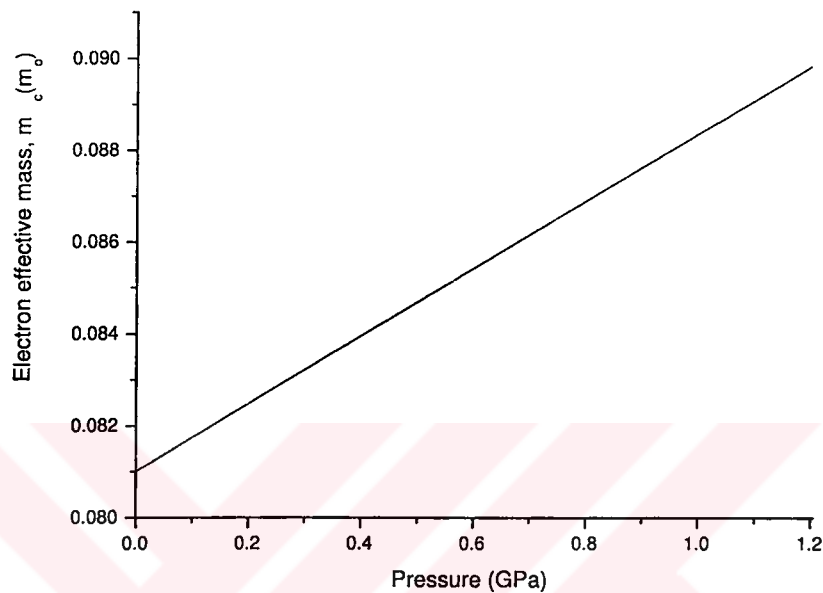
Figure 3.3: Electron effective mass versus pressure for 30% In concentration and 2% N concentration.

3.2.3   Optical confinement factor

In semiconductor lasers, the ratio of the optical power in the active layer to the total optical power is an important parameter, because it influences the lasing threshold. This ratio is called the optical confinement factor Γ and is defined as

$$\Gamma \; = \; \frac{\int_{act} \Phi^2(z)dz}{\int_{-\infty}^{\infty} \Phi^2(z)dz} \tag{3.4}$$

where Φ is the electric field amplitude.

The pressure induced increase in the direct bandgap can have significant effects on the performance of lasers operated under high pressure, such as a

reduction in Auger recombination and IVBA in long wavelength lasers. The reduction in these mechanisms occur not only because of their inherent bandgap dependences but also as a result of the changes in optical confinement factor Γ and their effect in on the threshold gain. In this section, we investigate the pressure dependence of Γ (i.e. the fraction of the optical mode power in the active region) for the separate confinement heterostructure (SCH) quantum well lasers. A five layer dielectric slab waveguide model [81] was employed to calculate Γ. The calculations have been done taking into account the index of refraction of each of the confining and barrier layers of the laser systems. The large refractive index differences between confining and barrier layers serve to confine the light and thereby provide the optical waveguide. It should be noted that the change in Γ with pressure modelled here is only due to the changes in bandgap with pressure since minor variations has been obtained in Γ due to the changes in refractive indices with pressure [44, 82]. Therefore it is assumed that the band edge refractive index does not change with pressure. Γ depends entirely on layer widths, refractive indices and propagation constant $2\pi/\lambda$, and hence on optical gap through $E = \frac{hc}{\lambda}$.

Hydrostatic pressure increases the bandgap E_g. Using the three layer waveguide model, Γ is predicted to vary with band gap E_g as

$$\Gamma \approx C_\Gamma E_g^2, \tag{3.5}$$

where C_Γ is a material constant, essentially independent of pressure. The smallest optical confinement factors are then found in long wavelength lasers, which therefore require the highest threshold gain. Since hydrostatic pressure increases the band gap E_g, we predict the largest fractional increase in optical confinement factor, Γ [44, 45] as,

$$\frac{d\Gamma}{dE_g} = 2\frac{\Gamma}{E_g} \tag{3.6}$$

The fractional change of optical confinement factor Γ with bandgap E_g is inversely proportional to the bandgap, leading to a larger pressure dependence

of optical confinement factor Γ in long wavelength lasers than in visible lasers. Using the values of optical confinement factor for five-layer dielectric slab waveguides for 2% and 3% nitrogen in GaInNAs are shown in Fig. 3.4. The increase in pressure results a linear increase in optical confinement factor. However, confinement factor decreases with increasing nitrogen concentration in quaternary material GaInNAs. The increase in nitrogen concentration results a decrease in optical confinement factor at constant pressure of 0.5 GPa, as calculated in 3.5
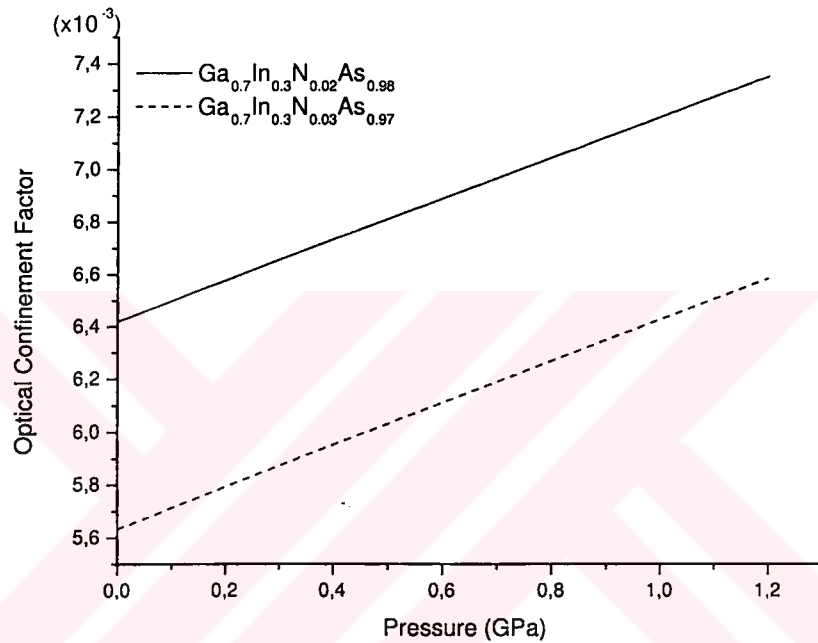
Figure 3.4: Optical confinement factor versus pressure.

3.2.4   Differential Gain

In order to highlight the effect of the conduction band effective mass on the pressure dependence of the differential gain, an idealised band model is used. This model is based on the assumption that the lasing characteristics are dominated by a single conduction band of mass m_c and a single valence band of mass m_v. The large energy separation between the valence subbands means that only the first subband is sufficiently populated to play a role. The very large effective
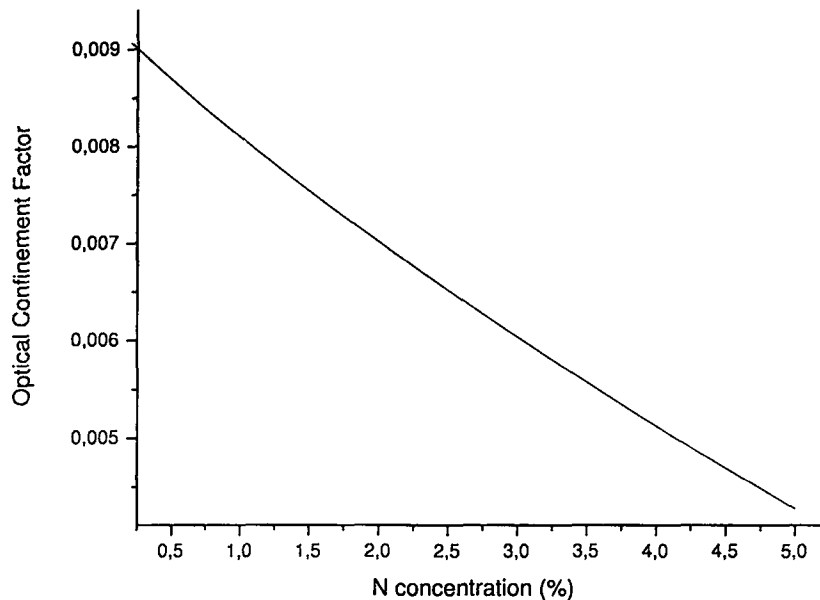
Figure 3.5: Optical confinement factor versus N concentration.

mass of the top subband means that the lower subbands are not significantly populated, despite the fact that the energy separation between the highest and second subband is typically less that 50 meV for 1.5% tensile strain [52, 53]. The model is less appropriate to lattice matched quantum well structures, and to quantum wells with moderate tensile strain where the valence band structure is strongly nonparabolic and where the second subband can play an important role. The use of realistic band structure yields higher values of the threshold carrier density than those found with parabolic approximation, because of the differing shape of the real bands. Although this simple parabolic band model ignores many features in the real band structure, it should nevertheless be useful for obtaining a theoretical trend which is in good agreement with the measurements [52]-[57].

In this section the differential gain is calculated using the parameters predicted from the band anti-crossing model presented in previous sections. In order to clarify the effect of the nitrogen concentration and the pressure on the differential gain we have calculated the differential gain and transparency carrier

concentration. The band edge peak gain, G_{max}, for electron and hole carrier density n at the quantum well band edge is given by [46]

$$G_{max} = G_0[f_c(n) - f_v(n)] \tag{3.7}$$

where

$$G_0 = \frac{\Gamma E_g \mu^2 m_r}{\epsilon_0 c n_r \hbar^3 L_z}, \tag{3.8}$$

where Γ is the optical confinement factor, E_g is the optical energy gap, μ^2 is the squared dipole moment along a given polarisation of light, m_r is the reduced mass, ϵ_0 is the permittivity in vacuum, n_r is the refractive index of the material and L_z is the well width. The quantities $f_c(n)$ and $f_v(n)$ are the Fermi occupation factors for electrons at the conduction and valence subband edges, respectively. The band edge peak gain can be rewritten using the inverted forms of Fermi occupation factors as

$$G_{max} = G_0(1 - e^{-n/n_c} - e^{-n/n_v}) \tag{3.9}$$

with

$$n_{c,v} = \frac{m_{c,v}}{\pi \hbar^2 L_z} kT \tag{3.10}$$

where $m_{c,v}$, is the conduction and valence band mass, respectively. The value of $\alpha = n_{tr}/n_c$ depends only on $R(= m_c/m_v)$. The differential gain at transparency, $\beta = dG_{max}/dn$, can be determined by differentiating the peak gain in Eqn. (3.9) with respect to carrier density as

$$\beta = \frac{dG_{max}}{dn} = G_0\left(\frac{1}{n_c}e^{-n/n_c} + \frac{1}{n_v}e^{-n/n_v}\right). \tag{3.11}$$

At transparency, $G_{max} = 0$, so the transparency carrier density n_{tr} can be determined from Eqn. (3.9) by solving

$$1 - e^{-\alpha} = e^{-\alpha/R}. \tag{3.12}$$

The value of α (n_{tr}/n_c) depends only on R.
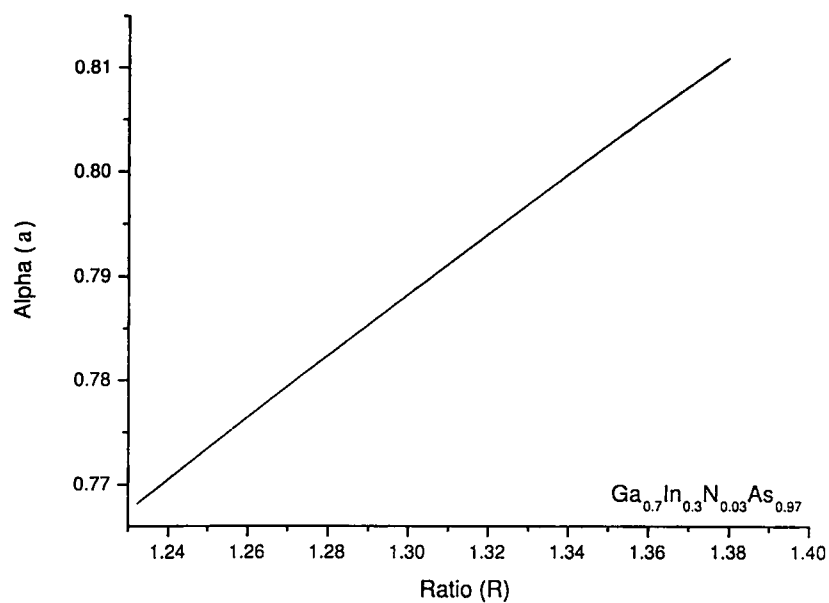
Figure 3.6: Calculated values of α (n_{tr}/n_c) versus mass ratio for 3% N concentration.
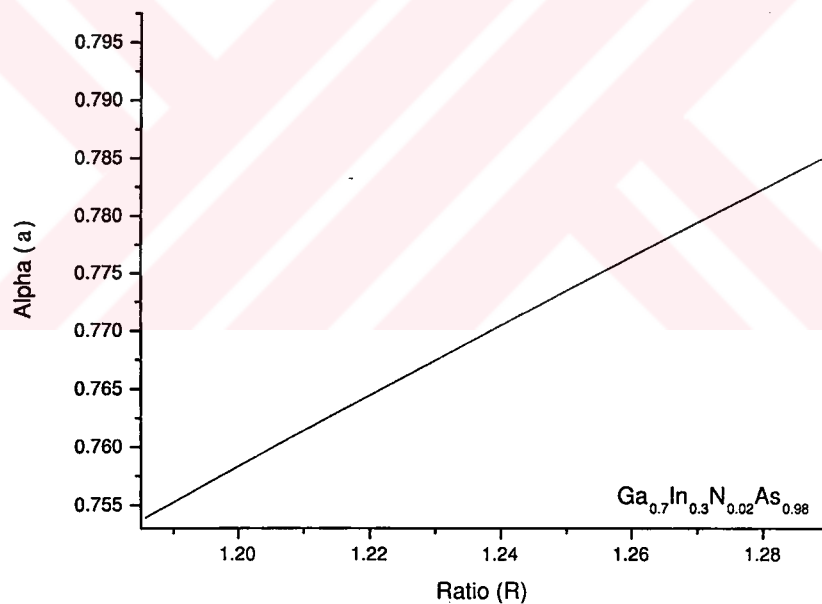
Figure 3.7: Calculated values of α (n_{tr}/n_c) versus mass ratio for 2% N concentration.

Fig. 3.6 shows the variation of α (n_{tr}/n_c) with the mass ratio (m_c/m_v) for 3 % N concentration. From this variation an increase in transparency carrier

density n_{tr} is obtained as a function of mass ratio. Fig. 3.7 illustrates the same calculations in the case of 2 % N concentration. A comparison of these two figures shows that transparency carrier density n_{tr} increases with increasing nitrogen concentration.

The differential gain can be rewritten in the following form to see the bandgap, transparency carrier density and mass ratio dependence as

$$\beta = \frac{\beta_0 E_g}{1 + R} [1 + e^{-\alpha}(R - 1)] \qquad (3.13)$$

with

$$\beta_0 = \frac{\mu^2 \pi}{\epsilon_0 c n_r \hbar k T} \qquad (3.14)$$

The change in differential gain is determined mainly due to the bandgap energy E_g and ratio R (see Eqn. (3.11)). Bandgap energy E_g increases with pressure causing an increase in differential gain β. The mass ratio R increases with pressure causing a decrease in β due to the ratio of $1/(1 + R)$ and an increase in β due to the second term in square brackets in Eqn. (3.11). In this equation $e^{-\alpha}$ tends to decrease this term due to the increase in transparency carrier density, n_{tr} with pressure P. On the other hand, $(R - 1)$ increases with pressure. The combined effect of all these gives a decrease in differential gain, as shown in Fig. 3.8. A reduction in differential gain with an increase in nitrogen concentration can also be seen from Fig. 3.8. The effective mass is another parameter, which determines the change in differential gain. The amount of this change will in turn determine the rate of change in n_{th} with pressure. The average effective mass is high in GaInNAs and this reduces the differential gain. The effect of the higher electron effective mass of GaInNAs on the differential gain can be further understood in terms of the increased density of states. Therefore, the quasi-Fermi level moves slowly with injected carriers, leading to decreased differential gain. The amount of this change will in turn determine the rate of change in threshold carrier density with pressure.

A linear relationship between carrier density and laser gain is assumed, so
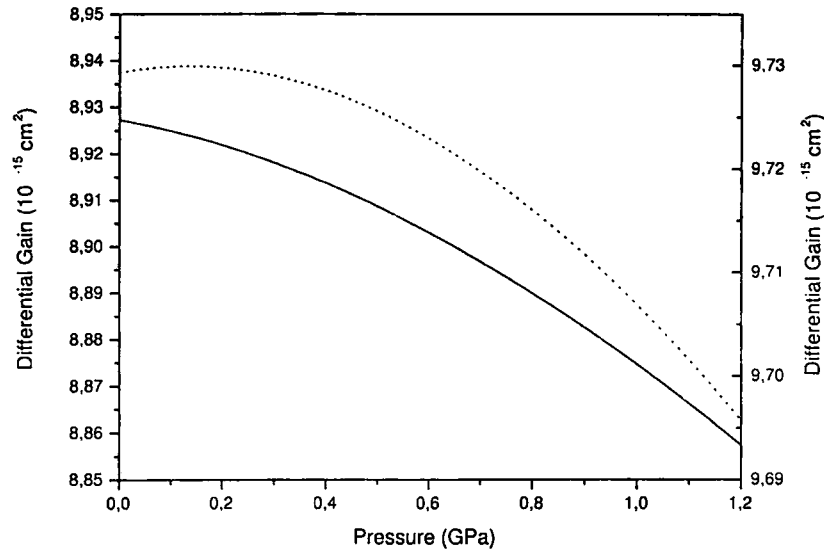
Figure 3.8: Differential gain versus pressure with different N concentration. The solid line for 3% N concentration with left y-axes and dotted line for that of 2% with right y-axes.

that the threshold carrier density n_{th} is then written by

$$n_{th} = n_{tr} + \left(\frac{g_{th}}{\beta}\right) \tag{3.15}$$

where g_{th} is the threshold material gain which takes the form

$$g_{th} = \alpha_a + \frac{1 - \Gamma}{\Gamma}\alpha_c + \frac{1}{\Gamma L}\ln\left(\frac{1}{R_m}\right) \tag{3.16}$$

where α_a and α_c are the active and cladding layer losses, L is the length of the laser and R_m is the reflectivity of the end mirrors. Since n_{tr}, β and g_{th} can be determined as a function of pressure, the pressure dependence of n_{th} can then be calculated using Eqn. (3.9) - Eqn. (3.12). These allows us to investigate the pressure dependence of n_{th} for given laser cavity parameters (laser length L, active layer thickness L_z etc.) This will in turn allow us to determine the pressure dependence of the threshold current.

Since n_{tr}, β and g_{th} as a function of pressure is determined and the pressure dependence of n_{th} can then be calculated using Eqn. (3.10) through Eqn. (3.16).
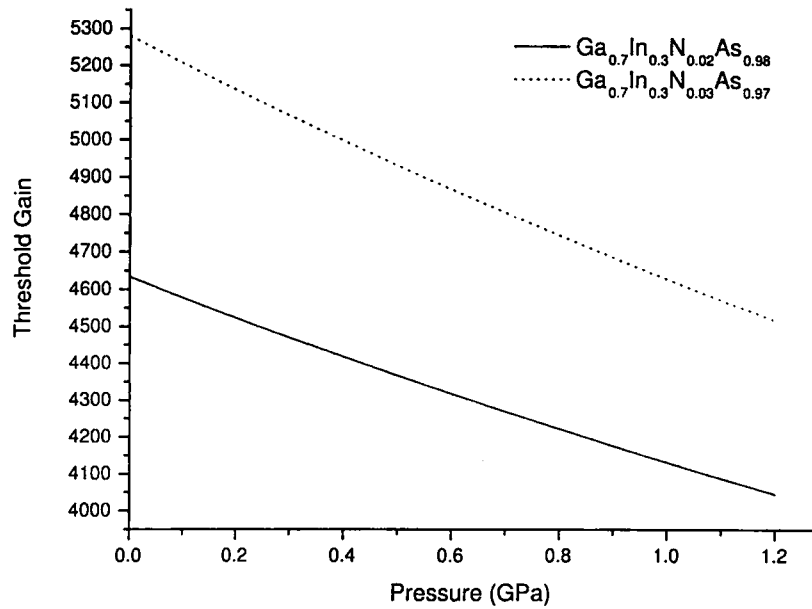
Figure 3.9: Threshold gain versus pressure.

This will in turn allow us to determine the pressure dependence of threshold current. The transparency carrier density n_{tr} increases with pressure whereas threshold gain g_{th} decreases with pressure due to the increase in Γ. Therefore, the threshold carrier density n_{th} can decrease or increase as pressure increases depending on whether the first or second term is dominant on the right hand side of Eqn. (3.15). The variation of n_{th} and n_{tr} with pressure is calculated using the calculated rate of increase of bandgap with pressure and shown in Fig. 3.2. As can be seen from Fig. 3.10 although transparency carrier density n_{tr} increases threshold carrier density n_{th} decreases with pressure for both of nitride systems. The combined effect of the increase of E_g, m_c with pressure results a decrease in threshold carrier density so do threshold current.

3.3 Conclusions

In conclusion, model calculations have been presented to investigate the effects of hydrostatic pressure on transparency and threshold carrier density for
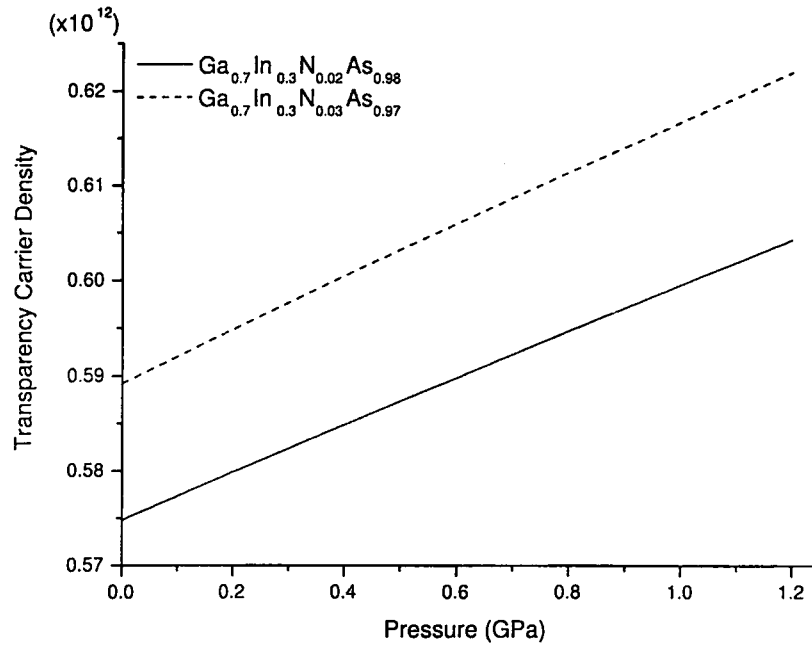
Figure 3.10: Pressure dependence of transparency carrier density for (2 - 3 % N concentration) quantum-well lasers.
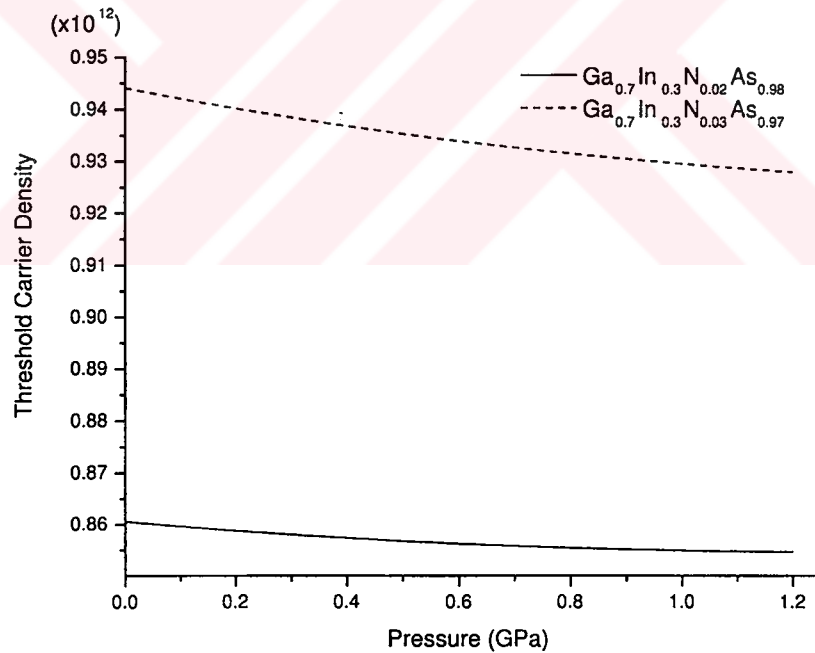
Figure 3.11: Pressure dependence of threshold carrier density for (2 - 3 % N concentration) quantum well lasers.

III-N-V systems. A detailed analysis of the pressure dependence of band structure, effective mass, optical confinement factor, peak gain and the differential gain have shown that although n_{tr} increases with pressure, n_{th} can decrease owing to the increased optical confinement factor.

Chapter 4

A theoretical comparison of pressure dependence of threshold current of phosphorus- aluminum- and nitrogen-based 1.3 μm lasers

4.1 Introduction

Due to minimum loss in optical fibre transmission, 1.3 and 1.5 μm semi-conductor lasers have attracted much attention. However, the conventional In-GaAsP/InP system exhibits a relatively low characteristic temperature due to poor electron confinement as a result of the small conduction band offset and by the presence of various loss mechanisms, like Auger recombination (AR) and intervalence band absorption (IVBA). Therefore, different material systems have been sought to improve the performance at high temperatures. Recently, Al-GaInAs/InP strained multiple quantum well (MQW) lasers have been developed to improve temperature dependence in 1.3 μm and 1.5 μm lasers by using wide bandgap barriers for the suppression of the thermal leakage [47]. Moreover, the novel material, GaInNAs on a GaAs substrate, has been proposed to solve these problems [1]. For laser applications this novel material system has several important advantages as compared to the most commonly used InGaAsP/InP

systems. First of all, a better high temperature performance of the laser structures is achieved due to a larger conduction band offset and, thus, improved electron confinement and decreased electron spill out at room temperature and above. Secondly, the increase of the electron effective mass with the addition of nitrogen provides a close match between the effective mass values for electrons and holes, beneficial for laser applications. In addition, GaInNAs gives the flexibility of tailoring the bandgap and an increase in the lattice parameter. Hence GaInNAs gives the potential to produce material lattice matched or mismatched to GaAs with a wide range of bandgap energies (from $\approx$ 1.5 eV to less than 0.8 eV) [48]. Reduced Auger recombination may also occur as a result of the larger electron effective mass and the strong non-parabolicity of the conduction band. Therefore, this work investigates how the unique features of GaInNAs/GaAs quantum wells change laser characteristics compared to conventional InGaAsP/InP and AlGaInAs/InP quantum well lasers. The dependence of the threshold current on pressure and parameters of structure are devoted to such lasers have appeared recently [49, 50].

Hydrostatic pressure can be used to continuously vary the emission energy of a laser enabling the study of bandgap dependent processes. This is a practical alternative to growing an ensemble of devices with varying material parameters and eliminates the effects that differences in growth quality and compositions between the structures may have on device performance.

We present calculations here which show that the observed differences between the three system are well explained by the calculated differences in optical confinement factor, γ, the differential gain at transparency and the carrier density at threshold. We extend our analysis to estimate the magnitude of the Auger coefficients and obtain the variation of the radiative and non-radiative part of the threshold current with pressure. We thus provide further insights into the factors influencing the threshold current density dependence of the devices operating at 1.3 μm.

Chapter 4 is organized as follows. In section 4.2, the three laser structures are described. We present the models that we have used in our calculations in section 4.3. The necessary comments on the validity of these approximate models are made to explain the basic physical properties of the laser systems under investigation. In section 4.4, we calculate the pressure dependence of the optical confinement factor for seperate confinement heterostructures using a five layer dielectric wavequide model. Section 4.5 provides a comparison of the effect of the variation of transparency carrier density, threshold gain and differential gain on threshold carrier density for each of the laser system. The predicted pressure dependence of both the radiative current and non-radiative Auger current for each system is given in section 4.6. Finally our conclusions are summarized in section 4.7.

4.2   Laser structures

We consider three different laser structures operating around 1.3 μm wavelength for comparison. The first type of device studied is P-based lasers which consists of unstrained $Ga_{0.33}In_{0.67}P_{0.28}As_{0.72}/Ga_{0.1}In_{0.9}P_{0.78}As_{0.22}/$InP quantum wells. The second type of device is Al-based lasers with $Al_{0.175}Ga_{0.095}In_{0.73}As$ / $Al_{0.27}Ga_{0.21}In_{0.57}As$ / InP structure parameters and the well is 1.4 % compressively strained. The third type of device is N-based lasers with 1.7 % compressively strained $Ga_{0.7}In_{0.3}N_{0.022}As_{0.098}$ quantum wells between GaAs barriers and $Al_{0.1}Ga_{0.9}As$ cladding layers. The quantum well thickness and cavity length in all structures is taken as 6 nm and 610 μm, respectively.

4.3   Pressure dependence of radiative and non-radiative threshold current

4.4   The models

In this section, we present the models which enables us to determine the threshold characteristics, radiative and Auger related non-radiative threshold current of 1.3 μm P-, Al-, and N-based lasers and their variation with pressure. Our models provide the first clear comparison of the parameters of structures and will enable us to predict optimum quantum well laser structures. For the band structures of P- and Al-based lasers, the material parameters except for the electron effective mass of GaInPAs and bandgap energies [51] are linearly interpolated from those of binary materials [30]. The band alignment for P- and Al-based lasers are derived from Harrison's model [51] whereas an experimental derived data is used for N-based lasers [5].

4.4.1   The radiative and non-radiative threshold current models

The total current injected in a quantum well can be written as

$$I = eV[A\ n_{th} + B\ n_{th}^2 + C\ n_{th}^3],\tag{4.1}$$

where V is the pumped volume of the active region, which is calculated by multiplying the surface area of the contact stripe by the total quantum-well thickness and e is the electronic charge. A is the monomolecular recombination coefficient, describing recombination through defects. B is the coefficient describing the direct radiative recombination of an electron in the conduction band with a hole in the valence band, which is, therefore, a bimolecular process and hence proportional to n_{th}^2[58]. Auger recombination involves three carriers (hence, $I_{Aug} \approx n_{th}^3$) and is described by the Auger coefficient C.

4.4.2   Radiative current

The radiative part of the threshold current density can be written as

$$J_{th} \approx B \, n_{th}^2 \qquad (4.2)$$

where B is the bimolecular radiative recombination coefficient between electrons and holes and is band structure dependent. B can be estimated analytically, using Maxwell-Boltzmann statistics, and assuming strict k selection [59]

$$B = \frac{e^2 \, L_z}{\epsilon_0 \, m_0^2 \, c^3 \, kT} \frac{n \, E_g \, \langle M_{av}^2 \rangle}{m_v \, (1 \, + \, R)} \qquad (4.3)$$

where $\langle M_{av}^2 \rangle$ is the squared momentum matrix element averaged over all polarizations of light, which is assumed here not to vary with wavevector k and pressure. Therefore, the radiative threshold current can be assumed to vary as

$$J_{th} \propto \frac{E_g}{1 \, + \, R} n_{th}^2. \qquad (4.4)$$

4.4.3   Non-radiative loss mechanism

Long wavelength lasers operating at $1.3 - 1.55$ μm wavelengths suffer from significant intrinsic losses such as intervalence band absorption (IVBA) and Auger recombination (AR). These intrinsic losses increase as the emission wavelength gets longer. With decreasing energy gap E_g, the spin orbit splitting energy Δ_0 becomes closer and closer to E_g. This enhances the probability of Auger transitions in the valence band as well as intervalence band absorption [60]. In addition, the influence of intervalence band absorption and non-radiative Auger recombination can amplify each other [42]. Large internal optical absorption losses increase the threshold carrier concentration, which in turn leads to increased Auger losses. As a result of these losses, long wavelength devices have a high threshold current, low efficiency and high temperature sensitivity.

The intervalence band absorption (IVBA) is a mechanism that has been proposed as a possible cause of this sensitivity of threshold currents in the longer-wavelength semiconductor lasers used for optical fibre communications. The intervalence band absorption process the emitted radiation is re-absorbed by the excitation of an electron from the split-off band to an empty state in the heavy-hole band. This is most likely caused by valence-band structure which reduces the in-plane effective mass of the holes considerably and, as a consequence, reduces the transition probability for the IVBA process. Without intervalence band absorption the threshold carrier density decrease slightly, and so therefore does the amount of Auger recombination.
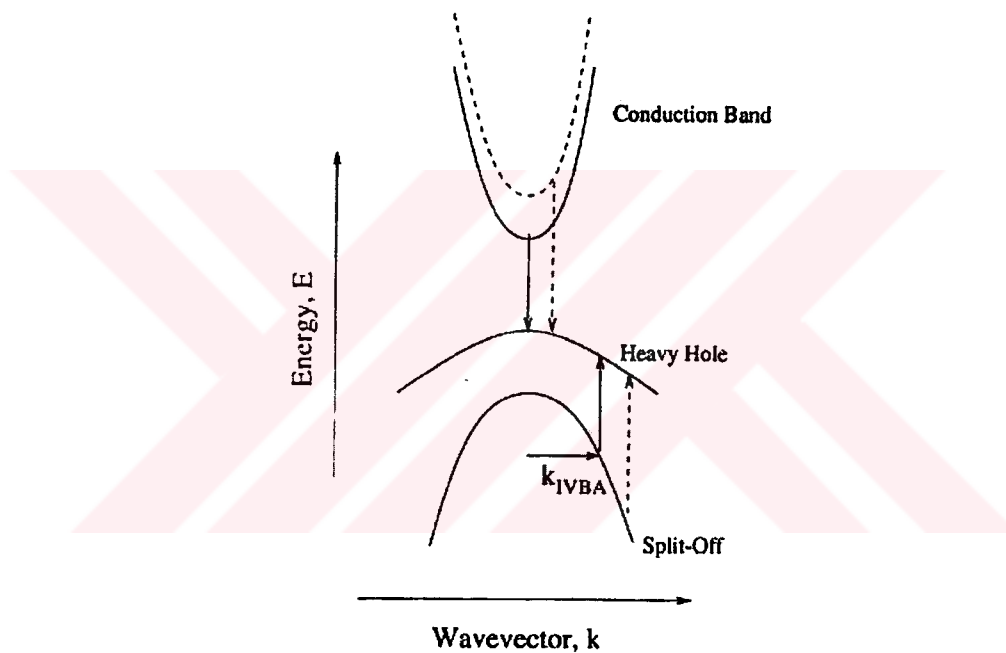
Figure 4.1: Schematic representation of intervalence band-absorption.

In Fig. 4.1, the dotted arrows indicate how IVBA moves to larger wavevector k and is thereby reduced with increasing bandgap. IVBA occurs when the photon is subsequently re-absorbed by lifting an electron from the spin-split-off band into an injected hole state in the heavy-hole band. The intervalence band absorption process (IVBA) is illustrated by the solid vertical arrows in Fig. 4.1, whereby an electron in the conduction band recombines with a hole near the valence band maximum, creating a photon of energy $h\nu$, close to the bandgap

energy E_g. The solid vertical arrow indicate the IVBA process, while the dotted lines indicate the case for shorter wavelength lasers. The absorption increases the gain required at threshold and hence increases the threshold carrier density n_{th} leading to an increase in threshold current density.

Auger recombination is a non-radiative recombination process whereby electrons and holes recombine across the energy gap, with the energy released exciting a third carrier: either an electron higher into the conduction band or hole into the valence band. There are two possible Auger recombination mechanisms: band-to-band [61] and phonon-assisted [62, 63], both have been widely investigated for both bulk semiconductors [64]-[66] and quantum wells [67]-[69].
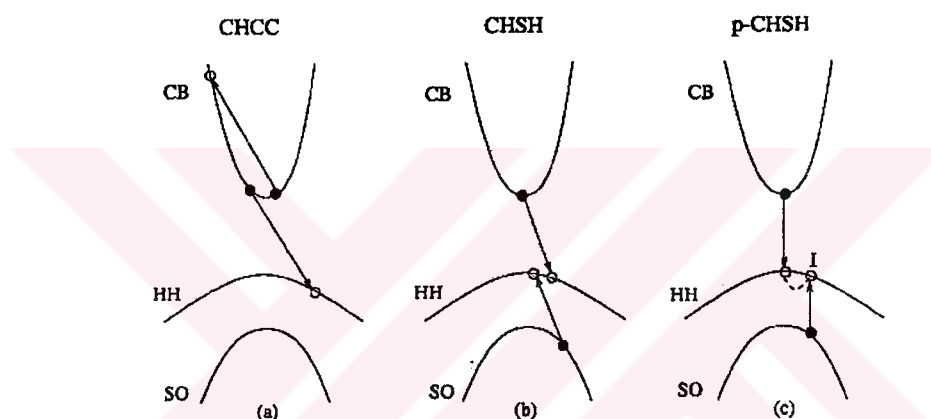
Figure 4.2: Band to band Auger recombination process shown schematically for a quantum well laser. (a) The direct - CHCC process, (b) CHSH process, (c) A phonon-assisted CHSH Auger transition.

Four main types of Auger recombination processes are generally considered in semiconductor lasers. Examples of the two major band-to-band Auger recombination (AR) processes are illustrated in Fig. 4.2. When an electron and hole recombine, they can transfer their energy and momentum to another electron by lifting it higher into the conduction band. This is called the CHCC process (C stands for the conduction band, H and S stand for the heavy-hole and split-off valence bands, respectively) and is illustrated in Fig. 4.2 (a). Alternatively, a hole can be excited deeper into the valence band. This is most likely to involve the spin-split-off band, as shown in Fig. 4.2 (b) and is then called the CHSH pro-

cess. Many other possible Auger processes may occur, including phonon-assisted Auger, for which the CHSH process, the electron excited from the split-off band passes through a forbidden intermediate state (I), and is then scattered with the absorption or emission of a phonon to the final state is illustrated in Fig. 4.2 (c). The phonon allows conservation of energy and momentum in the overall process. We investigate the role of Auger processes with the application of hydrostatic pressure that increases the direct energy gap E_g. The radiative current increases approximately as E_g^2 in an ideal quantum well laser [70]. In contrast, the Auger recombination current is very sensitive to the energy gap, decreasing rapidly with increasing E_g. Auger recombination has a rate that can be approximated for band-to-band processes as by

$$J = C_r n^3 e^{-E_a/k_B T}, \tag{4.5}$$

where C_r is a complicated expression determined by the band structure and optical matrix elements, n is the carrier density, k_B is Boltzmann's constant, T is the absolute temperature, and E_a is the activation energy which can be written for CHCC process as

$$E_a = \frac{m_c}{m_c + m_{hh}} E_g, \tag{4.6}$$

and for the CHSH process

$$E_a = \frac{m_s}{2m_{hh} + m_c - m_s}(E_g - \Delta), \tag{4.7}$$

assuming parabolic bands and Boltzmann statistics. Therefore, the activation energy is inversely proportional to the valence band heavy-hole effective mass. Thus, it was predicted by Adams [71] that a reduction in m_{hh} due to the incorporation of compressive strain into a laser device would reduce the Auger recombination rate due to an increase in the activation energy E_a. The activation energy for AlGaInAs/InP systems is larger than that for 1.55 μm GaInAsP/InP lasers [72] and smaller than that for 1.3 μm GaInAsP/InP lasers [73].

4.4.4   Non-radiative Auger current

In Auger recombination an electron and hole recombine across the bandgap and excite a third carrier into the valence or conduction band. Thus, the transition does not generate any photons. In this process, three active carriers are made unavailable for lasing. So, it is an undesirable process in semiconductor lasers because it makes reduction of threshold current difficult. As a result of three carriers being involved, the Auger term varies as n_{th}^3. The threshold current density is then simply given by

$$J_{th} \approx C\, n_{th}^3 \qquad\qquad (4.8)$$

where C is the Auger recombination coefficient. This expression is based on Boltzmann statistics and parabolic conduction and valence band and assumes therefore that the Auger term C is not carrier density dependent. The Auger recombination process in semiconductors can either be direct [61] or phonon assisted [62, 63]; both have been widely investigated for both bulk semiconductors [64]-[66] and quantum wells [67]-[69]. The CHCC and CHSH Auger processes are believed to be the two dominant processes in long wavelength devices. The pressure dependence of the threshold current will depend both on the pressure dependence of the non-radiative recombination coefficient C and on the threshold carrier density n_{th}. We have calculated the pressure dependence of the different Auger processes, using expressions from the literature based on parabolic bands and Boltzmann statistics. Auger recombination processes have been investigated by many authors [58, 64],[74]-[78]. In most of these works, analytical expressions of the Auger recombination coefficients under different conditions were derived. The usual assumptions behind these expressions are

- parabolic and isotropic bands,

- Boltzmann statistics and

- a constant transition matrix element.

It should be admitted that the validity of these assumptions is questionable. The valence subbands in particular are often far from being parabolic and the accuracy with which Boltzmann statistics represents the carrier occupancy will decrease with increasing carrier density. On the other hand, it is very difficult to calculate accurately the Auger transition rates in real systems because of the complexities involved in integrating over a large portion of the band structure, uncertainities in the band structure itself, and in the matrix elements. The use of a realistic band structure yields smaller values of the Auger coefficients than those found with parabolic approximation [78], because of the differing shape of the real bands. Although the parabolic approximation ignores many features in the real band structure, it should nevertheless be useful for obtaining an order of magnitude estimates of the Auger coefficients and their bandgap dependence.

4.4.5 Direct Auger processes

The direct Auger recombination rate can be expressed as

$$C_d = C_o e^{-\frac{E_a}{k_b T}} \tag{4.9}$$

where E_a is the activation energy [73]. The minimum activation energy E_a and coefficient C_0 for the CHCC direct Auger process can be written as

$$E_a(CHCC) = \frac{m_c E_g}{m_c + m_{hh}}, \tag{4.10}$$

$$C_0(CHCC) = \frac{4\pi}{\hbar} \frac{e^4}{\epsilon^2} \frac{m_c(m_{hh} + m_c)}{(2 m_{hh} + m_c)^2} \frac{|M_{ee}|^2}{k_b T} \tag{4.11}$$

where m_{hh} is the valence band heavy hole mass. $|M_{ee}|$ is the matrix element of the electron-electron interaction which can be taken for the CHCC process as [77]

$$|M_{ee}|^2 = \left(\frac{\hbar^2}{2m_0}\right)^2 \frac{m_0}{m_c} \frac{E_p}{3 E_g^3} \tag{4.12}$$

Inserting Eqn. (4.10)-Eqn. (4.12) into Eqn. (4.9) and considering only pressure-

dependent terms, the direct Auger recombination rate for the CHCC process becomes

$$C_d(CHCC) \propto \frac{m_0(m_{hh} + m_c)}{(2m_{hh} + m_c)^2} \frac{1}{E_g^3} \exp\left(-\frac{m_c}{m_c + m_{hh}} \frac{E_g}{k_b T}\right) \tag{4.13}$$

Using the same model, the activation energy and coefficient C_0 for the direct CHSH Auger process can be written as

$$E_a(CHSH) \propto \frac{m_s(E_g - \Delta)}{2m_{hh} + m_c - m_s} \tag{4.14}$$

$$C_0(CHSH) = \frac{4\pi}{\hbar} \frac{e^4}{\epsilon^2} \left(\frac{m_{hh}}{m_v}\right)^2 \frac{m_s(2m_{hh} + m_c - m_s)}{(2m_{hh} + m_c)^2} |M_{ee}|^2 \tag{4.15}$$

with the matrix element

$$|M_{ee}|^2 = \left(\frac{\hbar^2}{2m_0}\right)^2 \frac{f_{CH} f_{SH}}{E_g \Delta} \tag{4.16}$$

where f_{CH} and f_{SH} are oscillator strengths which can be represented in the Kane model by [79]

$$f_{CH} = \frac{E_p}{3E_g} \tag{4.17}$$

$$f_{SH} = \frac{E_p}{3\Delta (E_g + \Delta)} \frac{\hbar^2 k_2^2}{2m_0} \left(1 + \frac{m_s}{m_0}\right) \tag{4.18}$$

where E_p is the energy equivalent of the momentum matrix element which is evaluated for different semiconductors by Lawaetz [80]. Here k_2 is the solution of

$$E_g - \Delta - \varepsilon_s(k_2) = 0 \tag{4.19}$$

where ε_s is the energy of the spin-split-off band. Thus $|M_{ee}|^2$ can be written as

$$|M_{ee}|^2 = \left(\frac{\hbar^2}{2m_0}\right)^2 \frac{E_p^2}{9E_g \Delta(E_g + \Delta)} \tag{4.20}$$

Similarly, the pressure dependence of the direct CHSH Auger rate can be found

by inserting Eqn. (4.20), Eqn. (4.15) and Eqn. (4.14) into Eqn. (4.9).

$$C_d(CHSH) \quad \propto \quad \left(\frac{m_{hh}}{m_v}\right)^2 \frac{m_s(2m_{hh} + m_c - m_s)}{(2m_{hh} + m_c)^2} \frac{1}{E_g \Delta^2 (E_g + \Delta)}$$

$$x \quad \exp\left(-\frac{m_s}{2m_{hh} + m_c - m_s} \frac{E_g - \Delta}{k_b T}\right) \tag{4.21}$$

where m_{lh} and m_s are the mass of the light hole and spin-split-off band, Δ the spin-split-off energy and $m_v = m_{hh} + m_{lh}$. It is clear from the above equations that the relative strengths of these processes are heavily dependent on the bandgap and effective masses.

4.4.6   Phonon-assisted Auger processes

The strong band structure dependence of the direct Auger processes arises from the conservation laws of energy and momentum. The additional momentum conservation in direct Auger processes gives rise to an activation energy for the process. As can be seen from Eqn. (4.10) and Eqn. (4.15), activation energy depends strongly on bandgap. In the absence of momentum conservation, there is no activation energy. Thus the strong band structure dependence will not appear if the momentum conservation is not satisfied. In the phonon-assisted Auger processes conservation of momentum can be fulfilled by the phonon. As a consequence, one may expect that the influence of the band structure is less important in phonon assisted Auger processes.

The phonon-assisted Auger recombination rate is given by Haug [68] as

$$C_p \quad = \quad \frac{A}{2\hbar^3}\left(\frac{4\pi e^2}{\varepsilon}\right)^2 m_{hh}\bar{\mu}\frac{|M_{ep}|^2 \; |M_{ee}|^2}{e^{\hbar\omega/k_B T} - 1}\left[\frac{1}{(\bar{\mu}\bar{E}_g + \hbar\omega)^2} + \frac{e^{\hbar\omega/k_B T}}{(\bar{\mu}\bar{E}_g - \hbar\omega)^2}\right] \tag{4.22}$$

with

$$\bar{E}_g \quad = \quad E_g \qquad \bar{\mu} \quad = \quad m_c/m_{hh} \tag{4.23}$$

for the CHCC process and

$$\bar{E}_g \quad = \quad E_g - \Delta \qquad \bar{\mu} \quad = \quad m_s/m_{hh} \tag{4.24}$$

for the CHSH process. A is the area of the quantum well, μ E_g is the kinetic energy associated with the forbidden intermediate state and $\hbar\omega$ is the phonon energy. In addition to electron-electron interaction M_{ee}, in this case the electron-phonon interaction M_{ep} is involved and this is described by [77]

$$|M_{ep}|^2 \;=\; \frac{\Omega_0}{AL_z} \frac{D^2 \hbar\omega}{2Mv_s^2} \tag{4.25}$$

where D is the deformation potential, v_s is the velocity of the sound and M is the sum of the masses of the atoms in the elementary cell of volume Ω_0. The matrix element for the electron-electron interaction $|M_{ee}|$ is given by Eqn. (4.12) and Eqn. (4.16) for the CHCC and CHSH Auger processes, respectively. Therefore, the pressure dependence of the CHCC Auger rate can be derived by substituting Eqn. (4.24), Eqn. (4.25) and Eqn. (4.12) into Eqn. (4.22), giving

$$C_p(CHCC) \;\propto\; m_0 \left(\frac{m_{hh}}{m_c}\right)^2 \frac{1}{E_g^5} \tag{4.26}$$

Similarly, substitution of Eqn. (4.24), Eqn. (4.25) and (4.20) into Eqn. (4.22) yields

$$C_p(CHSH) \;\propto\; \frac{m_{hh}^2}{m_s} \frac{1}{E_g \Delta^2 (E_g + \Delta)(E_g - \Delta)^2} \tag{4.27}$$

4.5 Comparison of the optical confinement factors

The change in optical confinement factor with pressure for the three competing structure is calculated according to the five layer waveguide model and shown in Table 4.1. Γ increases with pressure since hydrostatic pressure increases the bandgap. Γ is predicted to vary with bandgap as

$$\Gamma \;\approx\; C_\Gamma E_g^2 \tag{4.28}$$

according to the three layer waveguide model [56]. C_Γ is a material constant and

		GaInNAs/GaAs	GaInAsP/InP	AlGaInAs/InP
$\frac{dE_g}{dP}$	(meV/GPa)	86	86	89
$\Gamma\%$	(0 GPa)	0.642	0.930	1.046
	(1.2 GPa)	0.736	1.036	1.165
$\frac{1}{\Gamma}\frac{d\Gamma}{dP}$	(GPa^{-1})	0.146	0.114	0.113

Table 4.1: The values of the optical confinement factor Γ calculated at 0 GPa and 1.2 GPa using a five-layer dielectric slab wavequide model. $\frac{dE_g}{dP}$ is the pressure coefficient of the bandgap and $\frac{1}{\Gamma}\frac{d\Gamma}{dP}$ is the increase in Γ with pressure

is essentially independent of pressure. This explicit relation of Γ with bandgap according to the three layer waveguide model [83, 84] explains the pressure dependence of Γ.

The smallest optical confinement factors have been calculated for the N-based laser system and the highest optical confinement factors correspond to the Al-based laser system. It should be noted from Table 4.1 that, although the N-based system has the lowest Γ, the increase in optical confinement factor with pressure, i.e. $\Gamma^{-1}\ d\Gamma/dP$, is the fastest one in N-based system compared to the other two laser system.

4.6   Comparison of threshold carrier densities

Fig. 4.3 shows the variation of the transparency carrier density with pressure for the three competing laser systems. Firstly, n_{tr} increases with pressure owing to the increase in m_c for a fixed m_v which is assumed to be independent of pressure, as experiments show it to have only a very small pressure dependence even in strained structures [85]. Secondly, although the three laser systems have comparable transparency carrier densities, Al- based system has the lowest transparency carrier density, followed by N-based and P-based systems, successively. The N-based system has higher transparency carrier density than that of the Al-based system due to the larger electron effective mass. The value of the effective mass is directly related to the densities of states and result in higher transparency carrier density in N-based system. The increase in electron effec-
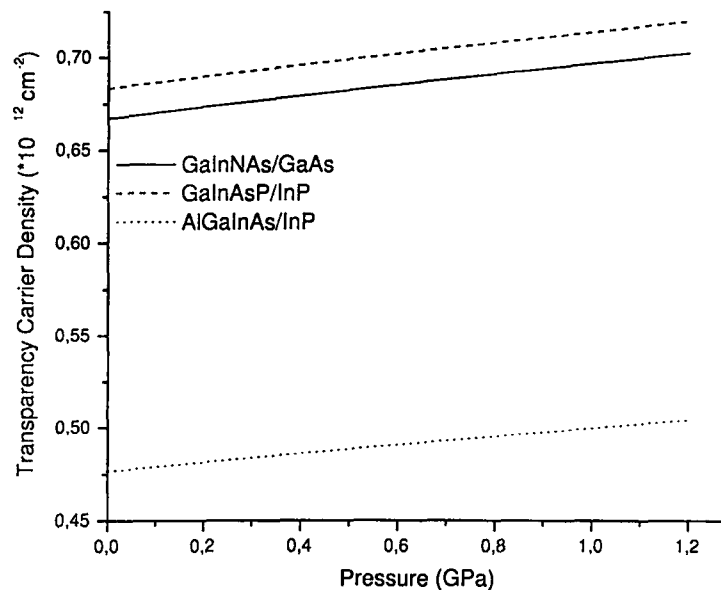
Figure 4.3: The pressure dependence of the transparency carrier density n_{tr} of $N-$, $P-$ and Al-based laser systems.

tive mass provides a close match between the density of states of the conduction and valence band. In other words the strong conduction band/valence band asymmetry has been removed in N-based system. However this will not induce a decrease in transparency carrier density. Since the overall effect is not only determined by the reduced conduction band/valence band asymmetry but also the reduced density of states in both valence and conduction band. The reduced conduction band/valence band asymmetry cause the Fermi levels to move symmetrically with injected carrier concentration, however the densities of states is increased due to the increase in conduction band effective mass.

The variation of threshold gain with pressure for the three modelled structures is shown in Fig. 4.4. Due to the lower optical confinement, N-and P-based laser systems require higher threshold gains. On the other hand, the differential gain β of the N-based system is greater than that of the both P-based and Al-based systems as shown in Fig. 4.5. The uncommonly large electron effective mass in N-based system improves the matching between the conduction band/valence band asymmetry and provide this system having the largest
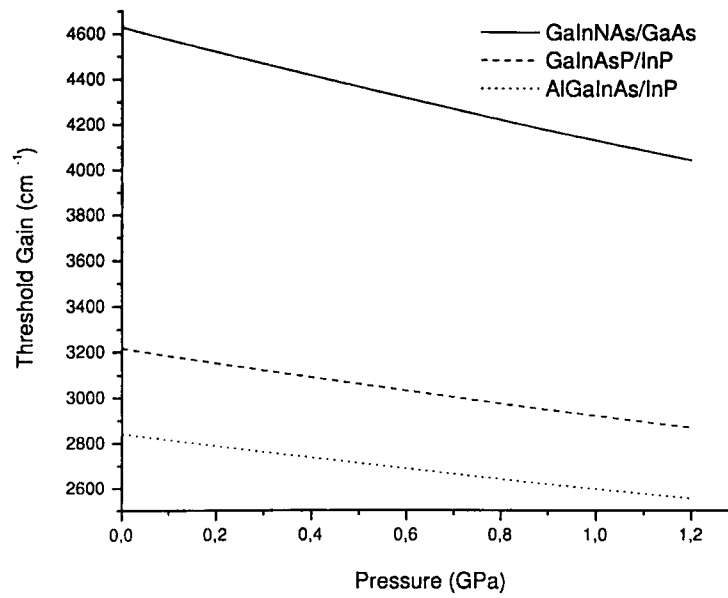
Figure 4.4: The variation of the threshold current with pressure of $N-$, $P-$ and Al-based laser systems.

differential gain which further implies high speed modulation.
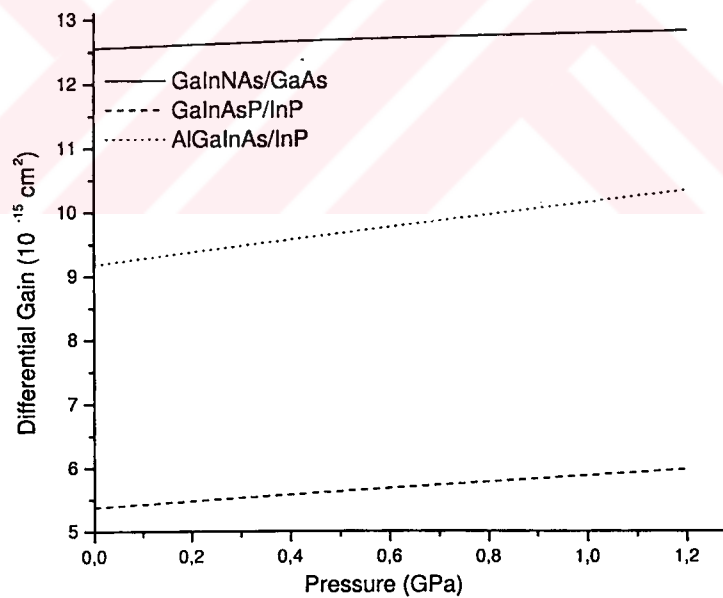
Figure 4.5: The calculated pressure dependence of the differential gain of three competing laser devices.

Fig. 4.6 present the variation of threshold carrier density n_{th} with pressure
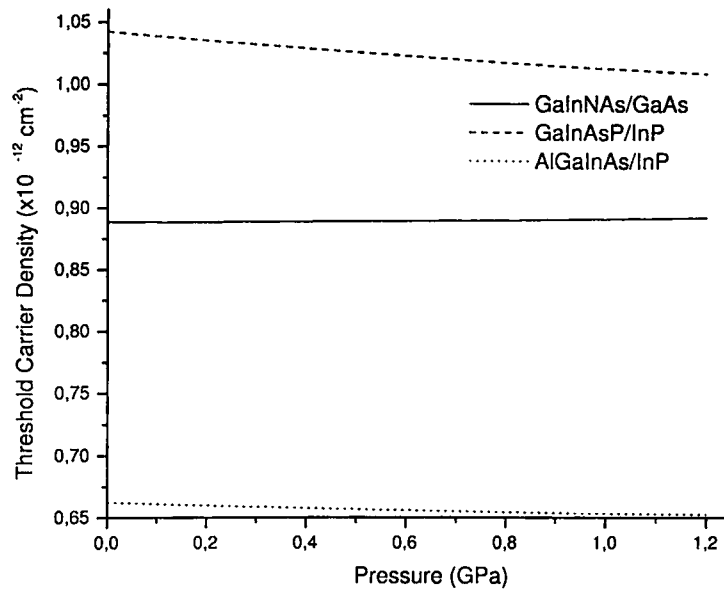
Figure 4.6: The threshold carrier density as a function of pressure for $N-$, $P-$ and Al-based laser systems.

for the three modelled laser systems. It is apparent from these variations that Al- and N-based lasers are superior to P-based lasers with Al-based laser system offering the optimum structure possessing the lowest n_{th}. It is interesting to note from Fig. 4.6 that n_{th} of P- and Al-based laser systems decreases with pressure with rapid reductions calculated in P-based lasers. These reductions are due to the increase in Γ and β and the decrease in threshold gain with pressure. On the other hand, n_{th} of N-based laser system increases with pressure owing to the increase in m_c which further increasing the band edge density of states.

To understand the pressure dependence of peak gain, we compare the peak gain of the three competing laser systems for a carrier density of $2x10^{12}$ cm^{-2}. As can be seen from Fig. 4.7, the peak gain of the Al-based system has the highest value and it increases with pressure. This system system has the highest optical confinement factor. For the transparency and threshold, Al-based system shows the lowest carrier density. Such improved laser properties makes the Al-based system as an ideal candidate for low power and low threshold applications. The calculated CB offsets ($\Delta E_c/\Delta E_g$) at 300 K are 0.55 for P-based system and

0.71 for Al-based system according to the Harrison's model. Note that both are smaller than that of the GaInNAs which is 0.80 [40]. The improved CB offset leads to temperature-insensitive properties. Therefore, combined with the high differential gain, N-based laser is an ideal candidate for high speed applications.
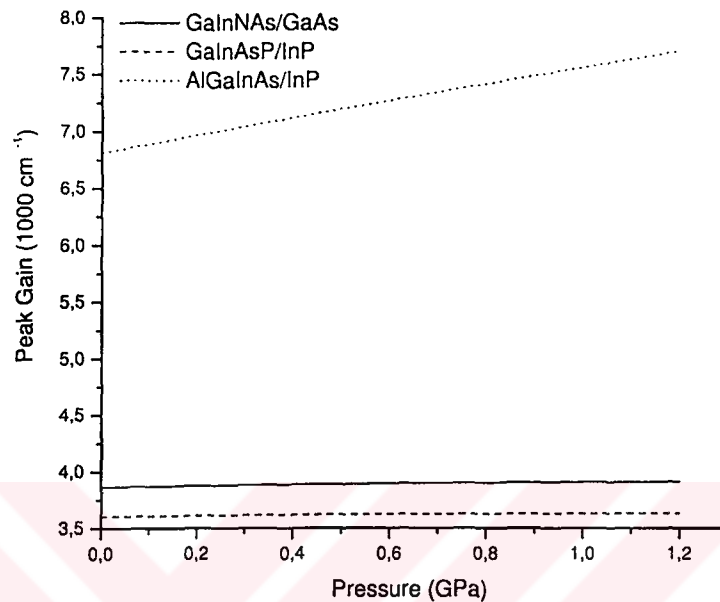
Figure 4.7: The variation of peak gain with pressure for the modelled laser devices.

4.7   Comparison of threshold currents

Two recombination processes, radiative recombination and nonradiative Auger recombination (AR), are dominant in semiconductors at high excitation levels. The current of Auger recombination constitutes a significant part of the total threshold current in P-based lasers. The Auger current not only affects the laser threshold current but also its temperature dependence. The stronger the temperature dependence of the AR rate, the lower the characteristic temperature and the lower stability of the laser. Therefore, in this section we provide a comparison of the influence of both threshold carrier density and the radiative and non-radiative recombination coefficients B and C, respectively, on the pressure

dependence of the threshold current of the three competing laser devices. The calculated variation of the radiative part of the threshold current with pressure is shown in Fig. 4.8.
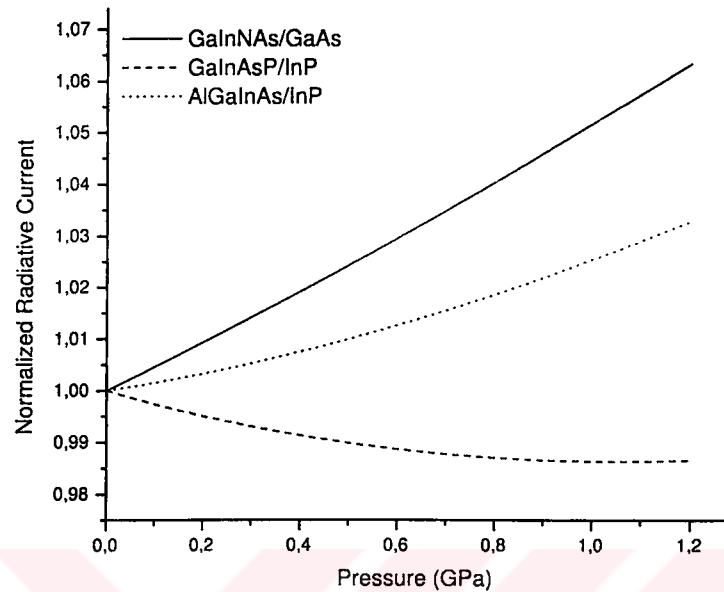
Figure 4.8: Pressure dependence of the radiative current density of N-, P- and Al-based laser systems.

We see that B always increases with increasing E_g owing to pressure, with the overall behavior of the threshold current density J_{th} depending also on the relative change in the threshold carrier density. The radiative threshold current of N- and Al-based lasers increases with pressure; however the increase of N-based lasers is much faster than the Al-based lasers. This is due to the fact that the threshold carrier density n_{th} increases with pressure in N-based lasers whereas n_{th} decreases with pressure in Al-based devices. On the other hand, the radiative threshold current of P-based lasers decreases with pressure. This decrease is due to the decrease in n_{th} in this P-based device, which offsets the increase in B completely. This is in agreement to what is observed experimentally [86], implying that radiative recombination is not the dominant current mechanism in these P-based lasers.

In a loss free laser, one would generally expect the radiative threshold

current to increase with pressure as bandgap increases [87]. P-based laser devices show a remarkable decrease in threshold current with pressure. This decrease has been attributed to the reduction in Auger recombination. Thus, the variation of threshold current with pressure gives a measure of the relative strength of the AR in each of the competing laser structures. We assign the reduction in threshold current to a combination of two effects:

- a change in the carrier density (increase or decrease) brought about by the pressure dependence of the gain-carrier density relation and

- the pressure dependence of the Auger coefficient.

Fig. 4.9 - Fig. 4.12 shows the calculated pressure dependence of Auger current for the three system where we have assumed in all cases that the phonon energy is small. Firstly, our calculations show that the decrease in phonon-assisted Auger rate is much weaker than that of the direct processes. Therefore, these results show that the influence of the band structure is less important for phonon-assisted processes, because the rate depends directly on the effective masses rather than on exponential terms involving the effective masses. Secondly, as can be seen from Fig. 4.9 - Fig. 4.12, the non-radiative Auger current of the three competing laser systems have similar pressure dependences with a most significant difference; the rate of decrease of phonon-assisted processes in N-based laser is slower than that of the other two. The rate of reduction of Auger coefficient C with pressure is very similar for different processes in each of the laser system. Therefore, the relative change of n_{th} with pressure determines the differences in Auger current. The increase of n_{th} with pressure is the reason for the slower decrease of Auger current with pressure in N-based lasers.

Extensive research has been carried out on Auger recombination processes in Al-based lasers and it has been found that [47, 88, 89] the Auger current density do not dominate the total current density in AlGaInAs showing that the situation is improved in Al-based lasers compared to P-based lasers. For
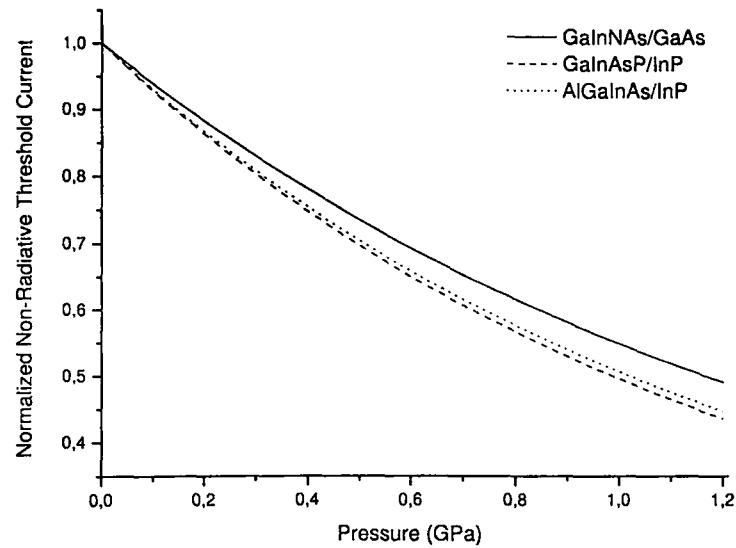
Figure 4.9: The calculated pressure dependence of non-radiative threshold current of three laser systems for phonon-assisted CHCC Auger processes.
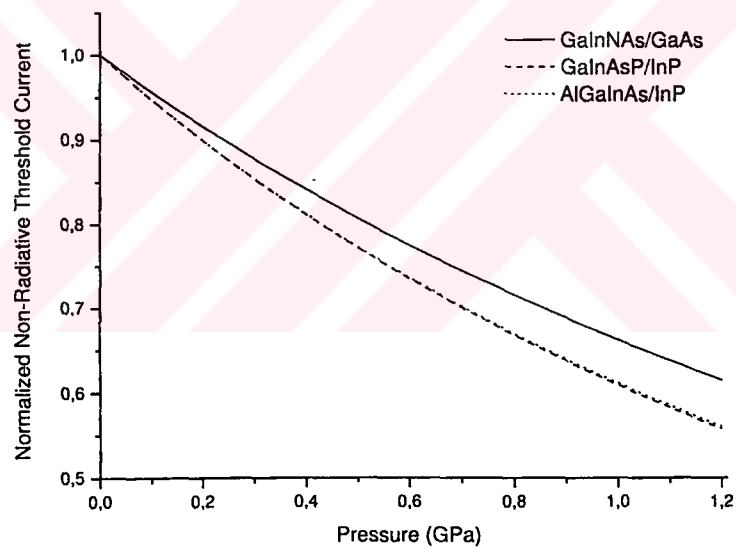
Figure 4.10: The calculated pressure dependence of non-radiative threshold current of three laser systems for phonon-assisted CHSH Auger processes.

GaInNAs material, there is no available published data on the Auger coefficients although, recently, work by Fehse et al. [90] has suggested that direct band-to-band Auger recombination is not the dominant recombination process.

As can be seen from Fig. 4.9 - Fig. 4.12 both direct CHCC and CHSH
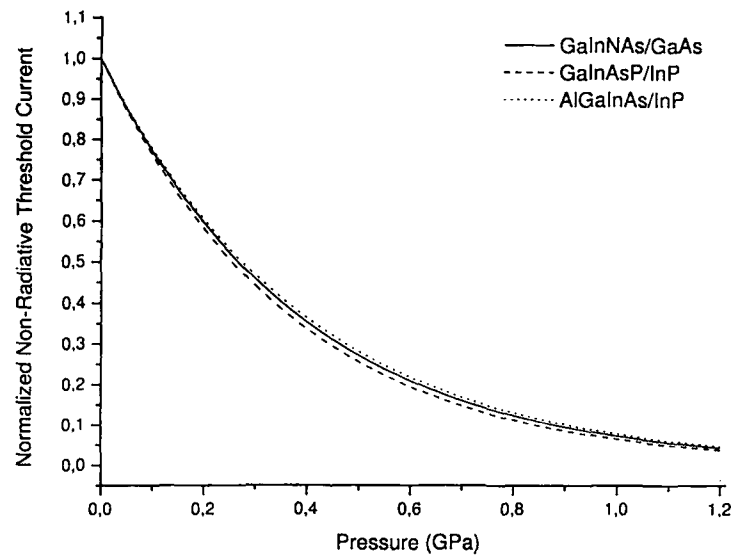
Figure 4.11: The calculated pressure dependence of non-radiative threshold current of three laser systems for direct CHCC Auger processes.
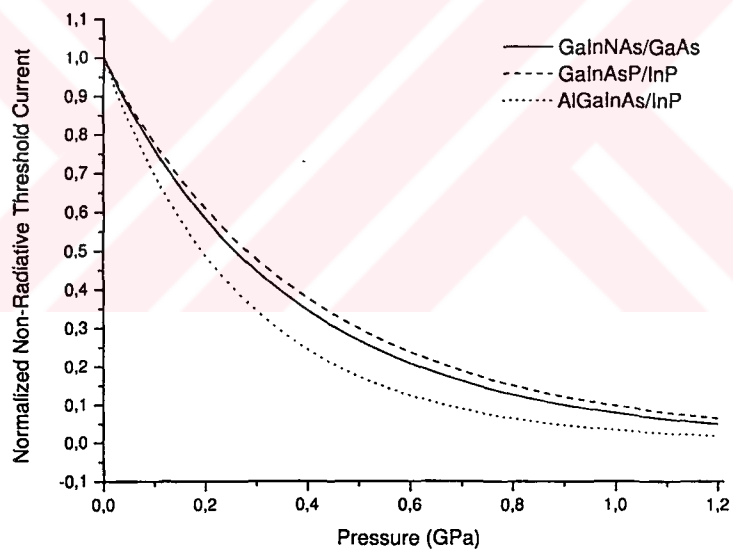
Figure 4.12: The calculated pressure dependence of non-radiative threshold current of three laser systems for direct CHSH Auger·processes.

Auger currents decreases at a much quicker rate than that of the phonon-assisted CHCC and CHSH Auger currents. Therefore, our results suggest the conclusion of the Fehse et al. that the band-to-band Auger recombination is not the dom-

inant recombination process in N-based lasers. The measured change in normalized threshold current with pressure for the three competing laser devices by S.J. Sweeney et al. [91] has shown that threshold current of P-based lasers decreases with pressure whereas the threshold current of the other two increases with pressure with rapid increments has been observed for N-based lasers. They has been attribute this strong increase with pressure to the increase in n_{th} with increasing pressure as a result of the heavier conduction band effective mass. We have calculated a rate of increase of about 2.5 % in n_{th} within a pressure range of 1.2 GPa. Although, this increase is not too much, we expect that it is high enough to change the overall behavior of the threshold current. The quicker rate of increase of radiative current of N-based laser implies that radiative current can dominate the total threshold current density. As an overall, the situation in threshold current of Al- and N-based lasers is improved compared to the P-based lasers. These predictions can be supported by comparing the ratio of the radiative to non-radiative recombination currents for different Auger mechanisms of the three of the laser systems, see Fig. 4.13 - Fig. 4.16. We find that the ratio of the radiative to non-radiative recombination currents for phonon-assisted processes are increased significantly for N- and Al-based devices compared to that of the P-based devices. These results indicate clearly that the non-radiative recombination current is significantly smaller in N-based laser and relatively smaller in Al-based laser devices at room temperature.

4.8   Conclusions

In conclusion, model calculations have been presented to compare the effects of hydrostatic pressure on the threshold carrier and current density for a typical three competing laser devices emitting in the neighborhood of 1.3 μm. We have shown that although optical confinement factor Γ of N-based system is smaller, it has a larger pressure dependence than that of the P- and Al-based lasers. Using simple expressions for idealized quantum well structures, we have
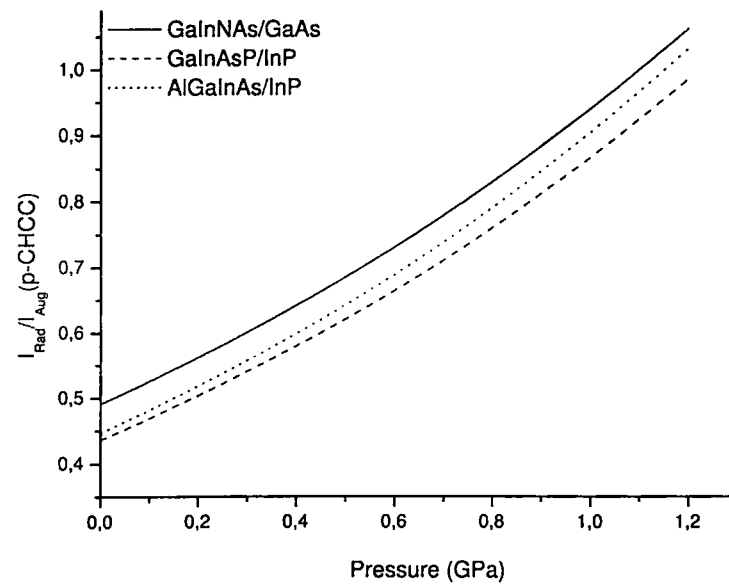
Figure 4.13: The ratio of the radiative to non-radiative recombination currents of three competing laser systems for phonon-assisted CHCC Auger processes.
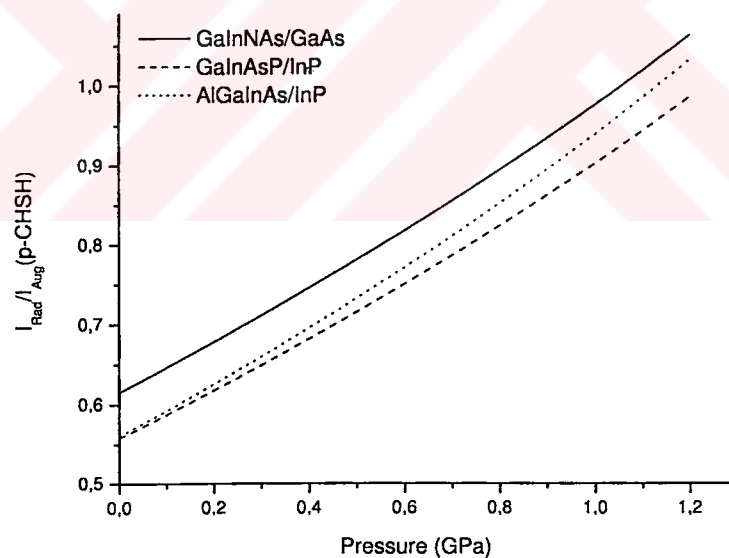
Figure 4.14: The ratio of the radiative to non-radiative recombination currents of three competing laser systems for phonon-assisted CHSH Auger processes.

shown that, although the transparency carrier density n_{tr} increases with pressure in all cases, the threshold carrier density n_{th} decreases owing to the increased optical confinement factor Γ in P- and Al-based lasers. On the other hand, the
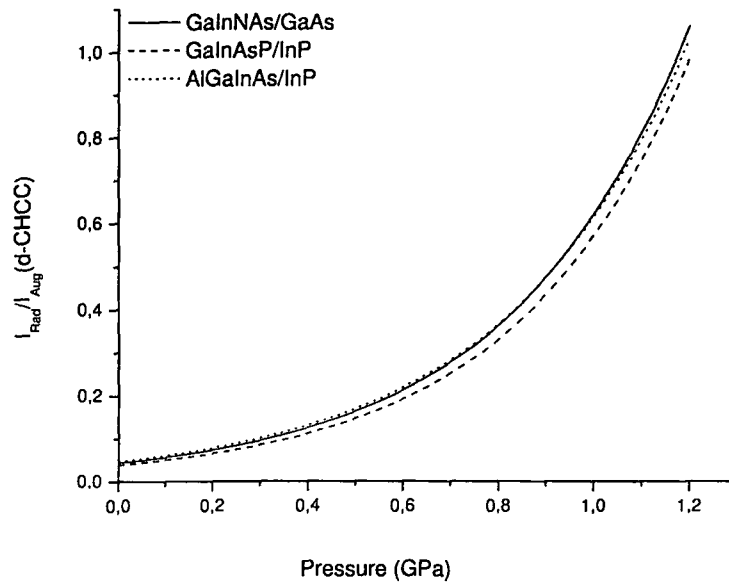
Figure 4.15: The ratio of the radiative to non-radiative recombination currents of three competing laser systems for direct CHCC Auger processes.
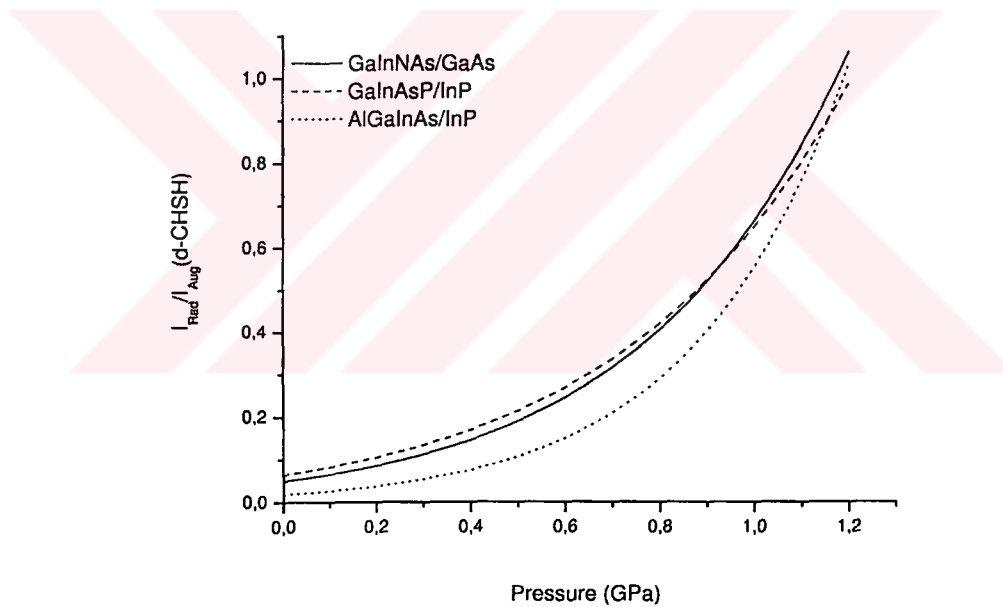
Figure 4.16: The ratio of the radiative to non-radiative recombination currents of three competing laser systems for direct CHSH Auger processes.

threshold carrier density n_{th} of N-based lasers increases slightly causing faster increments in radiative current. The variation of pressure dependence of laser parameters indicates that Al- and N-based laser systems are superior to that of

the P-based laser system and offers the Al- and N-based laser systems as ideal candidates for low threshold and high speed applications, respectively.

The estimated phonon-assisted Auger currents in N-based lasers has a much weaker pressure dependence than that was observed for Al- and P-based lasers. We also find that the ratio of the radiative to non-radiative recombination currents for phonon-assisted processes is increased in both of the N- and Al-based laser systems compared to that of the P-based laser system. Greater increments have been obtained for N-based system. Therefore, these results clearly indicate that the non-radiative recombination current is significantly smaller in N-based and relatively smaller in Al-based lasers at room temperature. This is another indication of the intrinsic superiority of N-based laser system.

Chapter 5

Performance improvement of 1.3 μm GaInNAs/GaAs quantum well lasers by doping

5.1   Introduction

It is known that the optical material quality deteriorates significantly with increasing N mole fractions [92], resulting in a much higher threshold current density of 1.3 μm emitting $Ga_{1-x}In_xN_yAs_{1-y}$/GaAs lasers compared with that of $In_xGa_{1-x}As$/GaAs lasers. In order to improve the performance of 1.3 μm emitting $Ga_{1-x}In_xN_yAs_{1-y}$/GaAs quantum well lasers, the nitrogen concentration of $Ga_{1-x}In_xN_yAs_{1-y}$ well should be reduced, although this leads to an increased strain in the quantum wells. By introducing a strain compensated barrier to this system it is now possible to grow highly strained GaInNAs wells free of misfit dislocations and increase the number of quantum wells in the laser structures [2]. We have shown previously that the performance of equivalent lasers can be increased by means of using strain compensated barriers. In order to achieve 1.3 μm wavelength and maintain high-quality crystal, one effective method is to increase the In composition and decrease the N composition simultaneously. Increasing In composition, i.e. $x > 3y$, results in compressive strain in $Ga_{1-x}In_xN_yAs_{1-y}$ layer. Using this method, 1.3 μm room temperature CW

operation of $Ga_{0.7}In_{0.3}N_{0.01}As_{0.99}$ compressive strained quantum well laser has been successfully fabricated [93].

The reports [7, 94] showed that when small amounts of nitrogen is added to GaAs or InGaAs, the alloy exhibit an unusual band structure than that of III-V alloys. This unusual band structure opens an interesting possibility of using N containing alloys for long wavelength optoelectronic devices [94]. The gain characteristics of nitride alloys emitting 1.3 μm has been studied theoretically and experimentally and compared with more conventional alloy systems [93]-[96]. The potential advantage of doping, however, needs more consideration since there are only limited number of works, [6, 93, 97]. The limitation on the maximum attainable free electron and/or hole concentration by doping is an important issue for the physics of semiconductors and the functionality of their devices. Yu et al [100] reported that the maximum free electron concentration increases rapidly with the N concentration in heavily Se-doped GaInNAs alloys. A dramatic increase of the conduction band electron mass is also reported in heavily n-type doped GaInNAs alloys [6, 93]. These findings offer an interesting opportunity to use alloying with nitrogen not only to overcome doping limits but also provide a closer match between the valence- and conduction-band effective masses in n-type III-V systems. In addition, an understanding of the effect of doping on band structure parameters is an important issue which has to be addressed and will certainly help to clear out the optimization of III-N-V quantum well active layer for improved device performance. In this respect, we have determined the effect of doping on Fermi functions, effective mass, transparency carrier density, peak and differential gain by the unusual band structure behaviour of nitride systems and shown that doped GaInNAs quantum well active layers may have certain benefits to lasers [97]. In addition, a significant reduction in the transparency carrier density by p-type doping and an increase in gain by n-type doping are observed for GaInNAs/GaAs contrary to nitrogen-free InGaAs/GaAs. Overall, our theoretical investigation revealed the fact that n-and p-type doping have also an

unusual, i.e. reverse effect on the band parameters of nitride systems compared to that of the nitrogen-free systems.

The theoretical potential advantage of doped $Ga_{1-x}In_xN_yAs_{1-y}$ / GaAs quantum wells for 1.3 μm laser emission is studied. By means of considering different x/y concentrations, we present the influence of doping on transparency carrier density, gain properties and spontaneous emission factor of 1.3 μm emitting $Ga_{1-x}In_xN_yAs_{1-y}$/GaAs strained quantum wells and compare with an equivalent N-free system 1.3 μm $In_xGa_{1-x}As$/GaAs laser structure. This study provides useful information for the optimization of doped $Ga_{1-x}In_xN_yAs_{1-y}$/GaAs on the basis of 1.3 μm emission wavelength. In this chapter we examine how the doping concentration modifies the N-induced changes in fermi functions, band structure, gain characteristics and spontaneous emission factor by modelling five $Ga_{1-x}In_xN_yAs_{1-y}$/GaAs quantum well laser structures in terms of simplified models for different x/y ratios and determine the optimal laser configuration of compressively strained $Ga_{1-x}In_xN_yAs_{1-y}$ quantum well lasers emitting at 1.3 μm is studied. An equivalent nitrogen-free system is also provided for comparison. The nitrogen concentrations that we have chosen span the range of experimentally demonstrated values [50, 98].

In order to predict the potential advantage of doping on gain characteristics of 1.3 μm $Ga_{1-x}In_xN_yAs_{1-y}$ laser material system for different In/N ratios and provide a clear comparison of the structure parameters, we use BAC model and idealized band model. A compressively strained $Ga_{1-x}In_xN_yAs_{1-y}$ quantum well $(x > 3y)$ yields a 'type-I' band alignment, favorable for lasing action. The band alignment for the nitrogen free system is derived from the Harrison model [99] and the nitrogen including system from the model solid theory [41]. The used parameters for the quaternary compounds are obtained by interpolation method [30].

The band anti-crossing model has been successfully used to quantitatively describe the dependencies of the upper and lower subband energies on N con-

centration and on hydrostatic pressure of group III-N-V alloys [98]-[103]. E_- transitions shifts towards lower energies with increasing N concentration, on the contrary, E_+ transition shifts towards higher energies with increasing nitrogen concentration, and its intensity increases relative to the E_- intensity [8, 12, 26]. As has been stated previously, the electron effective mass in $Ga_{1-x}In_xN_yAs_{1-y}$ has been predicted [104]-[107] to increase with increasing nitrogen concentration in the low concentration range. This behaviour is rather unusual and in fact is opposite to the conventional semiconductors, where the value of the effective mass decreases with decrease of the bandgap energy. Moreover, the conduction band in the alloys is predicted to be very non-parabolic [106], leading to a strong energy dependence of the effective mass. The knowledge of the effect of the effective mass on gain parameters is of special significance for a full exploration and optimisation of this material system in device applications. Therefore, it is our aim at this point to discuss the influence that this has on design issues. Our calculated results show an increased value of the electron effective mass in 1.3 μm $Ga_{1-x}In_xN_yAs_{1-y}$ with increasing nitrogen concentration, as has been predicted by theories. Such an increase may bring a beneficial for device designing due to its effect on subband carrier populations.

5.2 Idealised band model

Idealised band model is based on the assumption that the lasing characteristics are dominated by a single conduction band of mass m_c and a single valence band of mass m_v. This idealised band structure should provide a reasonable description of thin wells under biaxial compression, where $m_v/m_c \approx 2$ [108, 109] and the large energy separation between the valence subbands means that only the first subband is sufficiently populated to play a role. It should also describe thicker wells under large biaxial tension, where $m_v/m_c \geq 10$, and the very large effective mass of the top subband means that the lower subbands are not significantly populated, despite the fact that the energy separation between

the highest and second subband is typically less that 50 meV for 1.5 % tensile strain [52, 53]. The model is less appropriate to lattice matched quantum well structures, and to quantum wells with moderate tensile strain where the valence band structure is strongly nonparabolic and where the second subband can play an important role. The use of realistic band structure yields higher values of the transparency carrier density than those found with parabolic approximation, because of the differing shape of the real bands. Although this simple parabolic band model ignores many features in the real band structure, it should nevertheless be useful for obtaining a theoretical trend, which is in good agreement with the measurements [108]-[110]. The band edge peak gain, G_{max}, for electron and hole carrier density n at the quantum well band edge is given in Eqn. (3.7)-Eqn. (3.13).

The spontaneous noise at the peak gain is given by [46]

$$S = G_0 f_c(n)[1 - f_v(n)].$$
(5.1)

This can be written in terms of carrier density as

$$S = G_0(1 - e^{-n/n_c})(1 - e^{-n/n_v}).$$
(5.2)

The amplifier noise enhancement factor or spontaneous emission factor in semiconductor lasers is

$$n_{sp} = \frac{S}{G_{max}} = 1 + \frac{e^{-n/n_c} e^{-n/n_v}}{1 - e^{-n/n_c} - e^{-n/n_v}}.$$
(5.3)

It is not our intention in this paper to draw any quantitative conclusions relative to experimental values. Therefore, the use of these models provides us the required simple phenomenological expressions for the band structure as needed for laser modelling. Both models that we have used are simple, provide analytical expressions and explain the basic physical properties of materials well.

5.3   Theoretical results and discussions

In order to obtain the optimal laser performance, the transparency carrier density must have its minimum possible value and the differential gain and transition matrix element must have its maximum possible value. The primary use of GaInNAs as an active layer in laser configurations is to obtain the suitable values of transparency carrier density, differential and and transition matrix element. In this work we would like to provide some insight into basic design rules. When considering the necessary indium and nitrogen concentrations to achieve 1.3 μm, it is known that the laser related parameters modify with In and N concentrations [101]. When GaInNAs is intended to use as an active layer in a laser configuration, in general, it is accepted that the route of the highest possible indium and lowest possible nitrogen should be followed [101]. In this way the effect of the nitrogen is used only in the contribution to the reduction of the bandgap and nitrogen-induced nonparabolicity is suppressed. Consequently, the transparency carrier density is minimised and the differential gain is maximised. We should also bear in mind that GaInNAs/GaAs laser systems have substantially better band alignment than the commonly used nitrogen free system. A significant increase in conduction band offset ratio and a decrease in valence band offset ratio have been calculated with the introduction of nitrogen to InGaAs, as shown in Table 5.1. This result highlights the intrinsic superiority of the N-based laser system and offers the GaInNAs/GaAs laser system as an ideal candidate for high temperature operation. As can be seen from Table 5.1 ΔE_C gets bigger with increasing nitrogen and decreasing indium concentration. On the other hand, ΔE_V gets bigger with increasing indium and decreasing nitrogen concentration. Thus, hole leakage increases and electron leakage decreases with increasing nitrogen concentration showing an opposite tendency. It is known that in order to suppress the carrier leakage the conduction/valence band edge of the well must be kept away from that of the barrier. Therefore, the x/y concentration must be well controlled to optimize the carrier leakages while designing

(In/N)	Q_c	ΔE_C (eV)	ΔE_V (eV)
(0.46/0)	0.527	0.299	0.268
(0.50/0.011)	0.519	0.303	0.281
(0.40/0.017)	0.620	0.355	0.218
(0.33/0.021)	0.696	0.397	0.173
(0.30/0.022)	0.725	0.408	0.155
(0.20/0.026)	0.833	0.460	0.093

Table 5.1: Calculated band alignments of 1.3 μm $Ga_{1-x}In_xN_yAs_{1-y}/GaAs$ laser system for different In/N ratios.

1.3 μm $Ga_{1-x}In_xN_yAs_{1-y}/GaAs$ laser system. The investigation of Table 5.1 illustrates the fact of the route of the highest possible indium and lowest possible nitrogen should also be followed in order to obtain the favorable band alignment.

The effect of the x/y concentration on effective masses of 1.3 μm emitting $Ga_{1-x}In_xN_yAs_{1-y}/GaAs$ laser system is summarized in Table 5.2. The increase of the nitrogen concentration on the band structure of the alloy is translated to an increase of the electron effective mass in an explicit way and therefore the uncommonly large electron effective mass improves the matching between the density of states of the conduction band and valence band, i.e. the m_c/m_v ratio gets better in the N-including system. This result confirms the fact that the strong conduction band/valence band asymmetry has been removed in nitrides compared to N-free conventional material system. However, it should be noted that the matching between the effective masses enlarges for high In/low N concentration, which will further results an improved differential gain. It has been shown previously [97, 101] that the transparency carrier density n_{tr} increases with increasing nitrogen concentration and the n_{tr} of the nitrogen-including material system is relatively high compared to the nitrogen-free material system, due to high carrier effective masses, which translates into a high density of states. The effect of nitrogen concentration on n_{tr} can become more clear considering the dependence of the quasi-Fermi levels on the carrier concentration. Since the density of states is bigger with increasing N concentration, the electron Fermi level moves slowly with injected carriers. We have shown [97] that although the

(In/N)	$m_c(m_0)$	$m_v(m_0)$	m_c/m_v
(0.46/0)	0.048	0.054	0.888
(0.50/0.011)	0.055	0.053	1.037
(0.40/0.017)	0.068	0.060	1.133
(0.33/0.021)	0.077	0.066	1.166
(0.30/0.022)	0.081	0.068	1.191
(0.20/0.026)	0.096	0.079	1.215

Table 5.2: Calculated effective masses and their ratios for different In/N ratios in 1.3 μm $Ga_{1-x}In_xN_yAs_{1-y}$/GaAs laser system.

transparency carrier density n_{tr} of nitrogen-included system is higher than that of the nitrogen-free system. n_{tr} values can be reduced effectively by means of n- and p-type doping.
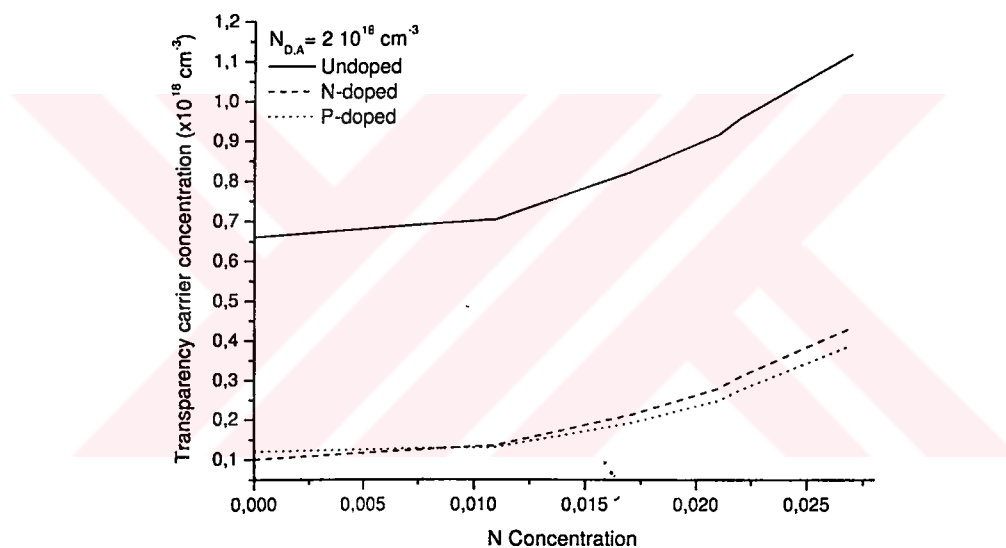
Figure 5.1: The plot of transparency carrier density (n_{tr}) as a function of N concentration for 1.3 μm doped and undoped $Ga_{1-x}In_xN_yAs_{1-y}$/GaAs laser system.

Fig. 5.1 shows the increase of n_{tr} with increasing N concentration for compressively strained 1.3 μm $Ga_{1-x}In_xN_yAs_{1-y}$/GaAs quantum wells emitting at 1.3 μm. Although the strong conduction band/valence band asymmetry has been removed in nitrides compared to N-free conventional material systems as shown in Table 5.2, this will not induce a decrease in the transparency carrier density. The conduction band/valence band symmetry cause the Fermi levels

to move more symmetrically with injected carrier concentration however the density of states in the conduction band is increased due to the increase in conduction band effective mass. As an overall, the conduction band/valence band symmetry do not imply reduced transparency. Because the overall effect is not only determined by reduced conduction band/valence band asymmetry but also the reduced density of states in both valence band and conduction band.

Fig. 5.1 indicates clearly that although the n_{tr} increases with the addition of N into InGaAs, this disadvantage can be eliminated effectively by means of n- and p-type doping. In Eqn. (3.7) and all that follow, the presence of donors or acceptors can be accounted for making the following replacements [46] of:

$$donors: \quad \frac{n}{n_c} \rightarrow (\frac{n + N_D}{n_c})$$
$$acceptors: \quad \frac{n}{n_v} \rightarrow (\frac{n + N_A}{n_v})$$

We kept both n- and p-type doping density at $2x10^{18}cm^{-3}$. Our calculations show that the n_{tr} of the doped $Ga_{1-x}In_xN_yAs_{1-y}/GaAs$ lasers with an emission wavelength in the area of 1.3 μm can have much lower values than that of the undoped N-free corresponding system. The analysis of Fig. 5.1 confirms the facts that we have stated before for the same material system with fixed indium and varying nitrogen concentration; n-type doping is more effective to reduce the transparency level in the nitrogen free system, whereas p-type doping is more effective to reduce the transparency in the nitride system. This shows that doping has a reverse effect on nitride systems compared to an equivalent nitrogen free system. Therefore, the nitrogen induced modifications of the conduction band structure results the $Ga_{1-x}In_xN_yAs_{1-y}/GaAs$ laser system having an unusual property of doping. Our calculations presents that a combination of the effect of the route of the highest possible indium and lowest possible nitrogen and both n- and p-type doping should allow us to have much smaller n_{tr} values for the 1.3 μm $Ga_{1-x}In_xN_yAs_{1-y}/GaAs$ laser system than that of the corresponding nitrogen free system. Fig. 5.2 shows how the peak gain of 1.3 μm

$Ga_{1-x}In_xN_yAs_{1-y}$/GaAs laser reduces with increasing N concentration. The increase in the conduction band effective mass leads to an increase in the carrier concentration at transparency for GaInNAs structure and a decrease in the quasi-Fermi energy separation $E_{fc} - E_{fv}$ for a fixed carrier concentration. As a consequence the peak gain decreases at a fixed carrier density when compared to an equivalent N-free corresponding. On the other hand, the peak gain values for the route of the highest possible indium and lowest possible nitrogen of 1.3 μm $Ga_{1-x}In_xN_yAs_{1-y}$/GaAs is close to the peak gain values of the corresponding nitrogen free system indicating the effect of the proper choice of the x/y concentration. This variation is obtained when the laser material systems are undoped. In order to see the effect of doping on peak gain we obtain a variation of peak gain as a function of nitrogen concentration for a donor and acceptor doping density of $2x10^{18}cm^{-3}$.
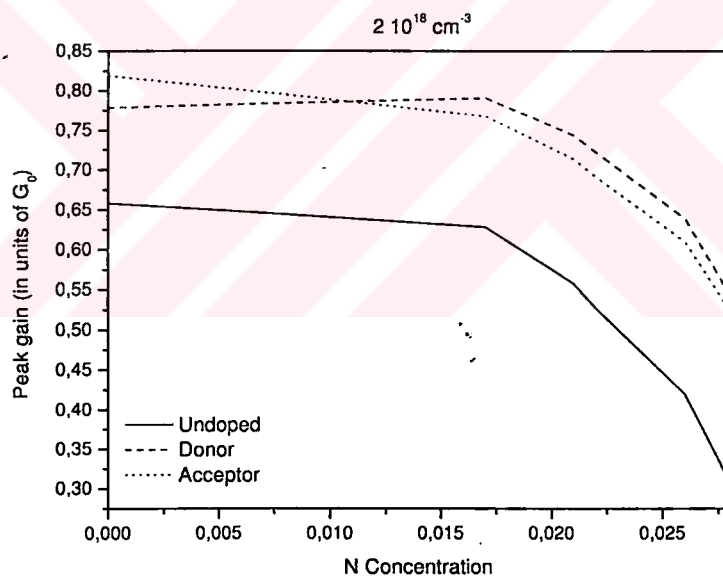
Figure 5.2: The variation of peak gain as a function of nitrogen concentration for 1.3 μm undoped and doped $Ga_{1-x}In_xN_yAs_{1-y}$/GaAs laser system.

As can be seen from Fig. 5.2, a very rapid increase in peak gain is obtained in the case of both n- and p-type doping compared to undoped material system. It should be noted that the magnitude of peak gain is more influenced

by p-type doping in a nitride free system whereas n-type doping seems effective in 1.3 μm $Ga_{1-x}In_xN_yAs_{1-y}/GaAs$ laser systems. The variation of differential gain for undoped and n- and p-type doped 1.3 μm $Ga_{1-x}In_xN_yAs_{1-y}/GaAs$ as a function of nitrogen concentrations is calculated by using Eqn. (3.13) and shown in Fig. 5.3. First, the peak differential gain is reduced with increasing nitrogen concentration. The nitrogen dependence of the differential gain depends on the variation of bandgap, the mass ratio and momentum matrix element. This can be analysed as follows; bandgap decreases with increasing nitrogen concentration causing a decrease in differential gain. Mass ratio increases with nitrogen concentration causing a decrease in differential gain due to the ratio $\left(\frac{dG_{max}}{dn}\right)$ and an increase in differential gain due to the second term in square brackets in Eqn. (3.13) (tends to decrease this term owing to the increase in transparency carrier density with nitrogen concentration; on the other hand, increases with nitrogen concentration). Momentum matrix element decreases with increasing nitrogen concentration which will in turn decreases the differential gain. The combined effect of all these gives a decrease in differential gain with increasing nitrogen concentration. Second, the differential gain of the 1.3 μm N-free laser system is in fact reduced by n- and p-type doping of the quantum well. On the other hand, the differential gain of the 1.3 μm $Ga_{1-x}In_xN_yAs_{1-y}/GaAs$ laser system increased by both n- and p-type doping of the quantum well. It should be notice that both n- and p-type doping tend to have the same values with increasing nitrogen concentration. The reduction in peak differential gain is a result of the increased density of states due to the higher electron effective mass in nitride systems. The higher density of states cause the quasi Fermi level to move more slowly with injected carrier concentration, therefore, resulting a decreased peak differential gain. It is instructive to calculate the spontaneous emission factor, n_{sp}, for different In/N concentrations and this variation is shown in Fig. 5.4. The spontaneous emission factor, n_{sp}, increases with increasing N concentration. The rate of increase is slow for the low N concentration and then it increases

very rapidly with N. Both G_{max} and S decreases with increasing N concentration, however the rate of decrease of G_{max} is faster than that of S resulting an increase in n_{sp} with increasing N concentration. Fortunately n_{sp} can also be decreased by means of doping as shown in Fig. 5.4. p-type doping seems to appear more effective at higher nitrogen concentration. In fact, this can be seen more clearly from the variation of n_{sp} with injection carrier density. Therefore, the magnitude of n_{sp} is more influenced by p-type doping which is the reverse of what was calculated for N-free system in which n-type doping is more effective to reduce n_{sp}.
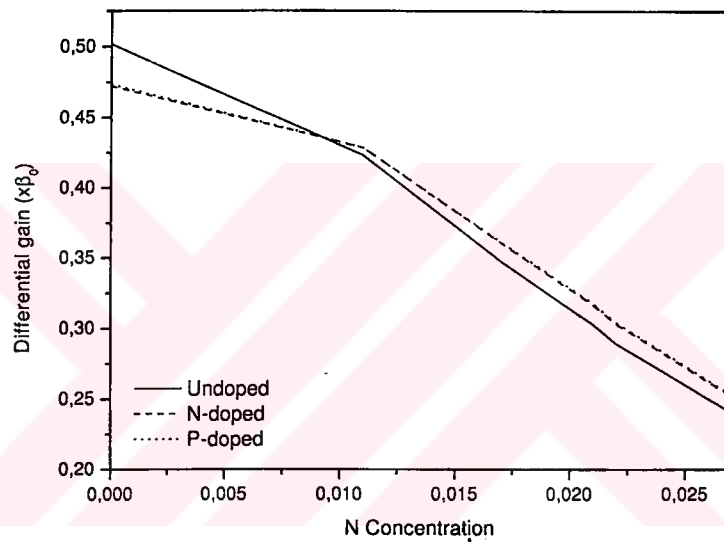
Figure 5.3: The differential peak gain of undoped and n- and p-type doped $Ga_{1-x}In_xN_yAs_{1-y}$/GaAs laser system as a function of nitrogen concentration.

5.4 Conclusions

Ideally, one requires the lowest possible transparency carrier concentration and the maximum possible differential gain in a laser structure. By means of this both the transparency and threshold carrier concentrations to reach the positive material gain and maximum gain are minimised, respectively. Additionally, a high differential gain enhances the modulation bandwidth of laser structures.
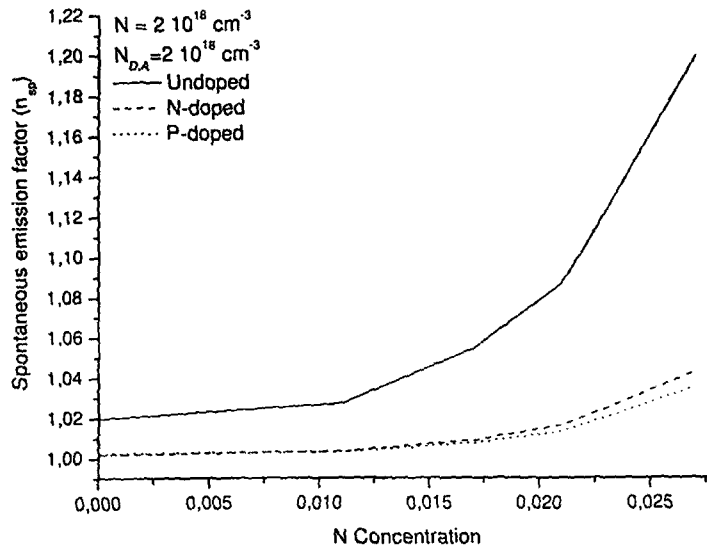
Figure 5.4: The calculated variation of the spontaneous emission factor versus N concentration for undoped and n- type and p-type doped $Ga_{1-x}In_xN_yAs_{1-y}$ / GaAs laser system.

The transition matrix element quantifies the overlap between the electron wavefunction and the hole wavefunction. Hence maximum possible values are desired since the wavefunction overlap is then more efficient leading to higher values of gain. The transparency carrier concentration, the peak gain and differential gain and the transition matrix element are magnitudes that depend on the band structure of the active material, which in turn is modified for different indium and nitrogen compositions. In order to conclude the optimal route of 1.3 μm $Ga_{1-x}In_xN_yAs_{1-y}$/GaAs laser system, we present a theoretical variation of gain characteristics as a function of different In/N concentrations, which result an emission wavelength of 1.3 μm, and especially focus on the effect of doping on these properties. We conclude that the optimal route of 1.3 μm wavelength GaInNAs would be the choice of the higher indium instead of the higher nitrogen due to the better matching of the effective masses, favorable band alignment, smaller transparency carrier density, higher peak and differential gain and lower spontaneous emission factor. Our results reveal that doping has a reverse effect on gain characteristics of $Ga_{1-x}In_xN_yAs_{1-y}$/GaAs laser system compared to the N-free

corresponding laser system. This is another unusual physical property of nitrogen containing alloys due to the nitrogen-induced modifications of the conduction band structure. In addition, we have shown that the modulation doping have certain benefits in $Ga_{1-x}In_xN_yAs_{1-y}/GaAs$ laser system. As an overall, significant improvements in the performance of the novel material system of 1.3 μm $Ga_{1-x}In_xN_yAs_{1-y}$/GaAs laser system have been calculated by doping keeping the route of the high indium and low nitrogen concentration.

Chapter 6

Bandgap renormalization in semiconductor quantum well lasers

6.1 Introduction

The material gain calculations for bulk and quantum well lasers have often based on the free carrier model, where Coulomb interaction between the injected electrons and holes in the active region is ignored. This model was first formulated about thirty years ago [111]- [114]. Although some of the many-body effects in semiconductors became known in 1970's [115], a systematic theory for semiconductor-light interactions including Coulomb interactions was only available much later [116]- [119]. The role of Coulomb interaction between electrons and holes confined into an active region of laser diode can be explained within a simple physical picture; while Coulomb force attracts electrons and holes at a closer distance, electron-hole radiative recombination rate increases, which manifests an enhancement in the intensity of spontaneous emission as well as in gain magnitude. In order to obtain more comprehensive model for the gain in the presence of large numbers of oppositely charged carriers the many body theory needs to be invoked. Some potentially significant many-body effects are band-gap narrowing, interband Coulomb attraction, plasma screening, and carrier-carrier scattering [119].

Because of the technical application of optoelectronic devices such as laser diodes, bandgap renormalization as one of the important factors of the optical nonlinear mechanism in the semiconductor quantum well systems has great deal of attention. The free carriers gives rise to bandgap renormalization which explains the experimental fact of the low-energy-side broadening of the spontaneous emission in the quantum well laser [120]-[122]. Work on bandgap renormalization due to many body effects has been extensively carried out, taking into account the screening on the Coulomb interaction between all charged particles as well as the exchange interactions.

In order to obtain a quantitative understanding of the renormalizations and of their subband dependence in quantum well systems, fully dynamic random-phase approximation self energy calculations will hence be considered. The calculations will be carried out for realistic systems with finite well widths, finite barrier heights, and finite temperatures. The optical gain and threshold current density will be calculated using the density matrix theory with intraband relaxation.

In this chapter, we first provide the theoretical background of the bandgap renormalization and present the material gain calculations for conventional lasers.

6.2   Theoretical Model

Enhancement of the optical gain due to the attractive electron-hole interaction is considered to be important in the description of the optical properties of semiconductors [124]. Coulomb interaction modifies spontaneous emission and gain spectra of laser diodes by shifting the gain peak towards lower energies. One of the inherent characteristics of electron-hole plasma is screening of the Coulomb potential. The modified, screened Coulomb potential $V_{sq}(q, \omega)$, as described in the momentum and frequency domain relates to an unscreened Coulomb poten-

tial, V_q, as:

$$V_{sq}(q,\omega) = \frac{V_q}{\varepsilon(q,\omega)} \tag{6.1}$$

where $\epsilon(q,\omega)$ is the longitudinal dielectric function that includes spatial dispersion (q dependence) and spectral dispersion (ω dependence). If one neglects the dynamic aspect of screening contained in a frequency dependence of the dielectric function, $\varepsilon(q,\omega)$, one can obtain the following dielectric function using the plasmon-pole approximation [125]:

$$\frac{1}{\varepsilon(q,w)} = 1 - \frac{\omega_{pl}^2}{\omega_q^2}, \tag{6.2}$$

where ω_{pl} is the plasma frequency, while ω_q is an effective plasmon mode frequency. The Coulomb interaction Hamiltonian contains the Fourier transform of the screened Coulomb potential is

$$V_{sq} = V_q(1 - \frac{\omega_{pl}^2}{\omega_q^2}). \tag{6.3}$$

Quantum well widths for lasers are less than 150 Å, which is sufficiently narrow to approximate the carriers as a two-dimensional plasma. In particular, in case of electrons and holes confined in a quantum well, one should use a two-dimensional (2D) Coulomb interaction, given by:

$$V_q = \frac{2\pi e^2}{\epsilon_b q A}. \tag{6.4}$$

where A is the quantum well area, ϵ_b is the background dielectric constant in the area of the quantum well and q is taken as $q = k - k'$. The another two parameters are the effective plasmon frequency ω_q^2 given by

$$\omega_q^2 = \omega_{pl}^2(1 + \frac{q}{\kappa}) + \frac{C_r}{4}(\frac{\hbar q^2}{2m_r}), \tag{6.5}$$

and the two dimensional (2D) plasma frequency ω_{pl} is

$$\omega_{pl}^2 = \frac{2\pi e^2 N_{2D} q L_z}{\epsilon_b m_r} = \frac{8\pi N_{2D} L_z a_0^3 \epsilon_R^2 q}{\hbar^2} \tag{6.6}$$

where C_r is a unitless constant typically in a range 1-4, $N_{2D} = N_{3D} L_z$ is the

(2D) carrier density in a quantum well width of L_z, m_r is the reduced effective mass of conduction band electrons and valence band holes in directions parallel to the quantum well plane and a_0 is the radius of the lowest exciton state and known as exciton Bohr radius,

$$a_o = \frac{4\hbar\pi\epsilon_0\epsilon_b}{e^2 m_r}. \tag{6.7}$$

The resonance energies for the optical transitions can be changed by the Coulomb interactions, which for low densities leads to the creation of exciton. Here the Coulomb attraction can bind an excited electron and hole pair into an exciton, which is hydrogen-like "atom" with a finite lifetime. By replacing proton mass by the reduced electron-hole mass, $m_r = \frac{m_e m_c}{m_e + m_c}$, we can use Bohr hydrogen model. The energy of the lowest state is given by the exciton Rydberg energy ϵ_R,

$$
\begin{aligned}
\epsilon_R &= \frac{\hbar^2}{2 m_r a_0^3} \\
&= \frac{e^2}{8\pi\epsilon\epsilon_b a_0} \\
&= \frac{e^4 m_r}{32(\pi\epsilon\epsilon_b)^2 \hbar^2}.
\end{aligned} \tag{6.8}
$$

The description of the semiconductor behavior depends on a_0 compared to the mean distance between electron-hole pairs and the screening length, and ϵ_R compered to $k_B T$.

As shown in Fig. 6.1, the Bohr radius increases linearly for $InGaAs/GaAs$ with increasing In concentration. The inverse screening length (κ) is a measure of effectiveness of the screening of the Coulomb interaction between two carriers by other carriers and defined by

$$\kappa = \frac{e^2}{2\varepsilon\varepsilon_b}\left(\frac{\partial N_{2D,e}}{\partial \mu_{fc}} + \frac{\partial N_{2D,h}}{\partial \mu_{fv}}\right). \tag{6.9}$$

In the two band, quasi equilibrium approximations near band edge yields

$$\kappa = \frac{2}{a_0}\left(\frac{m_e}{m_r}f_{e0} + \frac{m_h}{m_r}f_{h0}\right) \tag{6.10}$$

where $f_{\alpha 0}$ denotes the Fermi-Dirac distribution at $k = 0$. This analytic result can
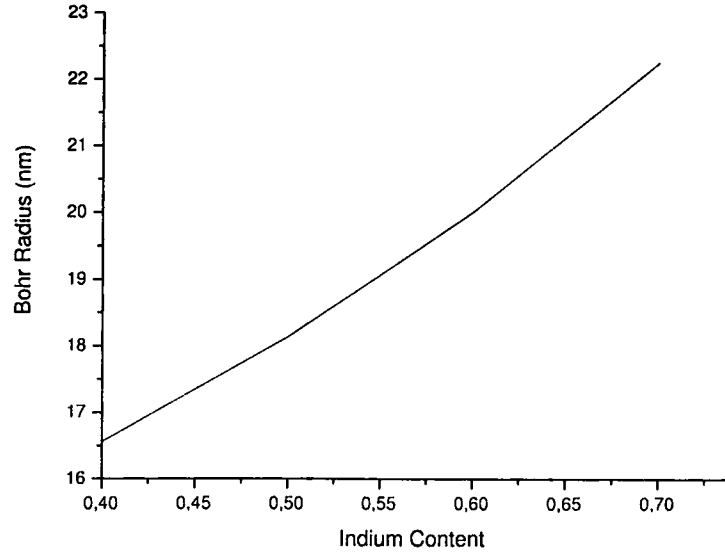
Figure 6.1: Bohr Radius for different In concentration.

be verified easily by using the explicit two dimensional carrier density formula and the Fermi Dirac distribution for $k = 0$.

Using Eqn. (6.3)-(6.5) and Eqn. (6.6), it can be found that the screened Coulomb potential as

$$V_{sq} = \frac{4\pi\epsilon_R a_0}{Aq}(\frac{q}{\kappa}) + (\frac{C_r a_0 q^3}{1 + \frac{q}{\kappa} + \frac{C_r a_0 q^3}{32\pi N_{2D}}})^{-1}, \qquad (6.11)$$

We apply these equations to study the bandgap renormalization effect that is the effect of carrier Coulomb interaction on the spectrum of e-h inter-band recombination. This Coulomb Hole (CH) contribution to the band-gap reduction with inserting the V_{sq} in Eqn. (6.15), that is the hole-energy in terms of an effective mass as

$$\begin{aligned} E_{hk}^s &= -E_{vk} + \sum_{q \neq 0} V_{sq} \\ &= \frac{\hbar^2 k^2}{2m_h}. \end{aligned} \qquad (6.12)$$

and

$$E_{hk}^s = -E_{vk} + \sum_{q \neq 0} V_q + \sum_{q \neq 0} (V_{sq} - V_q)$$

$$= E_{hk} + \sum_{q \neq 0} (V_{sq} - V_q).$$

$$= E_{hk} + \Delta E_{CH}, \qquad (6.13)$$

where the Debye shift, or Coulomb-hole self energy, can be defined as

$$\Delta E_{CH} \cong \sum_{q \neq 0} [V_{sq} - V_q]. \qquad (6.14)$$

This term is independent of wavevector and is usually considered as an additional contribution to the bandgap shift. It is due to the increasing effective plasma screening that occurs with increasing carrier density. At very low carrier densities, the lack of vacant valence band states together with the exclusion principle limit the ability of the valence electron distribution to effectively screen the Coulomb repulsion between a conduction electron and any one of the valence electrons. The corresponding abundance of vacant conduction band states are energetically inaccessible to a valence electron via the Coulomb interaction. At higher carrier densities, more vacant valence band states are available to allow the redistribution of charges for more effective screening. Since the screening of a repulsive interaction leads to a lowering of the conduction electron energy, the transition energy decreases with increasing density. The static plasmon-pole approximation the Coulomb-hole energy is written as

$$\Delta E_{CH} = \sum_{q \neq 0} (V_{sq} - V_q)$$

$$= \sum_{q \neq 0} V_q (\frac{1}{\epsilon_q} - 1)$$

$$= -\sum_{q \neq 0} V_q \omega_{pl}^2 [\omega_{pl}^2 (1 + \frac{q^2}{\kappa^2}) + \frac{C_r}{4} (\frac{\hbar q^2}{2m_r})^2]^{-1}. \qquad (6.15)$$

In addition to the Coulomb-hole self energy, there is a second contribution to the carrier density dependence of ω_k that comes from the Hartree-Fock approximation,

$$\Delta E_{SX,k} = -\sum_{k' \neq k} V_{s,|k-k'|} (n_{ck'} + n_{hk'}), \qquad (6.16)$$

which is screened-exchange (SX) shift. It is often a reasonable approximation to

neglect the weak k-dependence in $\Delta E_{SX,k}$ and just use a k-independent ΔE_{SX}. In this case, both contributions to the ω_k renormalization are independent of k and renormalized bandgap is given by

$$E_g = E_{g0} + \Delta E_{CH} + \Delta E_{SX}. \tag{6.17}$$

Evaluating Eqn. (6.15) and Eqn. (6.16) for the quantum well

$$\Delta E_{CH} = -2\epsilon_R a_0 \int_0^\infty \frac{dq}{1 + \frac{q}{\kappa} + \frac{C a_0 q^3}{32\pi N_{2D}}}$$

$$\simeq -2\epsilon_R a_0 \kappa \ln\left(1 + \sqrt{\frac{32\pi N_{2D}}{C\kappa^3 a_0}}\right). \tag{6.18}$$

and

$$\Delta E_{SX} = -\frac{2\epsilon_R a_0}{\kappa} \int_0^\infty dk\, k \frac{1 + \frac{C_r \kappa a_0 k^2}{32\pi N_{2D}}}{1 + \frac{k}{\kappa} + \frac{C_r a_0 k^3}{32\pi N_{2D}}} (f_{ek} + f_{hk}) \tag{6.19}$$

where f_{ek} and f_{hk} are the Fermi-Dirac distributions.
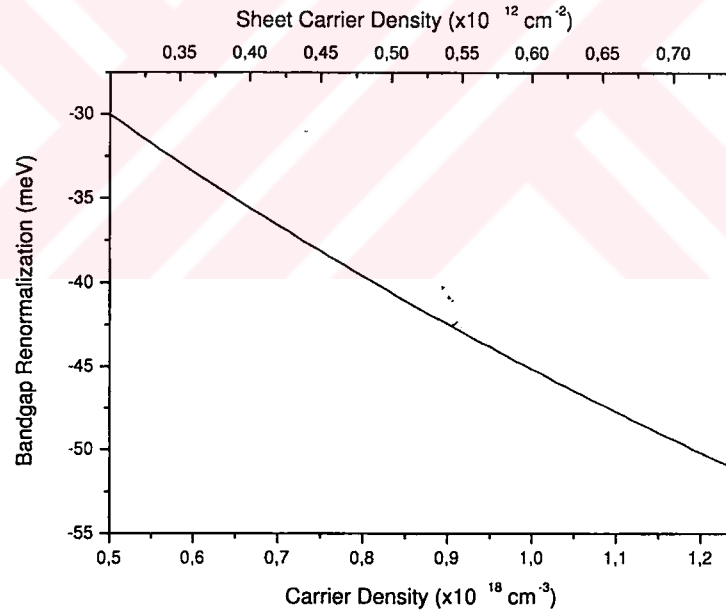
Figure 6.2: The bandgap renormalization as a function of carrier density for $In_x Ga_{1-x} As/GaAs$ quantum well for $x = 0.4$ and $L_z = 60$ Å.

6.3 Results and Conclusions

In this section, our aim is to examine the linear gain including the bandgap renormalization for InGaAs/GaAs quantum wells. We have carried out calculations for a strained 60 $\overset{\circ}{A}$ $In_xGa_{l-x}As$ well at T = 300 K. The material parameters are quoted from Vurgaftman [30] and Chuang [111]. The linear gain, $\alpha(\omega)$, calculations for quantum wells have been carried out the theory developed by Asada [126] who used the density-matrix theory with relaxation broadening. The linear gain $\alpha(\omega)$ is given for parabolic bands by the following equation of

$$\alpha(\omega) = \omega\sqrt{(\mu/\epsilon)}\frac{m_c^*m_v^*}{(m_c^*+m_v^*)}\frac{1}{\pi\hbar^2L_z}\sum_{j,j'}\int_{E_g+E_{cj}+E_{vj'}}^{\infty} < R_{cv}(E_{cv})^2 >$$

$$\times(f_c(E_{cjk_{\|}}) - f_v(E_{vj'k_{\|}}))L(\hbar\omega)dE_{cv}, \tag{6.20}$$

with a Lorentzian broadening function

$$L(\hbar\omega) = \frac{\hbar/\tau_{in}}{(E_{cv} - \hbar\omega)^2 + (\hbar/\tau_{in})^2}, \tag{6.21}$$

where τ_{in} is the intraband relaxation time that characterize the decay time of the dipole formed by the recombining electron and hole, which interacts with the electromagnetic wave. ω is the angular frequency of light, μ is the free space permeability, ϵ is the dielectric constant, L_z is the well width , $m_c^*m_v^*/(m_c^*+m_v^*)$ is the reduced mass and E_{cv} is the transition energy. The transition energy with bandgap renormalization is written as

$$E_{cv} = E_{g0} + E_c + E_v + \Delta E(N). \tag{6.22}$$

where E_{g0} is the bulk bandgap, E_c and E_v are conduction- and valance-subband energies, respectively. The transition energy (E_g) is increased by the electron and heavy-hole quantum confinement energies, which depend directly upon quantum well thickness (L_z), and also upon indium concentration via the effective masses $(m_e^*, m_{hh}^*, m_{lh}^*)$ and conduction-band and valence-band offsets. The last term

$\Delta E(N)$ is the bandgap shrinkage due to the Coulomb-hole self energy, ΔE_{CH}, and screened-exchange (SX) shift, ΔE_{SX}. This term depends on the total carrier density N and decreases the transition energy. We calculate the bandgap renormalization as a function of carrier density for 60 $\mathring{A}In_{0.4}Ga_{0.6}As$ quantum well and Fig 6.2 shows the results illustrate the fact that the bandgap renormalization increases with increasing carrier density.
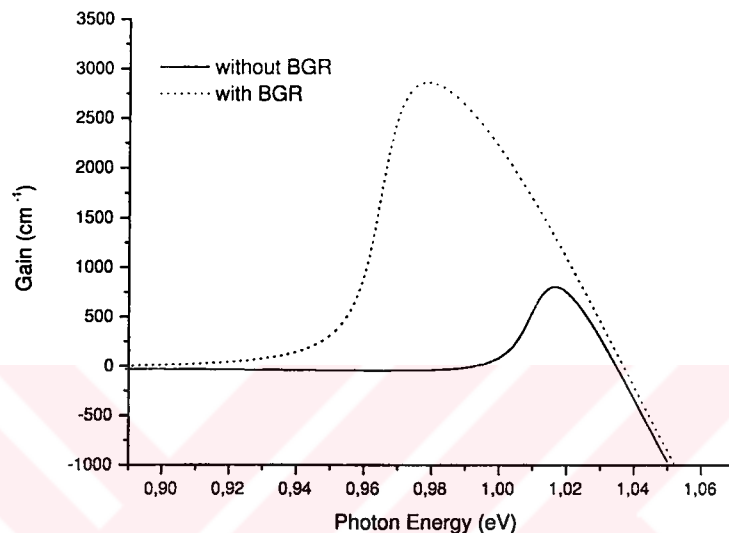
Figure 6.3: The linear gain for the InGaAs/GaAs with and without bandgap renormalization as a photon energy.

The Coulomb interaction between the injected electrons and holes in the active region is considered to be a more comprehensive model for the gain. In order to examine the effect of bandgap renormalization on linear gain, we calculate the linear gain for InGaAs/GaAs lasers with and without bandgap renormalization. This is illustrated as a function of photon energy in Fig. 6.3. As seen from Fig. 6.3, an enhancement in the linear gain is calculated when the bandgap renormalization is included.

The phenomenon of Coulomb enhancement, resulting from the consideration of many body effects, is included in the calculation of the gain of the quantum well lasers.

In order to examine the carrier dependence of peak gain with and without
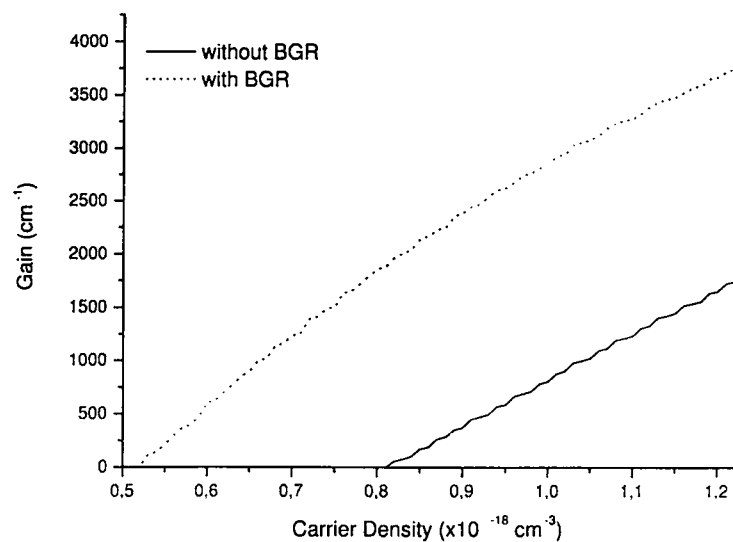
Figure 6.4: The peak gain for the InGaAs/GaAs with and without bandgap renormalization as a function of carrier density.

bandgap renormalization, we obtain Fig. 6.4. Peak gain increases with increasing carrier density. It can be concluded from Fig. 6.4 that one should have taken into account bandgap renormalization for gain calculations since gain is enhanced approximately three orders of magnitude when the bandgap renormalization is included. The order of magnitude of the enhancement depends on the carrier density.

Chapter 7

Band offset dependence of exciton binding energy calculations in 1.3 μm $Ga_{1-x}In_xN_yAs_{1-y}/GaAs$ quantum well lasers

7.1   Introduction

There has been considerable interest in excitons in semiconductors quantum well structures. Excitons have large effects on optical phenomena in these structures, so that an understanding of their properties, such as the increase in binding energy and oscillator strength due to confinement effects, has become an important topic in the physics of multi layer systems. Following the work of Miller et al [127] several authors have calculated binding energies of excitons in both infinite [127]-[145] and finite quantum wells [128, 129]. All these calculations are variational, including or not different phenomena such as valance-band mixing, nonparabolicity of dispersion relations, effective-mass, and/or dielectric constant mismatch between the well and barrier materials, Coulomb coupling between excitons belonging to different subbands, etc. These calculations need important computation times and the accuracy of the result depends to a large extent on the form of the trial wave function. In section 7.2 we review a fully

analytical model to calculate the exciton binding energy. The aim of the method reviewed here is not to compete with the very advanced ones like the very accurate theory proposed by Adreani and Pasquarello [128]. On the contrary, it is avoided tedious calculations to obtain, with reasonable accuracy, the exciton binding energy in most of the type-I confined structures. In its analytic, very simple form the method takes into account the effective-mass and dielectric-constant mismatches and the conduction band nonparabolicity. A satisfactory agreement with both experimental results and calculations of Adreani and Pasquarello [128] is obtained for InGaAs and the method stay free of tedious computer calculations. The gain characteristics of nitride alloys emitting $1.3 - 1.5$ μm has been studied both theoretically and experimentally and compared with more conventional alloy systems [93]- [96]. The investigation of the exciton binding energy, however, needs more consideration since there are only limited number of works [146]. Therefore, an understanding of exciton behavior in III-N-V quantum wells is an important issue which has to be addressed and will certainly help to clear out the optimization of III-N-V quantum well active layer for improved device performance.

The aim of this work is first to provide an understanding of the variation of exciton binding energy in $Ga_{1-x}In_xN_yAs_{1-y}$ laser material system with nitrogen concentration. Secondly, in order to predict the optimal In/N ratio of 1.3 μm $Ga_{1-x}In_xN_yAs_{1-y}$ laser system, we calculate the exciton binding energy by means of modelling five $Ga_{1-x}In_xN_yAs_{1-y}$/GaAs quantum well laser structures for different x/y (In/N) ratios. Finally, we provide a comparison of the ground state heavy-hole exciton binding energies of the conventional P-based and Al-based lasers with that of the novel laser material system of N-based lasers.

The band alignment for the nitrogen free system is derived from the Harrison model [99] and the nitrogen including system from the model solid theory [41]. The used parameters for the quaternary compounds are obtained by the linear interpolation method [30].

7.2   Theoretical Model

Leavitt and Little [147] presented a simple method for calculating exciton binding energies in quantum-confined structures neglecting valance-band mixings. The main result obtained in their paper is an expression for the exciton binding energy as the integral of a prescribed function, using five numerical parameters, weighted by the electron and hole subband envelope functions. In these approach, because details of the structure are included only through the subband envelope functions, the method can be applied to a wide variety of structures in which the exciton can be associated with a specific pair of electron and hole subbands. This approach is further simplified and generalized by means of a fully analytical method, free of any adjustable parameter by Mathiue et al [150]. In order to investigate the band offset dependence of excitons in GaInNAs/GaAs quantum wells, we first review the analytical model of Mathiue et al in this section. The method of Mathiue et al [150] uses the model of fractional-dimensional space already employed to study Wannier-Mott excitons in anisotropic solids [148]. The excitons in an anisotropic solid, like a quantum well, are treated as the ones in an isotropic fractional-dimensional space, where the dimension is determined by the degree of anisotropy. Such a space, termed dynamic space, differs from the one that embeds geometric bodies in that its dimensionality is determined by the physical interactions. Concerning the excitons in quantum-well structure, the question is what the spatial dimension α which measures the anisotropy of the electron-hole interaction. Knowing α, the model enables one to study exciton binding energy continuously from three-dimensional (3D) to 2D or 1D structures. By using this model, He [148] calculated the exciton bound-state energies and wave functions as a function of spatial dimension α by solving a simple hydrogenic Schrödinger equation in an αD space. The discrete bound-state energies and orbital radii are given by

$$E_n = E_g - \frac{E_0}{\left[n + \frac{\alpha-3}{2}\right]^2},$$

(7.1)

$$a_n = a_0 \left(n + \frac{\alpha - 3}{2} \right)^2, \tag{7.2}$$

where n=1,2,3... is the principal quantum number, E_0 and a_0 are, respectively, the effective Rydberg constant and effective Bohr radius,

$$E_0 = \left(\frac{\varepsilon_0}{\varepsilon} \right)^2 \left(\frac{\mu}{m_0} \right) R_H \tag{7.3}$$

and

$$a_0 = \left(\frac{\varepsilon}{\varepsilon_0} \right) \left(\frac{m_0}{\mu} \right) a_H. \tag{7.4}$$

R_H and a_H are the Rydberg constant and Bohr radius, respectively. m_0 is the free electron mass, μ is the exciton in-plane reduced mass. According to Eqn. (7.1), the binding energy of the 1s exciton is given by

$$E_b = E_0 \left[\frac{2}{\alpha - 1} \right]^2, \tag{7.5}$$

$\alpha = 3, 2$, or 1 give, respectively $E_b = E_0$, $4E_0$ or ∞ corresponding to the well-known results of the integer-dimension models. In a real quantum-well structure, α changes continuously between 3 and 2. As the well width decreases, both electron and hole envelope functions become compressed, the Coulomb attraction between the electron and the hole becomes anisotropic and the fractional dimension α decreases from 3 toward 2. For very narrow wells, the envelope functions spread into the barriers, their spatial extents actually begin to increase as the well width decreases. Consequently α does not lead to 2, but has a minimum value corresponding to onset of this spreading. Thus the main problem is to define the fractional dimension α, which describes the degree of anisotropy of the electron-hole interaction. This parameter should be related to a quantity which accounts for the spatial extension of this interaction. A possible choice is to express α is in terms of the average electron-hole distance in the quantum-confinement direction (z direction). In this way, the pertinent dimensionless parameter is written as

$$\beta = \left\langle \frac{|z_e - z_h|}{a_0} \right\rangle = \int_{-\infty}^{\infty} \left(\frac{z_e - z_h}{a_0} \right) f_p^e z_e^2 f_q^h z_h^2 dz_e dz_h \tag{7.6}$$

where $f_p^e z_e^2$ and $f_q^h z_h^2$ is the electron (hole) envelope function corresponding to the

$p^{th}(q^{th})$ electron (hole) quantum level. a_0 is the three dimensional effective Bohr

radius. It should be noted that a_0 has been included under the integral sign since,

in finite quantum wells, it depends on the distributions of the envelope functions

between the well and the barrier materials. Then the fractional dimension α is

related to the reduced average electron-hole distance β by a simple exponential

law like

$$\alpha = 3 - e^{(-\beta)} \tag{7.7}$$

with $\beta \rightarrow \infty$ corresponds to the three dimensional case ($\alpha = 3$), and $\beta = 0$

corresponds to the two dimensional case ($\alpha = 2$).

In finite quantum wells, it is known that as the well width decreases below a

given value, the envelope functions spread into the barriers. Then, the spreadings

of the electron and/or hole inside the barrier material partially restore the three-

dimensional character of the exciton. Consequently the fractional dimension α

does not lead to 2 as the well width becomes very small, but should come back

to 3 and must be expressed as a function of this spreading. Let us briefly recall

the one-dimensional motion of a particle (electron-hole), of effective mass m in

a square quantum-well characterized by a well depth V and a well width L_z. By

taking the bottom of the well as the zero of the energy, the bound state energies

E_P of the particle are given by the well-known trancendental equation which

may be written

$$k_w L_z = p\pi - 2 \arcsin \left[\frac{k_w}{m_w \sqrt{\frac{k_b^2}{m_b^2} + \frac{k_w^2}{m_w^2}}} \right] \tag{7.8}$$

where the characteristic wave vectors k_w and k_b are given by

$$k_w = \frac{\sqrt{2m_w E_p}}{\hbar} \tag{7.9}$$

$$k_b = \frac{\sqrt{2m_b(V - E_p)}}{\hbar} \tag{7.10}$$

m_w and m_b are the effective masses of the particle in the well and barrier ma-

terials, respectively. Inside and outside the quantum well, the z motion of the particle is described by the respective envelope functions of

$$\zeta_w z = A \sin\left(k_w z + \phi\right) \tag{7.11}$$

$$\zeta_b z = B e^{(\pm k_b z)} \tag{7.12}$$

In a finite quantum well, the pertinent parameter is written as $\frac{L_z^*}{2a_0^*}$ where L_z^* and a_0^* have the corresponding meanings in the finite well. L_z^* should be represent the spatial extension of the particle motion in the z direction; then, taking into account the spreading into the barriers on both sides of the well, L_z^* may be written as

$$L_z^* = \frac{1}{k_b} + L_z + \frac{1}{k_b} \tag{7.13}$$

where k_b is given by the solution of Eqn. (7.8). Now concerning the electron-hole pair, the electron and hole spreadings into the barriers are to be combined to define a length characteristics of the z motion of the electron hole pair. Here the question is when the electron and hole spreading very different, which of the two carriers rules the pair motion with regard to the well potential. Before answering that question, it must be noted that, with regard to the only square-well potential, there is no electron-hole interaction to take into account. As a result, when the electron and hole spreading are very different, the more localized particle partially restores a 3D character to the electron hole distance, or equivalently, to the center-of-mass motion. Consequently the spreading of the pair into the barriers may be written as

$$\frac{1}{k_b} = \frac{1}{k_{be}} + \frac{1}{k_{bh}} \tag{7.14}$$

where k_{be} and k_{bh} are given by the solution of Eqn. (7.8), the electron and hole wave vectors in barrier materials. The characteristic length of the motion of the electron-hole pair with regard to the quantum-well effect will be written

$$L_z^* = \frac{2}{k_b} + L_z \tag{7.15}$$

Concerning the length characteristic of the Coulomb interaction, it is noted that the 3D effective Bohr radius a_0 varies with the position-dependent effective masses and dielectric constant. In order to account for the effective-mass mismatch between the well and barrier materials, two weighting parameters β_e and β_h as

$$\beta_e = \frac{L_z}{(\frac{2}{k_{be}})} + L_z, \qquad \beta_h = \frac{L_z}{(\frac{2}{k_{bh}})} + L_z \qquad (7.16)$$

By using these parameters, mean values for the electron effective-mass and valance-band parameters can be defined, as

$$m_e^* = \beta_e m_{ew} + (1 - \beta_e m_{eb}) \qquad (7.17)$$

$$\gamma_1^* = \beta_h \gamma_{1w} + (1 - \beta_h)\gamma_{1b}, \qquad (7.18)$$

$$\gamma_2^* = \beta_h \gamma_{2w} + (1 - \beta_h)\gamma_{2b}. \qquad (7.19)$$

Then the mean value of the 3D Bohr radius which is the characteristic length of the Coulomb interaction can be written as

$$a_0^* = (\frac{\varepsilon}{\varepsilon_0})(\frac{m_0}{\mu^*})a_H \qquad (7.20)$$

where μ^* is the mean value of the 3D reduced mass of the exciton,which is given by [149]

$$\frac{1}{\mu^*} = \frac{1}{m_e^*} + \gamma_1^* \qquad (7.21)$$

The dimensionless pertinent parameter for the finite quantum well is then given by $\frac{L_z^*}{2a_0^*}$ and the fractional dimension α is

$$\alpha = 3 - \exp\left(-\frac{L_z^*}{a_0^*}\right) = 3 - \exp\left(-\frac{(\frac{2}{k_b} + L_z)}{2a_0^*}\right) \qquad (7.22)$$

By using Eqn.(7.5) together with Eqn.(7.22), the binding energy of the confined exciton in a finite quantum well can be written, without any adjustable parameter, as

$$E_b = \frac{E_0^*}{[1 - \frac{1}{2}\exp(-\frac{2/k_b + L_z}{2a_0^*})]^2} \qquad (7.23)$$

where E_0^* is the mean value of the effective Rydberg energy for the 3D exciton.

In a two dimensional system the anisotropy is stronger. In the present analytical model, however, it seems very difficult to include more accurate subband dispersions. However, an alternative method can be used considering an α dimensional system an interpolation in between the two limiting cases [150]. Then in order to take into account both the spreading of the wave functions into the barriers and the α dependent in-plane effective-masses, E_0^* in Eqn. (7.23) is calculated by using the following expressions for the reduced masses [150] of

$$\frac{1}{\mu_{hh}^*} = \frac{1}{m_e^*} + \gamma_1^* + (3-\alpha)\gamma_2^* \tag{7.24}$$

$$\frac{1}{\mu_{lh}^*} = \frac{1}{m_e^*} + \gamma_1^* - (3-\alpha)\gamma_2^* \tag{7.25}$$

where m_e^*, γ_1^*, γ_2^* are given by Eqns. (7.17), (7.18), (7.19). Equation (7.23) permits us to calculate the exciton binding energy for different pairs of confined states $e_p - h_p$ after the calculation of the energies of the corresponding electron and hole states given by Eqn. (7.8). Moreover, with α given by Eqn. (7.22), it is possible to calculate the excited-state energies of the exciton $(n\rangle 1)$ by using Eqn. (7.1) [150].

It must be noted that the light-and heavy-hole exciton binding energies converge to the same value as the well width becomes very large. This results from the α-dependent in-plane reduced masses given by Eqs. (7.24), (7.25). As an application, let us consider the electron heavy hole e1-hh1 and e1-lh1 ground state transitions. The spatial extension k_b^{-1} is a crucial ingredient of the calculation. The value k_b can be extracted from the resolution of Eqn. (7.8), which provides the values of the confinement energies of the e1 electron and hh1 (lh1) hole. This method allows us to obtain a fully analytical method for computing the binding energies of the ground state excitons, by direct application of Eqn. (7.16) [150].

7.3   Binding energy calculations and discussions

We have reviewed the simple method of Mathiue et al [150] for calculating exciton binding energies in quantum-confined semiconductor structures. The aim of the model calculation, which is developed in the framework of the fractional-dimensional space, is not to compete with the very advanced ones already proposed, but, on the contrary, to avoid tedious and expensive calculations, to obtain, with good accuracy, the exciton binding energy in most of the confined structures where the exciton can be associated with a specific pair of electron and hole subbands. The main result is an analytical expression for the exciton binding energy, free of any adjustable parameter.
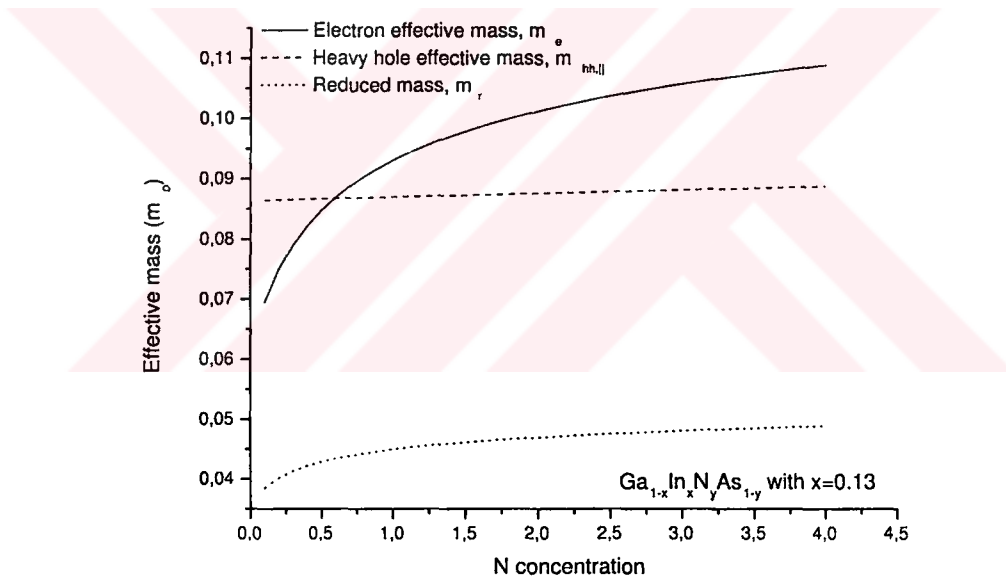

Figure 7.1: The plot of in-plane reduced mass versus nitrogen concentration in $Ga_{0.87}In_{0.13}N_yAs_{1-y}$

(In/N)	Q_c	ΔE_c(eV)	ΔE_v(eV)
(0.46/0)	0.527	0.299	0.268
(0.50/0.011)	.519	0.303	0.281
(0.40/0.017)	0.620	0.355	0.218
(0.33/0.021)	0.696	0.397	0.173
(0.30/0.022)	0.725	0.408	0.155
(0.20/0.026)	0.833	0.460	0.093

Table 7.1: The calculated band offset ratio and the valence- and conduction-band offsets for different In/N ratios in 1.3 μm $Ga_{1-x}In_xN_yAs_{1-y}$ /GaAs quantum well laser structures.

7.3.1 Nitrogen concentration dependence of binding energy

This subsection provides an understanding of variation of exciton binding energy in $Ga_{1-x}In_xN_yAs_{1-y}$ laser material system with N concentration. It has been stated by Ryczko et al [146] that the binding energy of the ground state heavy-hole exciton in $Ga_{1-x}In_xN_yAs_{1-y}$ / GaAs increases both with increasing indium and nitrogen concentrations. They have calculated the exciton binding energy by variational envelope function procedure using simple two-band model, including strains and difference in dielectric constants between well and barrier materials. They have taken a constant conduction band offset of 80 % of the total discontinuity between the bandgap of GaAs and $Ga_{1-x}In_xN_yAs_{1-y}$ grown on GaAs for all concentrations. In this chapter, we calculate the corresponding band offset of $Ga_{1-x}In_xN_yAs_{1-y}$ / GaAs layer for the chosen x/y ratios and therefore include the effect of band offsets into exciton binding energy. We calculate the binding energy of ground state heavy hole exciton according to Eqn. (7.23). The variation of binding energy E_b depends on the variations of E_0^*, L_z, k_b, and a_0^* with nitrogen alloy concentration. E_0^* is the mean value of the effective Rydberg energy for the three dimensional exciton and it is related to the in-plane effective mass of holes of which increases with increasing N alloy concentration in $Ga_{0.87}In_{0.13}N_yAs_{1-y}$ as illustrated in Fig. 7.1. Therefore, the effective Rydberg energy E_0^* increases with increasing nitrogen concentration. An increase in the

mean value of the three dimensional reduced exciton mass is also calculated with an increase in nitrogen alloy concentration, as also illustrated in Fig. 7.1. It can be noted from this figure that alloying with nitrogen provides a closer match between the valence- and conduction-band effective masses in III-N-V systems. On the other hand, the mean value of the effective Bohr radius a_0^* which is given by Eqn. (7.20) decreases with increasing nitrogen alloy concentration.
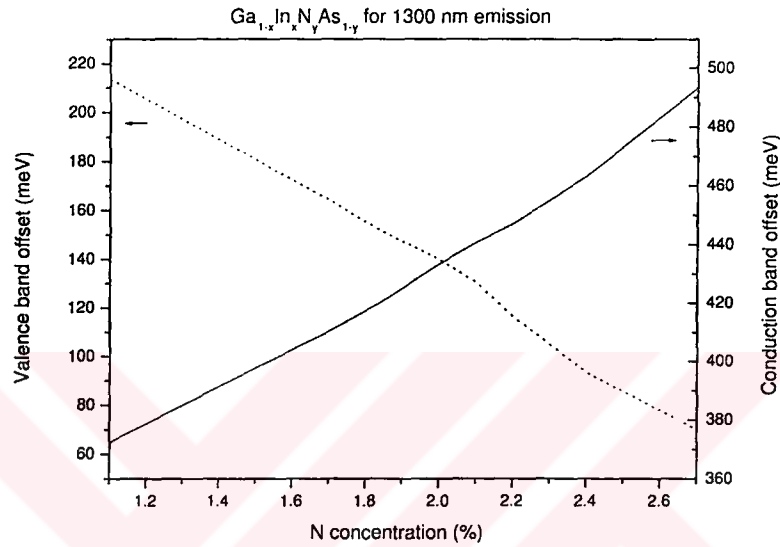
Figure 7.2: The calculated conduction- and valence-band offsets.

The band-offsets in III-N-V alloys greatly depends on the nitrogen concentration. As shown in Fig. 7.2, conduction band offset increases whereas valence band offset decreases with increasing nitrogen concentration. In addition, the incorporation of several percent of nitrogen in $In_xGa_{1-x}As$ alloy increases both the conduction- and valence-band offsets [3]. Therefore, the band offsets of $Ga_{0.87}In_{0.13}N_{0.05}As_{0.95}$/GaAs quantum well is greater than that of the $In_{0.13}Ga_{0.87}As$/GaAs. This leads to a stronger confinement in $Ga_{1-x}In_xN_yAs_{1-y}$ / GaAs laser system. All these combine and results an enhanced exciton binding energy in $Ga_{0.87}In_{0.13}N_{0.05}As_{0.95}$ / GaAs quantum well compared to that of the $In_{0.13}Ga_{0.87}As$ / GaAs quantum well for the whole range of well width, see Fig. 7.3. These variations of the corresponding heavy-hole exciton binding en-
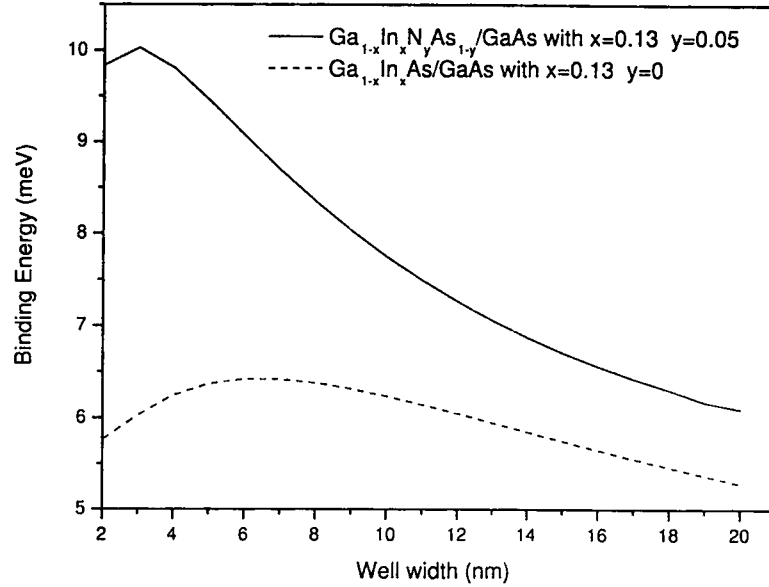
Figure 7.3: Binding energy of ground state heavy hole exciton in quantum wells: $Ga_{0.87}In_{0.13}As$ / GaAs (doted line) and $Ga_{0.87}In_{0.13}N_{0.05}As_{0.95}$ / GaAs (solid line).

ergy with and without nitrogen alloy concentration clearly determines the effect of the nitrogen alloy concentration on heavy-hole exciton binding energy. The curves represent the results obtained by using only one conduction and one valence subband (two band approximation). These results include the dielectric mismatch. First, the binding energy increases as the well width is reduced until it reaches a maximum value, after since it drops. The reason for this behaviour has been explained by Green et al. [129]. As the well width is reduced, the exciton wave function is compressed in the quantum well. However, beyond a certain value of the well width, the part of the wave function in well layer becomes more important and this makes the binding energy approaches to the bulk value.

7.3.2 In/N ratio dependence of binding energy

$Ga_{1-x}In_xN_yAs_{1-y}$/GaAs layer system can be effectively used as a 1.3 μm emitter varying In/N ratio as stated in Chapter 5. We have also concluded that the route of the high In and low N must be followed due to the favorable band
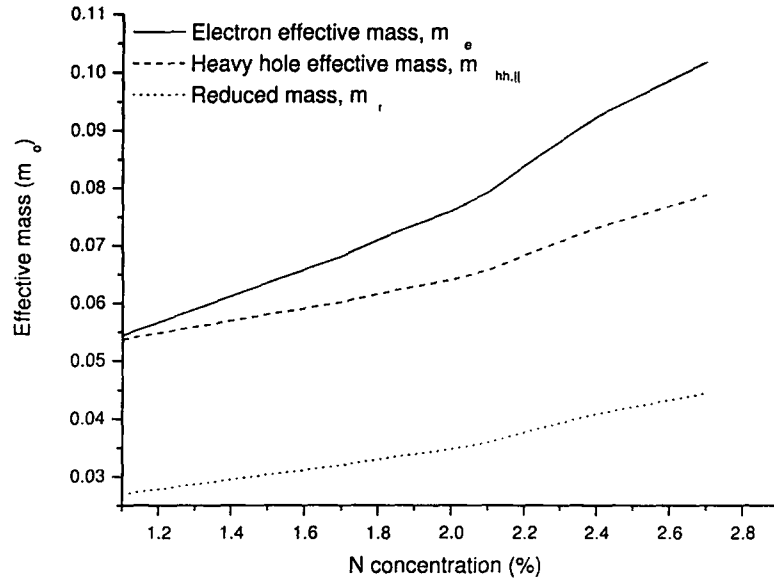
Figure 7.4: The variation of the effective mass of the electron and in-plane heavy-hole mass with In/N ratio.

alignment, better matching of the effective masses, smaller transparency carrier density, higher peak and differential gain and lower spontaneous emission factor. Now, in order to predict the optimal In/N ratio of 1.3 μm $Ga_{1-x}In_xN_yAs_{1-y}$ laser system from the exciton binding energy point of view, we calculate the binding energies for the five model $Ga_{1-x}In_xN_yAs_{1-y}$ /GaAs quantum well laser structures for different x/y (In/N) ratios. Table 7.1 tabulates the band offset ratio and the corresponding valence- and conduction-band offsets of different In/N ratios in 1.3 μm $Ga_{1-x}In_xN_yAs_{1-y}$ /GaAs quantum well laser structures. As can be seen from Table 7.1 that the optimal route is to follow high In and low N in order to effectively confine the carriers into the conduction and valence bands. We also investigate the variation of the effective mass of the electron and in-plane heavy-hole mass with In/N ratio. This is illustrated in Fig. 7.4 in which their corresponding values increases with increasing nitrogen concentration. Finally, the comparison of the ground state heavy-hole exciton binding energy for the five model 1.3 μm $Ga_{1-x}In_xN_yAs_{1-y}$ /GaAs quantum well laser structures is shown in Fig. 7.5. This variation indicates that the route of the low In/high N route is

favourable from the exciton binding energy point of view since the binding energy increases with increasing N and decreasing indium in 1.3 μm $Ga_{1-x}In_xN_yAs_{1-y}$ /GaAs quantum well laser structures.
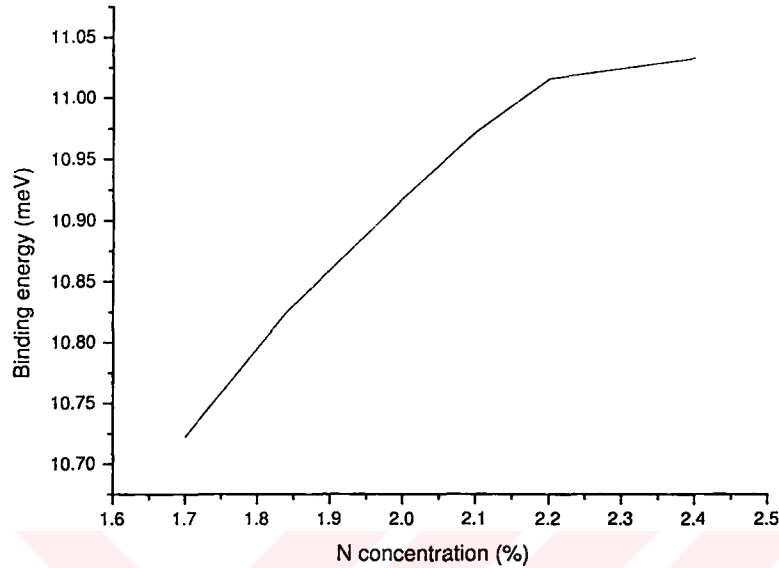
Figure 7.5: The comparison of the ground state heavy-hole exciton binding energy for the five model 1.3 μm $Ga_{1-x}In_xN_yAs_{1-y}$ /GaAs quantum well laser structures.

7.3.3 Comparison of the binding energy of N-based lasers with that of the P- and Al-based lasers

We now want to compare the exciton binding energies of conventional P-based and Al-based lasers with that of the novel laser material system of N-based lasers. We consider three different laser structures operating around 1.3 μm wavelength for comparison. The first type of device studied is P-based lasers which consists of unstrained $Ga_{0.33}In_{0.67}P_{0.28}As_{0.72}/Ga_{0.1}In_{0.9}P_{0.78}As_{0.22}$/InP quantum wells. The second type of device is Al-based structures with $Al_{0.175}Ga_{0.095}In_{0.73}As$ / $Al_{0.27}Ga_{0.21}In_{0.57}As$ / InP lasers structure parameters and the well is 1.4 % compressively strained. The third type of device is N-based lasers with 1.7 % compressively strained $Ga_{0.7}In_{0.3}N_{0.022}As_{0.098}$ QWs between GaAs barriers and

$Al_{0.1}Ga_{0.9}As$ cladding layers. The quantum well thickness and cavity length in all structures is taken as 6 nm and 610 μm, respectively.

Figure 7.6: The calculated values of the ground state heavy-hole exciton binding energies as a function of well width is shown in for the three different laser structures.

Table 7.2 illustrates the calculated values of effective masses and the valence and conduction band offsets for the three laser structures operating around 1.3 μm wavelength. As can be seen from this table N-based lasers exhibits ideal band offset values and better matching of the effective masses than those of the Al-based and P-based lasers. P-based laser parameters seem the worst one.

	P-Based	Al- Based	N-Based
Well	$In_{0.33}Ga_{0.67}As_{0.72}P_{0.28}$	$In_{073}Ga_{0.095}Al_{0.175}As$	$Ga_{0.7}In_{0.3}N_{0.022}As_{0.978}$
Barrier	$In_{0.1}Ga_{0.9}As_{0.27}P_{0.73}$	$In_{0.52}Ga_{0.21}Al_{0.27}As$	GaAs
$m_c(m_o)$	0.0852	0.0516	0.0792
$m_{hh,\parallel}(m_o)$	0.0569	0.0445	0.0683
ΔE_c	0.149	0.225	0.447
ΔE_v	0.169	0.091	0.116

Table 7.2: The tabulated values of the effective masses and the valence and conduction band offsets for the P-based, Al-based and N-based laser structures.
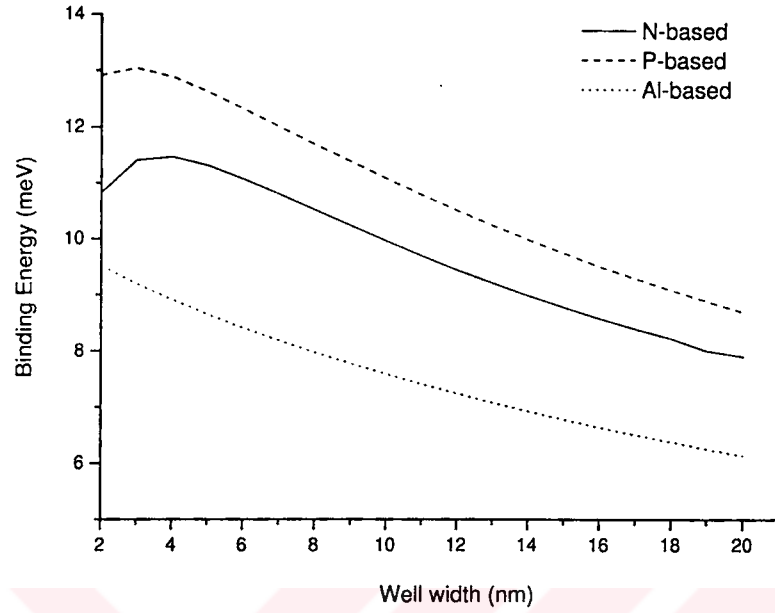
The calculated values of the ground state heavy-hole exciton binding energies as a function of well width is shown in Fig. 7.6 for the three different laser structures. As can be seen from Fig. 7.6 P-based lasers has the highest binding energies which is followed by N-based lasers. On the other hand, Al-based lasers have the smallest binding energies for the whole range of well widths.

7.4   Conclusions

Although the use of the variational technique to obtain the binding energies enables more accurate results, it is tedious. We use the simple method of Mathieu et al [150] in order to avoid these tedious calculations, but, on the contrary to obtain the binding energies with good accuracy. It is not our intention in this study to draw any quantitative conclusions relative to the experiment. Therefore, the use of this analytical method proposed by Mathieu et al [150] is adequate to investigate the excitonic properties in III-V and III-N-V quantum wells. The binding energy of the ground state heavy hole exciton in $Ga_{1-x}In_xN_yAs_{1-y}$ / GaAs was seen to be greater than that of the $In_xGa_{1-x}As$ / GaAs quantum wells. In addition, an enhancement of the exciton binding energy of the ground state heavy hole exciton was also calculated with increasing nitrogen alloy concentration in $Ga_{1-x}In_xN_yAs_{1-y}$/GaAs quantum wells. The close examination of the band-offsets and the corresponding exciton binding energies for 1.3 μm $Ga_{1-x}In_xN_yAs_{1-y}$ / GaAs lasers with different In/N ratios reveals the fact that the route of low In/high N must be followed to get higher binding energies. Finally, we conclude that P-based laser is the ideal laser system from exciton binding energy point of view. N-based lasers have intermediate exciton binding energy values.

Chapter 8

Conclusions and Future work

The work carried out in this thesis considered the effects of alloying, pressure and doping on the properties of III-V and III-N-V quantum well lasers for long wavelength emission. In the result part of related chapters appropriate conclusions have already been presented. However, it is useful in this chapter to briefly summarize and gather together the major conclusions from the work described in this thesis.

GaInNAs/GaAs lasers has the following several unique features. A better high temperature performance of the laser structures is achieved due to a larger conduction band offset and, thus, improved electron confinement and decreased electron spill out at room temperature and above. The increase of the electron effective mass with the addition of nitrogen provides a close match between the effective mass values for electrons and holes, beneficial for laser applications. Moreover, GaInNAs gives the flexibility of tailoring in the bandgap and an increase in the lattice parameter. Hence GaInNAs gives the potential to produce material lattice matched or mismatched to GaAs with a wide range of bandgap energies (from 1.5 eV to less than 0.8 eV). Therefore, nitrogen containing III-V ternary and quaternary alloys represent a novel material system which has the mentioned exciting physical properties and a great potential for many applications in optoelectronic and photonics. By far the most studied and the best understood are the GaInNAs alloys with low nitrogen composition, where im-

pressive progress in the material growth and device fabrication has been achieved within a very short period of time. To secure the full exploration of the alloy potential for device applications, comprehensive studies of the basic band structure and the recombination processes in the materials have been undertaken. The majority of the discovered fundamental physical properties can be refereed to as unusual and fascinating. These include the giant bowing in the bandgap energy, the appearance of the E_- and E_+ subbands in the conduction band, a sublinear pressure dependence of the bandgap energy, a strong increase of the electron effective mass with decreasing bandgap energy (increasing nitrogen composition), etc.

Theoretical calculations have been presented to compare the band alignments of InGaAs/GaAs and GaInNAs/GaAs laser devices. It has been shown that model solid theory can be used to calculate the band alignment of GaInNAs/GaAs laser device where only experimental data available to date. The investigation of the band alignments with and without nitrogen confirms that the ideal band alignment of GaInNAs offer the N-based laser system as an ideal candidate for high temperature operation.

A comparative study of the three competing laser materials, namely InGaAsP/InP, AlGaInAs/InP, and InGaNAs/GaAs has been undertaken, for the first time, involving threshold characteristics with pressure. Our theoretical study investigates the factors that influence the material gain performance, the threshold characteristics and the pressure dependencies of each of the laser systems. We find that AlGaInAs and InGaNAs active layer materials have substantially better material gain performance than the commonly used InGaAsP at room temperature. Both radiative and non-radiative current contributions for laser systems are compared using basic equations which makes our analysis particularly attractive owing to its simplicity and ability to predict the main effects involved. We have found that the estimated variation of phonon-assisted Auger rates with pressure in N-based system has a slower decrease than that of

the other two laser systems. The threshold carrier density n_{th} in N-based system increases with pressure whereas it decreases in Al- and P-based laser systems. This opposite variation changes the overall behavior of the threshold current in these three competing laser systems. Our theoretical calculations indicate a significant increase of the radiative to non-radiative recombination current in N-based laser system. This result highlights the intrinsic superiority of the N-based laser system.

In this thesis we have also presented that the type of the doping has an opposite effect on nitride systems compared to an equivalent nitride-free system. This is another unusual physical property of nitrogen containing alloys due to the nitrogen-induced modifications of the conduction band structure. In conclusion, although the addition of nitrogen into III-V systems increases the transparency carrier density n_{tr}, this disadvantage can be eliminated by means of n- and p-type doping. Especially, p-type doping is more effective to lower transparency carrier density n_{tr} than that of the n-type doping in a nitride system. On the other hand, n-type doping is more effective in increasing gain in nitride system. Our calculations confirm that n-type doping is effective to reduce transparency carrier density n_{tr} whereas p-type doping is effective to increase peak gain in a nitride free system. As an overall, our theoretical investigation reveals the fact that n-and p-type doping have also an unusual, i.e. reverse effect on the band parameters of nitride systems compared to that of the III-V systems. p-type modulation doping of III-N-V quantum well active layers may have certain benefits to lasers in nitride systems.

The theoretical potential advantage of doped $Ga_{1-x}In_xN_yAs_{1-y}$ / GaAs quantum wells for 1.3 μm laser emission is studied. By means of considering different x/y concentrations, we present the influence of doping on transparency carrier density, gain properties and spontaneous emission factor of 1.3 μm emission $Ga_{1-x}In_xN_yAs_{1-y}$ strained quantum wells and compare with an equivalent N-free 1.3 μm $In_xGa_{1-x}As$ / GaAs laser structure. This study provides useful

information for the optimazition of doped $Ga_{1-x}In_xN_yAs_{1-y}$ / GaAs on the basis of 1.3 μm emission wavelength.

We have shown that the Coulomb interaction between injected electrons and holes must be taken into account to have a comprehensive gain model. It has been calculated that the consideration of this Coulombic interaction enhances the linear gain greatly. We have also seen that the magnitude of the enhancement depends on the carrier density.

Finally, a detailed analysis of exciton binding energy in III-V and III-N-V alloys revealed the following facts. The ground state exciton binding energy of III-N-V laser system is greater than III-V laser system and binding energy increases with increasing N concentration. The higher binding energies are obtained by means of keeping the In concentration as low as possible and N concentration as high as possible to get 1.3 μm emission wavelengths using $Ga_{1-x}In_xN_yAs_{1-y}$ / GaAs laser system. From the exciton binding energy of view, P-based lasers display highest binding energies. N-based lasers follows P-based lasers. In addition, Al-based lasers have the smallest binding energies.

It is known that strained heterostructures made from III-V zinc blende type semiconductors grown along (111) orientation can exhibit novel characteristics due to the piezoelectric effect. This effect, vanishes for (001) orientation, can generate built-in internal fields, and thus modify the electronic structure and optical properties of (111) strained heterostructures. The effects of the growth orientation on gain, critical thickness and threshold current is investigated for III-V semiconductors,but it is still unknown for III-N-V semiconductors up to our knowledge. Therefore, we want to examine these growth orientation dependent parameters in III-N-V semiconductors and obtain the variations as a function of nitrogen concentration, as a future work.

List of References

[1] M. Kondow, K. Uomi, A. Niwa, T. Kitantai, S. Watahiki, and Y. Yazawa *Jpn. J. Appl. Phys.* **35**, 1273-1275 (1996).

[2] Li W, Turpeinen J, Melanen P, Savolainen P, Usimaa P and Pessa M *J. Cry. Growth* **230**, 533 (2001).

[3] B Gonul, F Kocak, H Toktamis and M Oduncuoglu, submitted to *Physica E*.

[4] Neugebauer and C. G. Van de Walle, *Phys. Rev. B* **51**, 10568 (1995).

[5] J. Hader, S. W. Koch, J. V. Moleney, E. P. O'Reilly, *Appl. Phys. Lett.* **77**, 630 (2000).

[6] C. Skierbiszewski, P. Perlin, P. Wisniewski, W. Knap, T. Suski, W. Walukiewicz, W. Shan, K.M. Yu, J.W. Ager, E.E. Haller, J.F. Geisz, J.M. Olson, *Appl. Phys. Lett.* **76**, 2409 (2000).

[7] M. Weyers, M. Sato and H. Ando, Japan. *J. Appl. Phys.* **31**, L853 (1992).

[8] J. D. Perkins, A. Mascarenhas, Y. Zhang, J. F. Geisz, D. J. Friedman, J. M. Olson, and S. R. Kurtz, *Phys. Rev. Lett.* **82**, 3312 (1999).

[9] P. N. Hai, W. M. Chen, I. A. Buyanova, H. P. Xin, and C. W. Tu, *Appl. Phys. Lett.* **77**, 1843 (2000).

[10] Z. Pan, L. H. Li, Y. W. Lin, B.Q. Sun, D. S. Jiang, and W. K. Ge, *Appl. Phys. Lett.* **78**, 2217 (2001).

[11] P. Perlin, S. G. Subramanya, D. E. Mars, J. Kruger, N. A. Shapiro, H. Siegle, and E. R. Weber, *Appl. Phys. Lett.* **73**, 3703 (1998).

[12] W. Shan, W. Walukiewicz, J. W. Ager, E. E. Haller, J. F. Geisz, D. J. Friedman, J. M. Olson, S. R. Kurtz, *Phys. Rev. Lett.* **82**, 1221 (1999).

[13] P. J. Klar, H. Grning, W. Heimbrodt, J. Koch, F. Hhnsdorf, W. Stolz, P. M. A. Vicente, and J. Camassel, *Appl. Phys. Lett.* **76**, 3439 (2000).

[14] J. D. Perkins, A. Mascarenhas, J. F. Geisz, and D. J. Friedman, *Phys. Rev. B* **64**, 121301(R) (2001).

[15] G. Leibiger, V. Gottschalch, B. Rheinländer, J. Sik and M. Schubert, *Appl. Phys. Lett.* **77**, 1650 (2000).

[16] D. J. Wolford, J. A. Bradley, K. Fry, and J. Thompson, Proc. 17th Conf. of the Physics of Semiconductors (New York: Springer), p. 627 (1984).

[17] X. Liu, M. E. Pistol, L. Samuelson, S. Schwetlick, and W. Seifert, *Appl. Phys. Lett.* **56**, 1451 (1990).

[18] T. Makimoto, H. Saito, T. Nishida, and N. Kobayashi, *Appl. Phys. Lett.* **70**, 2984 (1997).

[19] M. Kondow, K. Uomi, K. Hosomi, and T. Mozume, Japan. J. Appl. Phys. **33**, L1056 (1994).

[20] T. Yang, S. Nakajima and S. Sakai, *Japan. J. Appl. Phys.* **36**, L320 (1997).

[21] N. Baillargeon, K. Y. Cheng, G. F. Hofler, P. J. Pearah, and K. C. Hsieh, *Appl. Phys. Lett.* **60**, 2540 (1992).

[22] W. G. Bi and C. W. Tu, *Appl. Phys. Lett.* **69**, 3710 (1996).

[23] K. M. Yu, W. Walukiewicz, J. Wu, J. W. Beeman, J. W. Ager III, E. E. Haller, W. Shan, H. P. Xin, and C. W. Tu, *Appl. Phys. Lett.* **78**, 1077 (2001).

[24] J. C. Harmand, G. Ungaro, J. Ramos, E. V. K. Rao, G. Saint-Girons, R. Tessier, G. Le Roux, L. Largeau, and G. Patriarche, *J. Cryst. Growth* **553**, 227-228 (2001).

[25] B. N. Murdin, N. Kamal-Saadi, A. Lindsay, E. P. OReilly, A. R. Adams, G. J. Nott, J. G. Crowder, C. R. Pidgeon, I. V. Bradley, J.-P. R. Wells, T. Burke, A.D. Johnson, and T. Ashley, *Appl. Phys. Lett.* **78**, 1568 (2001).

[26] Shan W, Walukiewicz W and Ager J W III, Haller E E, Geisz J F, Friedman D J, Olson J M and Kurtz S R *J. Appl. Phys.* **86**, 2349 (1999).

[27] W. Walukiewicz, W. Shan, Y. M. Yu, J. W. Ager III, E. E. Haller, I. Miotkowski, M. J. Seong, H. Alawadiii, and A. K Ramdes, *Phys. Rev. Lett.* **85**, 1552 (2000).

[28] A. Rubio and M. L. Cohen, Phys. Rev. B **51**, 4343 (1995).

[29] C. Ellmers, M. Hofmann, W. W Rühle, A. Girndt, F. Jahnke, W. W. Chow, A. Knorr, S. W. Koch, C. Hanke, L. Korte, and C. Hoyler, *Phys. Status Solidi B* **206**, 407 (1998).

[30] I. V. Vurgaftman, J. R. Meyer, L. R. Ram-Mohan, *J. Appl. Phys.* **89**, 5815, (2001).

[31] M. Silver and E. P. O'Reilly, *IEEE J. Quantum Electron.* **31**, 1193 (1995).

[32] I. Suemune, K. Uesugi and W. Walukiewicz, *Appl. Phys. Lett.* **77**, 3021 (2000).

[33] P. Perlin, P. Wisniewski, C. Skierbiszewski, T. Suski, E. Kaminska, S. G. Subramanya, E. R. Weber, D. E. Mars, and W. Walukiewicz, *Appl. Phys. Lett.* **76**, 1279 (2000).

[34] J. Hader, S. W. Koch, J. V. Moloney, and E. P. OReilly, *Appl. Phys. Lett.* **76**, 3685 (2000).

[35] C. Skierbiszewski et al, *Physica Status Solidi B* **216**, 135 (1999).

[36] K. Uesugi, I. Suemune, T. Hasegawa and T. Akutagawa, *Appl. Phys. Lett.* **76**, 1285 (2000).

[37] A. Lindsay and E.P. OReilly, *Solid State Commun.* **112**, 443 (1999).

[38] U. Bandelov, H J Wunsche, B Sartorius, M. Mohrle, IEEE J. Select. *Topics Quantum Electron.* vol. **3**, 270 (1997).

[39] P. Phelan, D. McDonald, A Egan, J. Hegarty, R. O'Dowd, G. Farell, S. Lindgren, *Proc. Ins. Elect. Eng. J.* vol. **141**, 114 (1984).

[40] M. Hetterich and M. D. Dawson, *Appl. Phys. Lett.* **76**, 1030 (2000).

[41] G. Lin and C.P. Lee *Optical and Quantum Electronics* **34**, 1191 (2002).

[42] A.R. Adams, K.C. Heasman and J. Hilton, *Semicond. Sci. Technol.* **2**, 761 (1987).

[43] E. D. Jones, A. A. Allerman, S. R. Kurtz, N. A. Modine, K. K. Bajaj, S. W. Tozer and X. Wei, *Phys. Rev. B* **62**, 71447149 (2000).

[44] M. Hawley, PhD Thesis, University of Surrey (1994).

[45] B. Gönül, PhD Thesis, University of Surrey (1995).

[46] K.J. Vahala and C.E. Zah, *Appl. Phys. Lett.* **52**, 1945 (1988).

[47] T. Higashi, S. J. Sweeney, A. F. Phillips, A. R. Adams , E. P. O'Reilly, T. Uchida and T. Fujii, *IEEE Photon. Technol. Lett.* **11**, 409 (1999).

[48] I. A. Buyanowa, W. M. Chen and B. Monemar, *MRS Internet J. Nitride Semicond. Res.* **6**, 2 (2001).

[49] J. C. L. Yong, Judy M. Rorison, and Ian II. White, *IEEE J. Quantum. Electron.* **38**, 1553 (2002).

[50] C. K. Kim and Y. H. Lee, *Appl. Phys. Lett.* **79**, 3038 (2001).

[51] J. Minch, S. H. Park, T. Keating, and S. L. Chuang, *IEEE J. Quantum. Electron.* **35**, 771 (1999).

[52] L. F. Tiemeijer, P. J. A. Thijs, P. J. de Waard, J. J. M. Binsma, T. Van Dongen, *Appl. Phys. Lett.* **58**, 2738 (1991).

[53] P. J. A. Thijs, J. J. M. Binsma, L. F. Tiemeijer T. Van Dongen, *Proceedings ECOC* **31** (1991).

[54] J. P. Loehr, J. Singh, *IEEE J. Quantum. Electron.* **QE-27**, 708 (1991).

[55] A. Ghiti, W. Batty, U. Ekenberg, E.P. O'Reilly, *SPIE 861*, **96** (1987).

[56] B.Gönül, *Semicond. Sci. Technol.* **14**, 648 (1999).

[57] B. Gönül, *Physica E.* **5**, 50 (1999).

[58] A. Haug and B. Photophys, *Laser Chem.* **11** 151-153 (1987).

[59] D. P. Bour, G. A. Evans and D. B. Gilbert, *J. Appl. Phys.* **65**, 3340 (1989).

[60] A. P. Mozer, S. Hausser and M. H. Pilkuhn, *IEEE J. Quantum Electron.* **21**, 719 (1985).

[61] Sugimura1981 A. Sugimura, *IEEE J. of Quantum Electronics.* **QE-17**, 627 (1981).

[62] W. Lochmann, *Phys. Status Solidi A* **40**, 285 (1977).

[63] W. Lochmann, *Phys. Status Solidi A* **42**, 181 (1977).

[64] R.I. Taylor, R.A. Abram, M.G. Burt, and C. Smith, *IEE Proc.*, **132**, 364 (1985).

[65] A. Haug, *J. Phys. C*, **17**, 6191 (1984).

[66] L. Huldth. *Phys. Status Solidi A* **24**, 221 (1974).

[67] A. Sugimura, *IEEE J. of Quantum Electronics*, **QE-19**, 932 (1983).

[68] A. Haug, *Electron. Lett.*, **26**, 1415 (1990).

[69] C. Smith, R.A. Abram, and M.G. Burt, *J. Phys. C*, **16**, L171 (1983).

[70] A. R. Adams, M. Silver, and J. Allam, *Semicond. and Semimet.* **55**, 301 (1998).

[71] A.R. Adams, *Electron. Lett.*, **22**, 249 (1986).

[72] S. Seki, W. W. Lui, and K. Yokoyama, *Appl. Phys. Lett.*, vol. **66**, 30933095 (1995).

[73] S. Mogg and J. Piprek, in Proc. *SPIE Physics and Simulation of Optoelectronic Devices*, vol. **4283**, 29 (2001).

[74] A. Haug, *J. Phys. C: Solid State Phys.* **17**, 6191 (1984).

[75] N. K. Dutta and R. J. Nelson, *J. Appl. Phys.* **53**, 74 (1982).

[76] M. Takeshima, *Phys. Rev. B* **30**, 3302 (1984).

[77] A. Haug, *Semicond. Sci. Technol.*, **7**, 1337 (1992).

[78] A. Haug, *Appl. Phys. Lett.* **42**, 512 (1983).

[79] A. Sugimura, *J. Appl. Phys.*, **51**, 4405 (1980).

[80] P. Lawaetz, *Phys. Rev. B*, 4, 3460 (1971).

[81] M J Adams An Introduction to optical Wavequides (New York: Wiley) (1981).

[82] S. R. Jin et al, *Electron. Lett.* **38**, 93 (2002).

[83] H C Casey and M B Panish, Heterostructure Lasers (Acedemic, New York, 197.

[84] K J Ebeling, Integrated Optoelectronics (Springer-Verlag, Berlin. (1993).

[85] A. Lancefield et al, *J. Phys. Chem. Solids* **56**, 469 (1995).

[86] E. P. O'Reilly and A. R. Adams, *IEEE J. Quantum Electron.* **30**. 366 (1994).

[87] A. R. Adams, K. C. Heasman and E. P. O'Reilly, Band Structure Engineering in Semiconductor Microstructures, ed R. A. Abram and M. Jacos (New York: Plenum) p 279.

[88] S. Seki, H. Oohashi, H. Sugiura, T. Hirono and K Yokoyama, *IEEE J. Quantum. Electron.* **32**, 1478 (1996).

[89] J. W. Pan and J. L. Chyi, *IEEE J. Quantum. Electron.* **32**, 2133 (1996).

[90] R. Fehse, S. J. Sweeney, A. R. Adams, E. P. O'Reilly, A Y Egorov, H. Riechert and S. Illek, *Electron. Lett.* **37**, 325 (2003).

[91] S. J. Sweeney, S. R. Jin, S. Tomic, A. R. Adams, T. Higashi, H. Riechert and P. J. A. Thijs, *Phys. Stat. Sol. B* **235**, 474 (2003).

[92] H.P. Xin, C.W. Tu, *Appl. Phys. Lett.* **72**, 2442 (1998).

[93] M. Kondow, T. Kitatani, K. Nakahara, T. Tanaka, *Jpn. J. Appl. Phys.* L1356 (1999).

[94] M. Kondow, T. Kitatani, S. Nakatsuka, M. Larson, K. Nakahara, Y. Yazawa, M. Okai and K. Uomi, *IEEE J. Quantum Electron.* **3**, 719 (1997).

[95] M. Hofmann, A. Wagner, C. Ellmers, C. Schlichenmeier, S. Schafer, F. Höhnsdorf, J. Koch, W. Stolz, S.W. Koch, W.W. Rühle, J. Hader, J.V. Moloney, E.P. O'Reilly, B. Borchert, A. Egorov Yu and H. Riechert, *Appl. Phys. Lett.* **78**, 3009 (2001).

[96] D. Alexandropoulos and M.J. Adams, J. Phys. Conds. Matter. **14**, 3523 (2002).

[97] B. Gonul, M. Oduncuoğlu, S. Dindaroglu and B. Yağdıran, *Semicond. Sci. Technol.* **18**, 163 (2003).

[98] W.W Chow and J.S. Harris, *Appl. Phys. Lett.* **82**, 1673 (2003).

[99] W.A. Harrison, *J Vac. Sci. Technol.* **14**, 1016 (1997).

[100] K.M. Yu, W. Walukiewicz, W. Shan, J.W. Ager III, J. Wu and E.E. Haller, H.P. Xin and C.W. Tu, *Phys. Rev. B* **61**, R13337 (2000), K.M. Yu *Semicond. Sci. Technol.* **17**, 785 (2002).

[101] D. Alexandropoulos and M.J. Adams, *IEE Proc. Optoelectron.* **150**, 105 (2003).

[102] W. Shan, W. Walukiewicz, K.M. Yu, J.W. Ager III, E.E. Haller, H.P. Xin and C.W. Tu, *Appl. Phys.Lett.* **76**, 3251 (2000).

[103] K.M. Yu, W. Walukiewicz, W. Shan, J. Wu, J.W. Beeman, J.W. Ager III. E.E. Haller, H.P. Xin and C.W. Tu, *Appl. Phys Lett.* **78**, 1017 (2001).

[104] E.D. Jones, N.A. Modine, A.A. Allerman, S.R. Kurtz, A.F. Wright, S.T. Torez, X. Wei, *Phys. Rev. B.* **60** 4430 (1999).

[105] E.D. Jones, N.A. Modine, A.A. Allerman, I.J. Fritz, S.R. Kurtz, A.F. Wright, S.T. Torez, X. Wei, *Proc. SPIE* **52**. 3621 (1999).

[106] A. Lindsay, E.P. O'Reilly, *Sol. St. Comm.* **112**, 443 (1999).

[107] T. Mattila, S.H. Wei, A. Zunger, *Phys. Rev. B* **60**, R11245 (1999).

[108] J.P. Loehr, J. Singh, *IEEE J. Quantum. Electron.* **QE-27**, 708 (1991).

[109] A. Ghiti, W. Batty, U. Ekenberg, E.P. O'Reilly, *SPIE* **96**, 861 (1987).

[110] B. Gönül *Physica E.* **5**, 50 (1999).

[111] S.L. Chuang, Physics of Optoelectronic Devices. New York:Wiley ch. 9 1995.

[112] E. Haken and H.Haken, *Z. Phys.*, **176**, 421-428 (1963).

[113] H. Haug and H. Haken, *Z. Phys.*, **204**, 262-275 (1967).

[114] H. Haug, *Phys. Rev.*, **184**, 338 (1969).

[115] P.D. Dapkus, N. Holonyak Jr., J.A. Rosi, F.V. Willianms, and D.A. High, *J. Appl. Phys.*, **40**, 3300 (1969).

[116] M. Lindberg and S.W. Koch, *Phys. Rev. B*, **38**, 3342-3350 (1988).

[117] H. Haug and S.W. Koch, *Phys. Rev. A*, **39**, 1887-1898 (1989).

[118] H.Haug and S.W. Koch, Quantum Theory of the optical and electronic properties of semiconductors, 2nd. (World Scientific, Singapore), (1993).

[119] W. W. Chow, S. W. Koch, and M. Sargent, Semiconductor Laser Physics, Springer, Heidelberg, Berlin, (1994).

[120] S. Tarucha, H. Kobayashi, Y. Horikoshi, H, Okamoto, *Jpn. J. Appl. Phys.*, **23**, 874 (1984).

[121] A. Tomita, A. Suzuki, *IEEE J. Quantum Electron.*, **QE-23**, 1155 (1987).

[122] M.P. Kesler, C. Harder, *IEEE J. Quantum Electron.*, **QE-27**, 1812 (1991).

[123] W. W. Chow, S.W. Koch, Semiconductor-Laser Fundamentals, Physics of the Gain Materials, Springer (1999).

[124] H. Haugh and S Schmitt-Rink, Prog. Quantum Electron, vol **9**, 3-100, (1984).

[125] H. Huag, S. Schmitt-Rink, *J. Opt. Soc. Am* **B2**, 1135 1985; S. Schmitt-Rink, C. Ell, and H. Haug, *Phys. Rev.* **B33**, 1183 (1986).

[126] M. Asada, Y. Yasuyuki and Y. Suematsu, *IEEE J. Quantum Electron.*, **QE-22**, 1915 (1986).

[127] R.C. Miller, D.A. Kleinman, W.T. Tsang, and A.C. Gossard. *Phys. Rev. B*, **24** 1134 (1981).

[128] L.C. Andreani and A. Pasquarello, *Phys. Rev. B*, **42** 8928 (1990).

[129] R. L. Greene, K. K. Bajaj and D. E. Phelps, *Phys. Rev. B*, **29** 1807 (1984).

[130] F. J. Betanuer, I. D. Mikhailov and L. E. Oliveira, *J. Phys. D Appl. Phys.*, **31** 3391 (1998).

[131] P. Lefevre, P. Christol, H. Mathieu and S. Glutsch, *Phys. Rev. B*, **52** 5756 (1995).

[132] E. Reyes-Gomez, A. Matos-Abiague, C. A. Perdomo-Leiva, M. de Dios-Leyva and L. E. Oliveira, *Phys. Rev. B*, **61** 13104 (2000).

[133] F.J.Betanuer. *Phys. Rev. B,* vol **33** 2 (2001).

[134] M.C.Y. Chan, C. Surya and P.K.A. Wai. *J. Appl. Phys.*, **90** 197 (2001).

[135] A. Polimeni, M. Capizzi, M. Geddo, M. Fischer, M. Reinhardt and A. Forchel. *Phys. Rev. B*, **63** 195320 (2001).

[136] W.J. Fan and S.F. Yoon, *J. Appl. Phys.*, **90** 843 (2001).

[137] G. Sek, K. Ryczko, J. Misiewicz, M. Fischer, M. Reinhardt and A. Forchel, *Thin Solid Films*, **380** 240 (2000).

[138] A. Polimeni, M. Capizzi, M. Geddo, M. Fischer, M. Reinhardt and A. Forchel, *Appl. Phys. Lett.*, **77** 2870 (2000).

[139] M.-A. Pinault and E. Tournie, *Appl. Phys. Lett.*, **78** 1562 (2001).

[140] R.A. Mair, J.Y. Lin, H.X. Jiang, E.D. Jones, A.A. Allerman and S.R. Kurtz, *Appl. Phys. Lett.*, **76** 188 (2000).

[141] G. Bastard, E.E. Mendez, L.L. Chang and L. Esaki, *Phys. Rev. B*, **26** 1974 (1982).

[142] E.H. Li. *Physica E*, **5** 215 (2000).

[143] J. Reithmaier, R. Hoger and H. Riechert. *Phys. Rev. B*, **43** 4933 (1991).

[144] R.C. Iotti and L.C. Andreani, *Semicond. Sci. Technol.*, **10** 1561 (1995).

[145] D.A.B. Miller, D.S. Chemla, T.C. Damen, A.C. Gossard, W. Wiegmann, T. Wood, and C.A. Burrus, *Phys. Rev. B*, **32** 1043 (1985).

[146] K. Ryczko, G. Sek, J. Misiewicz, *Solid State Commun.*, **122** 323-327 (2002).

[147] R.P. Leavitt and J.W. Little, *Phys. Rev. B*, **42** 11774 (1990).

[148] X.F. He, *Phys. Rev. B*, **43** 2063 (1991).

[149] A. Baldereschi and N.O. Lipari, *Phys. Rev. B*, **3** 439 (1971).

[150] H. Mathieu, P. Lefevre and P. Christol. *Phys. Rev. B*, **46** 4092 (1992).

Publications

[1] M. Oduncuoğlu and B. Gönül, II. Kızılırmak Uluslararası Fen Bilimleri Kongresi (Fizik), Kırıkkale University, 20-22 May, 136, (1998).

[2] B. Gönül, S. Dindaroğlu and M. Oduncuoğlu, Balkan Physics Letters, **10** 200 (2002).

[3] M. Oduncuoğlu and B. Gönül, Balkan Physics Letter, **10** 208 (2002).

[4] B. Gönül, M. Oduncuoğlu, S. Dindaroğlu and B. Yağdıran, Semiconductor Science and Technology, **18** 163-169 (2003).

[5] B Gönül and M. Oduncuoğlu, Semiconductor Science and Technology, **19** 23-32 (2004).

[6] H. Toktamış, B. Gönül and M. Oduncuoğlu, Physica E, accepted for publication.

[7] B. Gönül, F. Koċak, H. Toktamış and M. Oduncuoğlu, submitted to Physica E.

[8] M. Oduncuoğlu and B. Gönül, submitted to Solid State Commun.

[9] M. Oduncuoğlu, M. Göl and B. Gönül, submitted to European Physical Journal B.

Curriculum Vitae

The author was born in Antalya, in December, 1973. He graduated from Antalya Kocademir Elementary, Hızır Reis Secondary and Çağlayan High Schools in Antalya, in 1985, 1988, and 1991, respectively. He received his B. S. degree in Engineering Physics Department from University of Gaziantep in July 1996. He worked as a teacher in Isparta from 1996 to 1997. Then he has been accepted as a Research Assistant in the Department of Engineering Physics at the University of Gaziantep. He has completed his M. Sc. degree, in 2000, under the topic of "Effects of growth orientation on the properties of semiconductor quantum well lasers". He has started his Ph. D. program in 2000 and his main areas of interest are Semiconductor Laser Structures. He is married and has one child.